UNIVERSIDADE FEDERAL DE PERNAMBUCO
CENTRO DE CIÊNCIAS EXATAS E DA NATUREZA
PROGRAMA DE PÓS-GRADUAÇÃO EM FÍSICA

Daniel Canavello Moura de Araújo

Dynamics of Self-Aligning Polar Active Matter

Recife
2025

Daniel Canavello Moura de Araújo

Dynamics of Self-Aligning Polar Active Matter

Thesis submitted to the Graduate Program in Physics at Universidade Federal de Pernambuco as a partial requirement for obtaining the degree of Doctor of Physics.

Area of Concentration: Theoretical and Computational Physics

Advisor: Prof. Dr. Clécio Clemente de Souza Silva

Recife

2025

.Catalogação de Publicação na Fonte. UFPE - Biblioteca Central

Araújo, Daniel Canavello Moura de.
Dynamics of self-aligning polar active matter / Daniel Canavello Moura de Araújo. - Recife, 2025.
95f.: il.

Tese (Doutorado) - Universidade Federal de Pernambuco, Centro de Ciências Exatas e da Natureza, Programa de Pós-Graduação em Física, 2025.
Orientação: Clécio Clemente de Souza Silva.
Inclui referências e apêndices.

1. Matéria ativa; 2. Auto alinhamento; 3. Sistemas interagentes. I. Silva, Clécio Clemente de Souza. II. Título.

UFPE-Biblioteca Central

DANIEL CANAVELLO MOURA DE ARAÚJO

DYNAMICS OF SELF-ALIGNING POLAR ACTIVE MATTER

Thesis submitted to the Graduate Program in Physics at Universidade Federal de Pernambuco as a partial requirement for obtaining the degree of Doctor of Physics.

Area of Concentration: Theoretical and Computational Physics

Date of Approval: 30/06/2025.

THESIS COMMITTEE

Prof. Dr. Clécio Clemente de Souza Silva
Advisor
Universidade Federal de Pernambuco

Prof. Dr. Paulo Roberto de Araujo Campos
Internal Examiner
Universidade Federal de Pernambuco

Prof. Dr. Raí Maciel de Menezes
Internal Examiner
Universidade Federal de Pernambuco

Prof. Dr. Anderson Luiz da Rocha e Barbosa
External Examiner
Universidade Federal Rural de Pernambuco

Prof. Dr. Carolina Brito Carvalho dos Santos
External Examiner
Universidade Federal do Rio Grande do Sul

ACKNOWLEDGEMENTS

This thesis is the result of a long journey that I could not have completed without the support of many others. While my words are few, the feelings of gratitude I have are anything but. I want to thank my advisor, Prof. Clécio Clemente, for both introducing me to the area of active matter and continuing to help me throughout my work, and Prof. Leonardo Cabral, who also gave invaluable help in making this work a reality. I want to extend a huge thank you to my friends in the lab as well — Matheus, Rubens, Fernando, Lucas Gabriel, and many others, who always helped me out. And to my friends that now live far away, including Gabriel, Lucas, Eduardo and Pedro, let's keep watching detective series together.

I would like to thank especially my brother, Fernando, and my mother Fátima for their support, without which this work would not have been possible. And finally, I would like to thank *you*, the reader, for taking the time to read my work.

"Hofstadter's Law: It always takes longer than you expect, even when you take into account Hofstadter's Law". (HOFSTADTER, 1979)

ABSTRACT

Active matter systems consist of self-propelled particles that continuously convert energy into motion, maintaining a state of constant non-equilibrium. In many cases, the orientation of a particle's propulsion becomes misaligned with its actual velocity, creating an angle between the two vectors. This can happen during interactions with external confining potentials or collisions with other particles. By incorporating self-alignment dynamics, a torque emerges to align the particle's orientation with its velocity. This phenomenon is observed in both biological and synthetic systems, and significantly alters the dynamics both in the individual particle level and in the collective behaviors of the system. For a single particle, it can lead to orbital motion in confining potentials, while at the collective level, it leads to phenomena such as flocking transitions and self-organization, depending on the system's geometry. This work begins with a review of existing results for individual particle systems and progresses to explore the impact of self-alignment torque on collective dynamics. First, flocking behavior is investigated in systems without confinement, identifying a critical torque threshold for the onset of flocking. Introducing obstacles leads to spontaneous lane formation along the symmetry directions of the substrate. By adding a harmonic confinement to the system, several new phases emerge, including: a magnetized state where all particles align in the same direction and orbit the potential center; a compact vortex state where particles share the same angular velocity, resulting in a collective rotation around the potential; a hollow vortex state displaying shear banding between the inner and outer layers; and a state in which the system splits into several small clusters. To support these findings, a rigid-body model was developed to complement numerical results and a phase diagram was constructed to characterize the emergence of these phases.

Keywords: active matter; self alignment; interacting systems.

RESUMO

Sistemas de matéria ativa consistem em partículas auto-propelidas que continuamente convertem energia em movimento, mantendo um estado de constante não-equilíbrio. Em muitos casos, a orientação de propulsão de uma partícula fica desalinhada com a direção de movimento, criando um ângulo entre os dois vetores. Isso pode ocorrer durante a interação com potenciais confinadores externos ou por colisão entre partículas. Ao incorporar dinâmicas de auto-alinhamento entre partículas, um torque surge para alinhar a orientação com a velocidade. Esse fenômeno ocorre tanto em sistemas biológicos quanto sintéticos, e altera de maneira significativa as dinâmicas tanto em nível individual quanto coletivo. Para uma partícula, tal torque pode levar a movimento orbital na presença de um potencial confinador, já para dinâmicas coletivas, isso leva a fenômenos como transições de comportamento coletivo e auto-organização, a depender da geometria do sistema. Esse trabalho começa com uma revisão de resultados existentes para sistemas de uma partícula, e parte para explorar o impacto do torque de auto-alinhamento em dinâmicas coletivas. Para começar, o comportamento de alinhamento é investigado em sistemas sem confinamento, identificando um torque crítico para que haja alinhamento coletivo. Com a introdução de obstáculos, observa-se uma formação espontânea de faixas ao longo das direções de simetria do substrato. Ao incluir um confinamento harmônico ao sistema, várias novas fases aparecem, incluindo: um estado magnetizado onde todas as partículas alinham na mesma direção e orbitam o centro do potencial; um estado de vórtice compacto onde todas as partículas têm a mesma velocidade angular, resultando numa rotação coletiva ao redor do potencial; um estado de vórtice oco, com cisalhamento entre camadas internas e externas; e um estado onde o sistema separa em vários grupos menores. Para apoiar essas descobertas, um modelo de corpo rígido foi desenvolvido para complementar os resultados numéricos e um diagrama de fases foi construído para localizar e caracterizar o aparecimento dessas fases.

Palavras-chaves: matéria ativa; auto alinhamento; sistemas interagentes.

LIST OF FIGURES

LIST OF TABLES

CONTENTS

1 INTRODUCTION

The title of this thesis, “Dynamics of Self-Aligning Polar Active Matter”, can be broken down into parts and examined

- *Dynamics* refers to the study of dynamical phases and time-dependent behavior of the system.
- *Self-aligning* indicates the internal property that particles possess to adjust their own orientation vector.
- *Polar* refers to particles that exhibit a well-defined directionality, characterized by a head-tail distinction, in contrast to nematic systems, which lack this directional asymmetry.
- *Active matter* refers to the rich class of systems that consist of self-propelled agents, constantly converting energy into motion.

Bringing these topics together, this thesis investigates the temporal evolution and emergent collective behavior observed in polar active matter systems, particularly when self-aligning interactions are included. By focusing on how local alignment mechanisms influence large-scale dynamics, this work contributes to a broader understanding of how different phases spontaneously arise in systems with these properties.

This introductory chapter outlines some key features that make active matter systems a rich and compelling area of research. The thesis begins with a brief historical overview and the motivations that led to the development of active matter systems. It then explores the various environments in which these systems can be found and introduces some of the key models used to describe their dynamics.

1.1 ACTIVE MATTER SYSTEMS

Broadly speaking, active matter refers to systems composed of individual units that are able to convert local energy into directed motion. This phenomenon is observed in nature across several length scales, from the collective motion of animal groups to the movement of individual bacteria. In addition to natural systems, artificial active matter has been designed, including microswimmers and robotic swarms, that mimic some of the behaviors of living systems. As energy is supplied at the individual level, the system is kept out of equilibrium, leading to the breakdown of time-reversal symmetry and a departure from common results in equilibrium statistical physics. Due to this, a wide range of non-equilibrium effects can be observed in active matter systems, such as collective motion and cluster formation (RAMASWAMY, 2017; CHATÉ, 2020).

Figure 1 provides a comprehensive overview of various phenomena in the realm of active matter, highlighting the diversity of systems and phenomena associated with this field. Panel (a) presents examples of both natural and artificial systems of varying sizes that can be classified as active, based on their ability to consume energy in order to generate systematic movement. By supplying energy directly at the individual level, active matter differentiates itself from, for example, passive matter with global, external drives. This distinction enables active systems to interact with their environment in complex ways, such as developing foraging strategies and navigating chemical gradients, as shown in panel (b). As collections of active components interact, new and more intricate behaviors can emerge. One example is the formation of swarms, where individual units synchronize their motion, forming cohesive groups that move collectively in response to local interactions. Another notable behavior is the appearance of clusters, in which active components aggregate into localized groups. These, along with some other complex patterns, are illustrated in panel (c), highlighting the rich variety of self-organizing phenomena that active matter systems can exhibit (CICHOS et al., 2020).

Figure 1 – (a) Examples of systems that can be considered active across several length scales. (b) Different ways in which active particles can interact with the environment. (c) Some types of collective behavior that can emerge due to interactions between active particles.

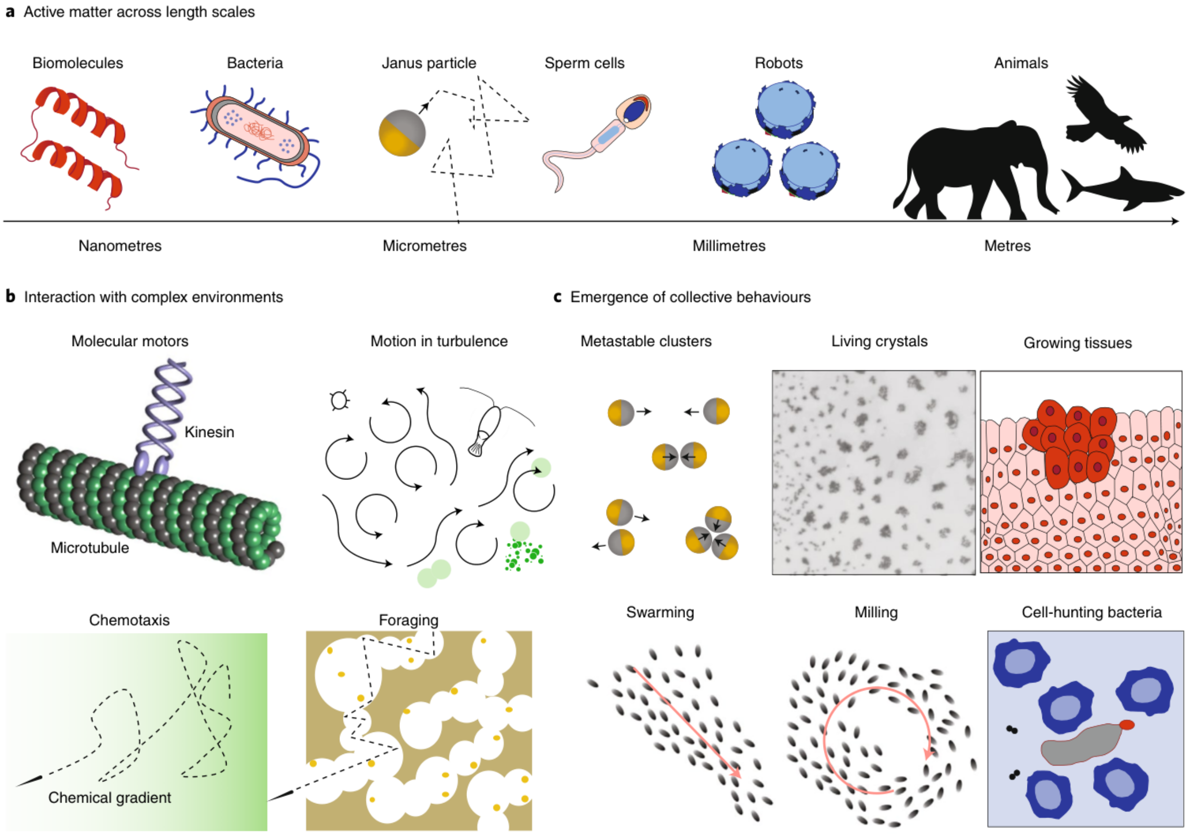

Source: (CICHOS et al., 2020)

1.2 PHYSICAL MODELS OF ACTIVE MATTER

The systematic study of active matter systems in physics, as a subfield of soft matter, is relatively recent. The model that popularized this area of research originated from the seminal work by Vicsek et al. (1995), which was published only 30 years prior to the writing of this thesis. Aiming to reproduce biological swarming phenomena, such as bird flocks and school fish, the well known and widely studied Vicsek model relies on few, simple rules and exhibits a rich phenomenology associated with it. Notably, the model consists on point-like particles propelling themselves along a given direction and at each timestep the orientation takes the value of the average orientation of its neighbors, along with a random noise. By doing this, a first order transition from disordered, gas-like behavior to ordered motion was found for critical values of noise[1]. A continuum model associated with the Vicsek model was developed shortly after

---

[1] Interestingly, a model with similar rules had already been introduced about a decade before Vicsek's work was published by Reynolds (1987), who introduced boids (bird-oids) particles that possess similar alignment rules to Vicsek's model. However this was done in the context of generating computer animations of flocks,

and various critical exponents associated with the flocking transition were calculated (TONER; TU, 1995; TONER; TU, 1998). The emergence of collective motion remains a topic of research in active matter systems, as it displays a deep insight into the mechanisms of active systems, which include both living beings and synthetic materials, and the presence of universal behaviors found in non-equilibrium systems (LAM; SCHINDLER; DAUCHOT, 2015; MARTÍN-GÓMEZ et al., 2018; FEHLINGER; LIEBCHEN, 2023; VICSEK; ZAFEIRIS, 2012). Although governed by relatively simple rules, the system exhibits surprisingly complex dynamics, including the presence of chaos, as seen in recent studies (MIRANDA-FILHO et al., 2022; GONZÁLEZ-ALBALADEJO; CARPIO; BONILLA, 2023).

As the field evolved, more sophisticated models were developed to explore different types of active systems. Some of the main classifications seen in active matter models are: dry vs. wet systems, regarding whether hydrodynamics play an important role or not (MARCHETTI et al., 2013), and polar vs. nematic, which differentiates according to the presence of head-tail symmetry (DOOSTMOHAMMADI et al., 2018; VENKATESH; SOUSA; DOOSTMOHAMMADI, 2025). The shape of the particle also plays an important role in the system dynamics (WENSINK et al., 2014), as symmetry, which can be for example spherical or rod-like (SAINTILLAN; SHELLEY, 2013; SPELLINGS et al., 2015), susceptibility to deformations (ARROYO et al., 2012) and the presence of appendages such as flagella or cillia (GILPIN; BULL; PRAKASH, 2020) can modify the behavior of the system in a nontrivial manner. Some complex models might even feature many-body interactions to optimize certain local conditions (ZAMPETAKI et al., 2021). While this vast range of different properties might make active systems appear to be intractable, they share several properties among them, such as (but not limited to): broken time-reversal symmetry[2], lack of equation of state and being far from equilibrium (ELGETI; WINKLER; GOMPPER, 2015). This makes even minimal models exhibit a wealth of unique behaviors, such as the formation of bands and clusters even in the absence of attractive interactions (ROMANCZUK et al., 2012; BOWICK et al., 2022; RAMASWAMY, 2010).

In Figure 2, a range of both biological and artificial swimmers are exhibited, highlighting the scales at which these systems can be built and operate in. Of course, the principles of active matter extend beyond the micro-scale and can also be applied to macroscopic systems, such as birds (BALLERINI et al., 2008; CAVAGNA et al., 2010), fish (WARD et al., 2008; MAKRIS et al.,

---

and not phase transitions.

[2] Which is a necessary condition for directed motion in viscous fluids, as a consequence of Purcell's famous scallop theorem (PURCELL, 1977)

Figure 2 – Order of magnitude for the size and speed for several classes of biological and synthetic swimmers, demonstrating the vast range of sizes in which self-propelled particles can exist, from nano to micro scales. The insets show examples of the most popular biological and artificial systems. The letters represent different types of artificial swimmers that have been created and a detailed table of those can be found on (BECHINGER et al., 2016).

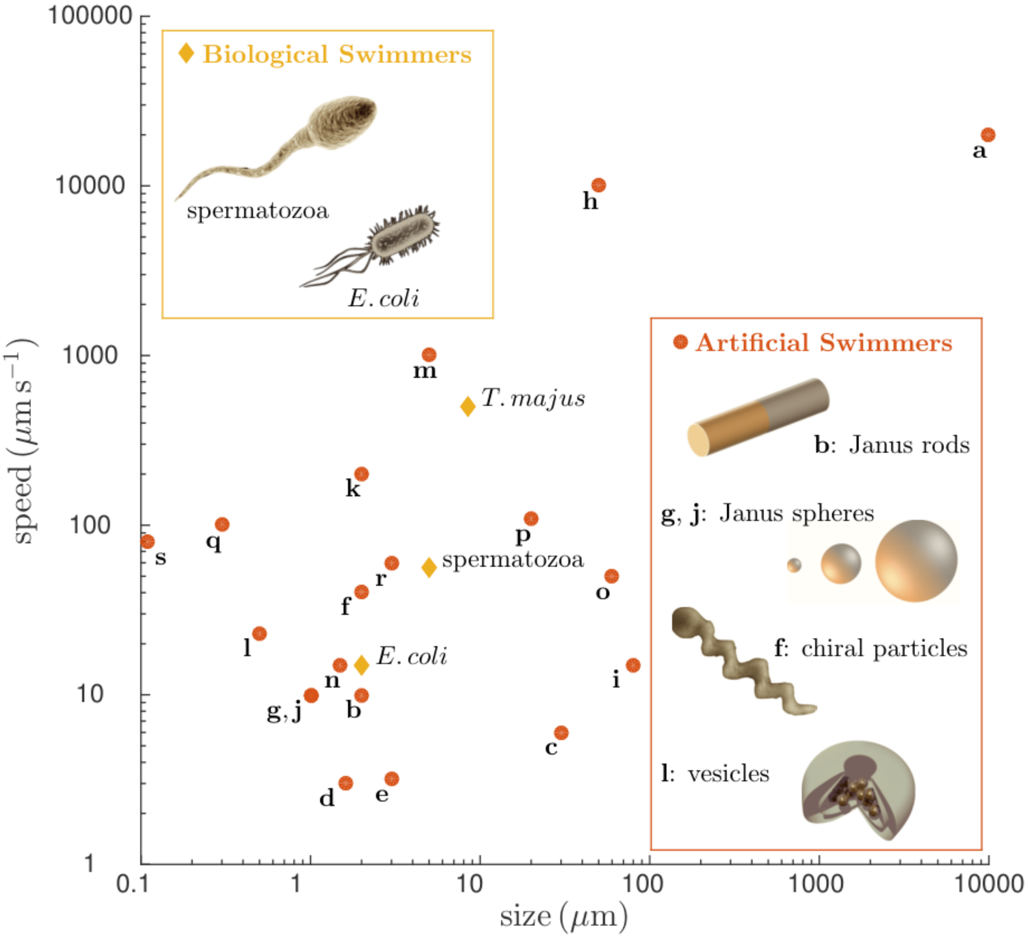

Source: (BECHINGER et al., 2016)

2009) and mammals (SUMPTER, 2006), including humans (MOUSSAÏD; HELBING; THERAULAZ, 2011).

Given that active matter spans a wide range of scales and exhibits numerous mechanisms of self-propulsion, it is unsurprising that multiple models have been developed to describe the dynamics of these systems. Figure 3 illustrates the principal computational models used to study active systems, highlighting key distinctions between different approaches. These include: dry models, where momentum is not conserved; wet models, which couples the system to a momentum-conserving fluid; microscopic models, focused on the dynamics of individual components; and continuum models, which describe the system using continuous variables such as velocity and density fields. The choice of model depends on the type of system being

Figure 3 – Different types of active matter models in micro-macro and dry-wet classifications. (a) Bubbly phase separation is shown for a continuum dry model, with boiling liquid in yellow and vapor in blue. (b) Vorticity field for a turbulent active fluid model. (c) Vibrated polar disks in confinement, with the colors indicating local alignment, ranging from red (parallel) to blue (anti-parallel) (d) Dipolar force flow field generated from a swimming bacteria (e) Schematic of the main computational models for active matter, with arrows indicating the direction of increased generalization, from microscopic dynamics to continuum and from dry system to those coupled with a solvent.

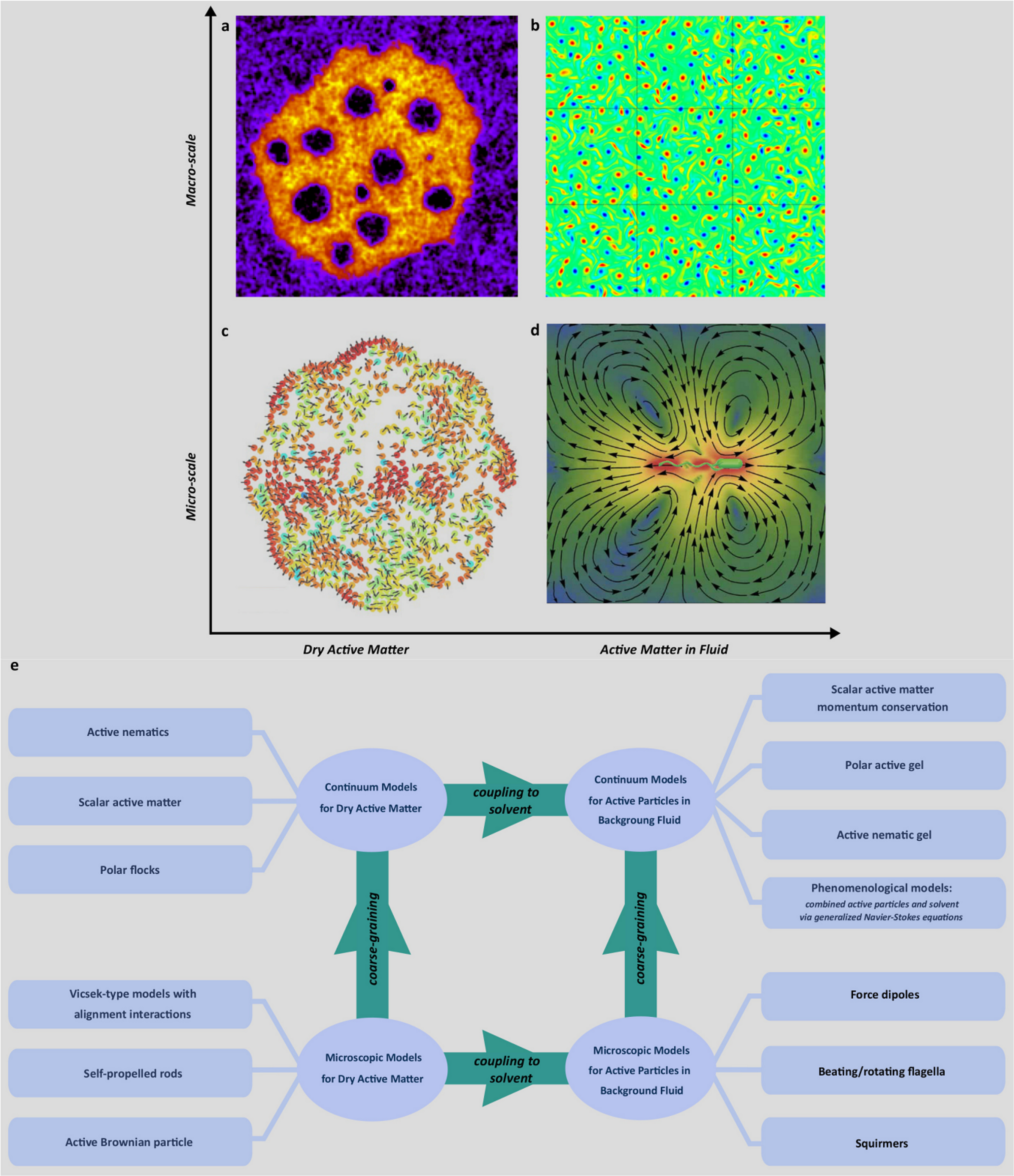

Source: (SHAEBANI et al., 2020)

studied and the specific characteristics of interest, as each model has its own unique strengths. As such, there is no universally superior model, only those that are more appropriate for a given case.

This thesis focuses on the study of microscopic dry active matter systems, where each component of the system is treated individually and explicit hydrodynamic interactions are neglected, meaning that momentum conservation does not apply. In such cases, the particle-fluid interactions are effectively modeled as a linear (i. e. Stokes) viscous friction force acting opposite to the direction of motion. This simplification is justified when fluid-mediated effects are less significant than thermal fluctuations and interparticle interactions, which is a common scenario when modeling the dynamics of dense flocks (CHATÉ, 2020). Within this context, there are also several other subcategories, mostly regarding how the particle reorients itself. A widely used approach, and the one employed here, is the active Brownian particle (ABP) model, in which the particle's orientation undergoes a rotational Brownian diffusion and is used to describe systems such as Janus particles (HOWSE et al., 2007; BUTTINONI et al., 2012). Other notable models include the run-and-tumble model, that features particles traveling along a single direction for a certain time before abruptly switching directions, which is a behavior observed in certain bacteria such as *E. coli* (TAILLEUR; CATES, 2008). Another prominent model is the Active Ornstein-Uhlenbeck model, where the velocity of a particle is no longer constant but follows a Ornstein–Uhlenbeck process, providing itself useful to model motion in viscous fluids (BONILLA, 2019; MARTIN et al., 2021). However, the general dynamics of the system are relatively indifferent to the model used, as the models have been shown to be largely equivalent in many cases (TAILLEUR; CATES, 2008; CATES; TAILLEUR, 2013), suggesting that the results derived in one model are applicable to others instead of being restricted to a single model.

1.3 SELF-ALIGNMENT

In systems where particles interact with one another or are subject to external potentials, the directions of a particle's heading and velocity can become decoupled when forces act upon it, such as during collisions. This separation in directions was explored as far back as (SHIMOYAMA et al., 1996), who, inspired by the gliding behavior of large birds, proposed that the heading and velocity vectors gradually relax to become parallel again over time. This process, later denoted *self-alignment*, offers a mechanism for integrating orientation dynamics into granular systems without the need for external control parameters like in the Vicsek model, which includes a certain neighborhood radius for each particle.

The self-alignment mechanism has since been extended and applied to various systems, including the study of tissue cell migration (SZABÓ et al., 2006), polar disks (DESEIGNE; DAUCHOT; CHATÉ, 2010; DESEIGNE et al., 2012; WEBER et al., 2013), and active solids (FERRANTE et al., 2013; GIOMI; HAWLEY-WELD; MAHADEVAN, 2013). In these contexts, the coupling between heading and velocity plays a crucial role in understanding collective phenomena, offering insights into a wide range of natural and synthetic systems. In experimental setups, the strength of this self-alignment effect can be estimated, for example, by finding the alignment length of individual components, and one way to control this is by adjusting the self-propulsion velocity of the particles. (BACONNIER et al., 2022)

Figure 4 – Illustration of the aligning mechanism for a system with self-alignment torque. From left to right, two particles with different orientations are in a collision course. As the particles start to interact, the directors become misaligned to the velocity. A self-aligning torque proportional to $\hat{\mathbf{n}} \times \mathbf{F}_{ij}$ arises and aligns those vectors, leaving the particles with equal orientations after the collision. This illustrates how an internal mechanism can induce global order in a system.

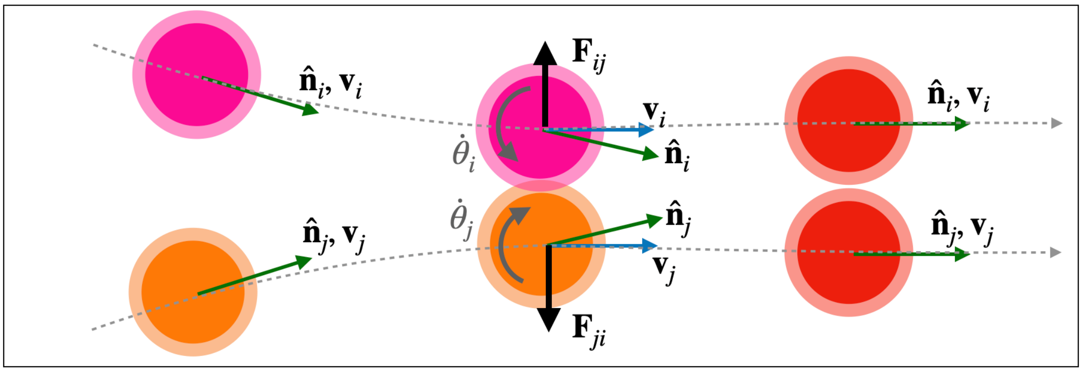

Source: (CANAVELLO et al., 2025) (adapted)

Figure 4 illustrates an example of how a self-alignment mechanism works. When two particles with initially parallel velocity $\mathbf{v}$ and orientation $\hat{\mathbf{n}}$ collide, represented by the overlap of their effective interaction ranges (shaded region), a repulsive force $\mathbf{F}_{ij}$ arises. This force induces a misalignment between each particle's velocity and orientation vectors. In response, a self-alignment torque, described by $\dot{\theta} \sim \hat{\mathbf{n}} \times \mathbf{F}_{ij}$, acts to restore alignment by rotating the orientation vector towards the velocity. As a result, the particles tend to leave the collision more aligned with each other than they were initially, demonstrating how collective alignment can emerge for a system without explicit alignment rules.

The realignment process that occurs during collisions competes with thermal diffusion, which acts to disrupt the alignment between particles over time. This interplay between both mechanisms plays a critical role in shaping the overall dynamics of the system. When alignment dominates, particles tend to organize into coherent, collectively moving structures, while stronger diffusion leads to disordered, random motion. Such a spectrum of behaviors is observed in numerous natural and synthetic systems, highlighting the relevance of these competing processes (BACONNIER et al., 2025).

1.4 STRUCTURE AND ORGANIZATION OF THIS WORK

This thesis explores the impact of self-alignment dynamics on both individual and collective behaviors in active matter systems, with a focus on the active Brownian particle model.

Chapter 1, the introduction, provides an overview of the history of active matter and outlines key models and phenomena that are characteristic of these systems.

Chapter 2 offers a brief description of the methods and tools employed to obtain the results presented in this work.

In Chapter 3, a review and derivation of established results for self-aligning particles in both free and confined systems is provided.

Chapter 4 presents new findings on the collective behavior of active matter systems under periodic boundary conditions. This chapter begins with a free system and then explores the effects of periodic obstacles, considering both isotropic and anisotropic configurations.

Chapter 5 introduces new results concerning the collective dynamics of active particles in harmonic confinement, including the construction of a phase diagram that categorizes the various emergent phases.

The final chapter, Chapter 6, offers a discussion of the results, as well as future research directions.

There are also two appendices: Appendix A, which provides detailed mathematical derivations used in Chapter 5, and Appendix B, that outlines some of the computational techniques used throughout this work.

2 MODEL AND METHODS

This chapter will include an overview of the mathematical and computational tools that were used. The active Brownian particle (ABP) model will be presented, along with details for the numerical integration of the Langevin equations of motion.

2.1 MODELING ACTIVE BROWNIAN PARTICLES

A two-dimensional system consisting of N identical spherical active Brownian particles is considered. The position and orientation of the i-th particle are denoted by $\mathbf{r}_i = (x_i, y_i)$ and $\hat{\mathbf{n}}_i = (\cos\theta_i, \sin\theta_i)$, respectively. An overdamped approximation is employed, which is valid in the regime where viscous forces dominate over inertial effects. This condition is commonly satisfied for micrometer-sized particles that self-propel in a fluid, where the particle mass is negligible relative to the viscous damping imposed by the surrounding medium (LÖWEN, 2020).

Under these assumptions, the equations of motion in the xy-plane are given by:

$$\dot{\mathbf{r}}_i = v_0\hat{\mathbf{n}}_i + \mu\mathbf{F}_i^{\text{tot}} + \sqrt{2D_T}\boldsymbol{\xi}_i(t), \tag{2.1a}$$

$$\dot{\theta}_i = \beta(\hat{\mathbf{n}}_i \times \mathbf{F}_i^{\text{tot}}) \cdot \hat{\mathbf{z}} + \sqrt{2D_R}\zeta_i(t), \tag{2.1b}$$

where the dot denotes the derivative with respect to time.

The parameter v_0 represents the self-propulsion speed, which is assumed to be constant and identical for all particles. This approximation is well justified for systems immersed in a viscous medium, as they quickly reach a fixed terminal velocity. Examples include biological microswimmers such as *E. coli* (BERG, 2004) and *T. tubifex* worms (SINAASAPPEL et al., 2025), as well as synthetic active particles such as catalytic Janus colloids (EBBENS et al., 2012). The translational and angular mobilities are denoted by μ and β, respectively, while the total force acting on a given particle is represented by $\mathbf{F}^{\text{tot}}$. The unit vector $\hat{\mathbf{z}}$ is defined as perpendicular to the plane of motion.

Stochastic contributions to the particle dynamics are modeled as additive Gaussian white noise. The translational and rotational noise terms, $\boldsymbol{\xi}_i(t)$ and $\zeta_i(t)$, have zero mean and are characterized by $\langle \xi_i^\alpha(t)\xi_j^\beta(t')\rangle = 2D_T\delta_{ij}\delta_{\alpha\beta}\delta(t-t')$ and $\langle \zeta_i(t)\zeta_j(t')\rangle = 2D_R\delta_{ij}\delta(t-t')$, where D_T and D_R are the translational and rotational diffusion coefficients, and $\alpha, \beta \in \{x, y\}$ stand for the Cartesian components.

The total force acting on particle i consists of contributions from external and interparticle interactions. It is given by

$$\mathbf{F}_i^{\text{tot}} = -\nabla V(\mathbf{r}_i) - \sum_{\substack{j=1\\ j\neq i}}^{N} \nabla U(|\mathbf{r}_i - \mathbf{r}_j|), \tag{2.2}$$

where $V(\mathbf{r}_i)$ denotes a position-dependent external potential, and $U(|\mathbf{r}_i - \mathbf{r}_j|)$ is the pairwise interaction potential between particles i and j. The first term represents forces due to external fields or confinement, while the second term accounts for interactions between particles.

The Weeks–Chandler–Andersen (WCA) potential is used to model interparticle interactions (WEEKS; CHANDLER; ANDERSEN, 1971). Derived from the Lennard-Jones potential, the WCA potential is obtained by truncating the Lennard-Jones interaction at its minimum, resulting in a purely repulsive potential. This formulation effectively captures excluded volume effects and is widely used in simulations of active matter systems where attractive interactions are negligible—for example, in dilute suspensions of microswimmers such as bacteria or synthetic colloidal particles (BIALKÉ; SPECK; LÖWEN, 2015; MARCHETTI et al., 2016). An additional advantage of the WCA potential is its continuity and differentiability, which make it well-suited for numerical simulations, unlike discontinuous potentials such as the hard-sphere model. The WCA potential is defined as

$$U_{\text{WCA}}(r) = \begin{cases} 4\varepsilon\left[(\sigma/r)^{12} - (\sigma/r)^{6}\right] + \varepsilon & \text{for } r \leq 2^{1/6}\sigma, \\ 0 & \text{for } r > 2^{1/6}\sigma, \end{cases} \tag{2.3}$$

where ε determines the strength of the repulsion, σ is the characteristic particle diameter, and the cutoff at $r = 2^{1/6}\sigma$ corresponds to the minimum of the original Lennard-Jones potential.

The term β controls the self-aligning strength, or restoring torque, of the particles, or how fast its orientation will change to match the force acting upon it, denoted by the cross product of $\hat{\mathbf{n}}$ and $\mathbf{F}^{\text{tot}}$. This term models a phenomena in which the heading and movement direction of a particle may not match, which can happen, for example, during collisions.

At low Reynolds numbers (corresponding to the laminar, non-turbulent regime) the translational and rotational diffusion constants D_T and D_R are related by the expression $D_R = 3D_T/\sigma^2$, which is directly derived from the Stokes-Einstein and Stokes-Einstein-Debye relations (KOENDERINK et al., 2003; KÖDDERMANN; LUDWIG; PASCHEK, 2008). This relation indicates that when the particles are small, which is the case in this study, then D_T will be considerably smaller than D_R. For instance, if σ is one fifth of a typical length scale of the system, such as the mean free path, then D_R will be about 75 times larger than D_T. Under these conditions, the translational diffusivity becomes negligible when compared to its rotational counterpart, which is supported by experimental observations that display this dominance of the rotational diffusivity (CATES; TAILLEUR, 2013). Based on these results, the translation diffusivity D_T will not be included in the analysis of collective dynamics analyzed in the following chapters, while the rotational diffusivity D_R will be referred to as simply D in that case.

2.2 NUMERICAL INTEGRATION OF THE EQUATIONS OF MOTION

For the simulations realized in this work, a second order stochastic Runge-Kutta method (also known as Heun's method) (GREINER; STRITTMATTER; HONERKAMP, 1988; BRAŃKA; HEYES, 1999) was implemented in C++ (STALLMAN; ROTHWELL, 2022) with a time step $\Delta t = 10^{-4}$. Cell linked lists were implemented to speed up the simulations (MATTSON; RICE, 1999), with details on the implementation described in Appendix B.

The Runge-Kutta algorithm can be described as follows for two dimensions

$$x_i(t+\Delta t) = x_i(t) + \frac{1}{2}(F^a_{i,x} + F^b_{i,x})\Delta t + u_i(t)\sqrt{2D_T\Delta t}, \tag{2.4a}$$

$$y_i(t+\Delta t) = y_i(t) + \frac{1}{2}(F^a_{i,y} + F^b_{i,y})\Delta t + v_i(t)\sqrt{2D_T\Delta t}, \tag{2.4b}$$

$$\theta_i(t+\Delta t) = \theta_i(t) + \frac{1}{2}(T^a_{i} + T^b_{i})\Delta t + w_i(t)\sqrt{2D_R\Delta t}, \tag{2.4c}$$

in which a and b denotes the state of the system at two different stages: a being the state at t and b being the state at $t + \Delta t$. The F and T terms are the force and torque that act in a particle at each time, which in this system are given by the deterministic parts of Eqs. 2.1, those being $F_i = v_0\hat{\mathbf{n}}_i + \mu\mathbf{F}^{\text{tot}}_i$ and $T_i = \beta(\hat{\mathbf{n}}_i \times \mathbf{F}^{\text{tot}}_i)\cdot\hat{\mathbf{z}}$, while the x and y subscripts indicate their projection along the Cartesian coordinates. The stochastic terms u_i, v_i and w_i are normally distributed random numbers with zero mean and unit variance.

The quantities at the intermediate step b can be found by performing a "virtual" step with the regular Euler-Maruyama method, which can be derived by first assuming a stochastic differential equation (HIGHAM, 2001)

$$dX_t = P(X_t, t)dt + Q(X_t, t)dW_t,$$

in which P and Q are, respectively, the deterministic drift and diffusion terms, while W_t denotes a Wiener process. Integrating over a time step $[t_n, t_{n+1}]$ results in

$$X_{t_{n+1}} = X_{t_n} + \int_{t_n}^{t_{n+1}} P(X_s, s)ds + \int_{t_n}^{t_{n+1}} Q(X_s, s)dW_s.$$

Approximating the integrands as constant over each time step, that is, $P(X_s, s) \approx P(X_{t_n}, t_n)$ and $Q(X_s, s) \approx Q(X_{t_n}, t_n)$, yields

$$X_{t_{n+1}} = X_{t_n} + P(X_{t_n}, t_n)\Delta t + Q(X_{t_n}, t_n)\Delta W_{t_n},$$

for a time step $\Delta t = t_{n+1} - t_n$.

Since $W_{t_{n+1}} - W_{t_n} = \Delta W_{t_n}$ is also a Wiener process, it has a mean of zero and a variance of $2D\Delta t$, where D denotes the diffusion coefficient. This allows the expression to be rewritten as $\Delta W_{t_n} \equiv \sqrt{2D\Delta t}\, u(t_n)$, with $u(t_n)$ once again representing a random Gaussian variable with zero mean and unit variance, i.e. $u(t_n) \sim \mathcal{N}(0, 1)$.

With this formulation, it becomes straightforward to generate the stochastic term ΔW_{t_n} computationally. This approach can be applied to the Langevin equation by identifying P as the sum of deterministic forces acting on a particle. These forces include self-propulsion, external potentials and interparticle interactions. Meanwhile Q can be set to unity since the particle's diffusivity is constant over time and space, and is already incorporated into the W_{t_n} term. While the first terms are the same as in the regular Euler method, the dependence on $\sqrt{\Delta t}$ is a characteristic of stochastic terms (MILSTEIN, 1995; SILVER, 2012).

2.3 SIMULATION PARAMETERS VALUES AND UNITS

Table 1 summarizes the numerical values of the system parameters used in the simulations conducted for this thesis, along with their corresponding units. The quantities β and D remain constant during each individual simulation and serve as the primary variables that were systematically varied across different simulations to explore the diverse behaviors exhibited by the system. Specifically, β was varied within the range $[0, 60]$, while D ranged from $[0, 10]$, depending on the phenomenon of interest for a given system.

The parameter L is used for the system studied in Chapter 4, where square boxes of size $L \times L$ with periodic boundary conditions are employed. Meanwhile, the parameter κ refers to the width of the confining harmonic potential, defined by $V(r) = \frac{1}{2}\kappa r^2$, which characterizes the system explored in Chapter 5.

The base units of time, length, and mass are frequently expressed in terms of ratios relative to fixed reference quantities which include, among others, v_0, μ, and κ. This approach allows for a more intuitive comparison across different systems and facilitates the interpretation of results within the context of the model parameters.

Table 1 – Summary of all key quantities in the system along with their typical numerical values as used in the simulations, unless otherwise specified. The parameter L applies to systems using periodic boundary conditions (Chapter 4), while κ is used for systems under harmonic confinement (Chapter 5). While the units of both β and D_R can include radians, it was not included as radians are not a physical unit.

System parameters and corresponding values used in simulations			
Quantity	Symbol	Numerical value	Unit
Self-propulsion velocity	v_0	1	length/time
Self-propulsion direction	$\hat{\mathbf{n}}_i$	Varies over time	Dimensionless vector
Total forces acting on a particle	$\mathbf{F}_i^{\text{tot}}$	Varies over time	mass · length/time^2
Translational mobility	μ	1	time/mass
Translational diffusion constant	D_T	0	length^2/time
Angular mobility	β	Simulation parameter	time/mass · length
Rotational diffusion constant	D_R	Simulation parameter	1/time
Particle size	σ	$0.1,\ 0.2$	length
Interaction potential well depth	ε	$0.1/4$	mass · length^2/time^2
Time step	Δt	10^{-4}	time
Periodic boundary size	L	$5,\ 10$	length
Harmonic well width	κ	1	mass/time^2

Source: The author (2025)

3 DYNAMICS OF A SINGLE ACTIVE PARTICLE WITH SELF-ALIGNMENT

In this chapter, a review of known results regarding a system consisting of a single active particle with self-alignment is conducted. This provides several exact results that are used to better understand the collective behavior presented in the following chapters.

3.1 FREE PARTICLE

If the system lacks any external potential or interactions, then $\mathbf{F}^{\mathrm{tot}} = 0$ and the equations of motion, given by Equations (2.1), reduce to

$$\dot{\mathbf{r}} = v_0\hat{\mathbf{n}} + \sqrt{2D_T}\boldsymbol{\xi}(t), \tag{3.1a}$$

$$\dot{\theta} = \sqrt{2D_R}\zeta(t). \tag{3.1b}$$

In this case, the alignment torque is not present. However, this system still shows interesting properties that are characteristic to ABPs. One of the peculiarities arises when calculating the mean square displacement of a particle. This can be done by starting with

$$\hat{\mathbf{n}} = \cos\theta\hat{\imath} + \sin\theta\hat{\jmath} \tag{3.2}$$

the autocorrelation matrix $\langle\hat{\mathbf{n}}(t)\hat{\mathbf{n}}(t')\rangle$ can then be calculated by using the statistical properties of $\theta(t)$, which include $\mathbb{E}[\theta(t)] = \theta(0)$ and $\mathrm{Cov}(\theta(t), \theta(t')) = 2D_R\min(t, t')$ (implying $\mathrm{Var}(\theta(t)) = 2D_R t$). This follows directly from the characteristics of a Wiener process with an arbitrary start point $\theta(0)$.

The first component of the matrix, $\langle\cos\theta(t)\cos\theta(t')\rangle$, can be simplified making use of the trigonometric identity

$$\cos\theta_t\cos\theta_{t'} = \frac{1}{2}\left(\cos(\theta_t + \theta_{t'}) + \cos(\theta_t - \theta_{t'})\right), \tag{3.3}$$

in which $\theta_t \equiv \theta(t)$ is used to avoid confusion caused by nested parentheses.

To find $\langle\cos(\theta_t \pm \theta_{t'})\rangle$, it is convenient to treat the cosine as the real part of a complex exponential function, i.e. $\cos(\theta_t \pm \theta_{t'}) = \Re\exp\{i(\theta_t \pm \theta_{t'})\}$. This approach simplifies the computation by making it essentially about finding the Fourier transform of a Gaussian function, which is itself another Gaussian:

$$\mathbb{E}[\exp(ikX)] = \frac{1}{\sqrt{2\pi\sigma^2}}\int_{\mathbb{R}} e^{ikx}e^{-\frac{(x-\mu)^2}{2\sigma^2}}dx = \exp\left(i\mu k - \frac{\sigma^2k^2}{2}\right),$$

in which X is a normal distribution with mean μ and variance σ^2, that is $X \sim \mathcal{N}(\mu, \sigma^2)^1$. By setting $k = 1$, it follows that $\mathbb{E}[\cos X] = \cos\mu \exp(-\sigma^2/2)$ and $\mathbb{E}[\sin X] = \sin\mu \exp(-\sigma^2/2)$. All that remains is to find the mean and variance of $\theta_t + \theta_{t'}$ and $\theta_t - \theta_{t'}$. For the first case, linearity of expectation gives $\mathbb{E}[\theta_t + \theta_{t'}] = 2\theta_0$ and propagation of variance results in $\mathrm{Var}(\theta_t + \theta_{t'}) = \mathrm{Var}(\theta_t) + \mathrm{Var}(\theta_t') + 2\,\mathrm{Cov}(\theta_t, \theta_{t'}) = 2D_R(t + t' + 2\min(t, t'))$. Doing a similar procedure for the second case yields $\mathbb{E}[\theta_t - \theta_{t'}] = 0$ and $\mathrm{Var}(\theta_t - \theta_{t'}) = 2D_R(t + t' - 2\min(t, t'))$. Applying these results to the expression above leads to

$$\begin{aligned}\langle \cos\theta_t \cos\theta_{t'} \rangle = \frac{1}{2}\{&\cos(0)\exp\left[-D_R(t + t' - 2\min(t, t'))\right] \\ &+ \cos 2\theta_0 \exp\left[-D_R(t + t' + 2\min(t, t'))\right]\}\,. \end{aligned} \tag{3.4}$$

Doing a similar procedure for all components leads to

$$\langle \hat{\mathbf{n}}(t)\hat{\mathbf{n}}(t') \rangle = \frac{1}{2}\begin{pmatrix} a_{11} & a_{12} \\ & \\ a_{21} & a_{22} \end{pmatrix} \tag{3.5}$$

with

$$\begin{aligned} a_{11} &= \exp\left[-D_R(t + t' - 2\min(t, t'))\right] + \cos 2\theta_0 \exp\left[-D_R(t + t' + 2\min(t, t'))\right], \\ a_{22} &= \exp\left[-D_R(t + t' - 2\min(t, t'))\right] - \cos 2\theta_0 \exp\left[-D_R(t + t' + 2\min(t, t'))\right], \\ a_{12} = a_{21} &= \sin 2\theta_0 \exp\left[-D_R(t + t' + 2\min(t, t'))\right]. \end{aligned}$$

Finding $\langle r_\alpha(t) r_\beta(t') \rangle$ requires integrating the equations of motion

$$\langle r_\alpha(t) r_\beta(t') \rangle = \int_0^t \mathrm{d}s_1 \int_0^{t'} \mathrm{d}s_2 \langle (v_0 \hat{n}_\alpha(s_1) + \sqrt{2D_T}\xi_\alpha(s_1))(v_0 \hat{n}_\beta(s_2) + \sqrt{2D_T}\xi_\beta(s_2)) \rangle. \tag{3.6}$$

For the sake of simplicity, and without loss of generality, the initial orientation is taken to be aligned with the x-axis, such that $\theta_0 = 0$. This is justified since the system is invariant under rotation and will simplify the analysis by causing the off diagonal elements in Equation (3.5) to vanish. Taking $t = t'$ to find the second moments provides

$$\langle r_\alpha^2(t) \rangle = \int_0^t \mathrm{d}s_1 \int_0^t \mathrm{d}s_2 \left[v_0^2 \langle \hat{n}_\alpha(s_1) \hat{n}_\alpha(s_2) \rangle + 2D_T \langle \xi_\alpha(s_1) \xi_\alpha(s_2) \rangle \right], \tag{3.7}$$

with the cross terms going to 0 since ξ_α has zero mean.

---

[1] This process is known in statistics as finding the *characteristic function* of a given probability density function, in this case the normal distribution.

Evaluating the integrals gives

$$\langle x^2(t)\rangle = v_0^2\left[\frac{t}{D_R}+\frac{1}{12D_R^2}\left(e^{-4D_Rt}+8e^{-D_Rt}-9\right)\right]+2D_Tt, \tag{3.8a}$$

$$\langle y^2(t)\rangle = v_0^2\left[\frac{t}{D_R}-\frac{1}{12D_R^2}\left(e^{-4D_Rt}-16e^{-D_Rt}+15\right)\right]+2D_Tt, \tag{3.8b}$$

which is the mean-square displacement (MSD) in each direction. The radial MSD is given by $\langle r^2(t)\rangle = \langle x^2(t)\rangle + \langle y^2(t)\rangle$, resulting in

$$\langle r^2(t)\rangle = 4D_Tt+\frac{2v_0^2}{D_R}t+\frac{2v_0^2}{D_R^2}\left(e^{-D_Rt}-1\right), \tag{3.9}$$

which is a well known result (BECHINGER et al., 2016; BREONI; SCHMIEDEBERG; LÖWEN, 2020). Notably, setting $v_0=0$ recovers the result for a passive particle, as expected. At large times, i.e. $t \gg D_R^{-1}$, the linear terms dominate and $\langle r^2(t)\rangle \simeq 4\left(D_T+\frac{v_0^2}{2D_R}\right)t = 4D_{\text{eff}}t$, indicating that the activity provides a correction to the particle's diffusivity[2]. Meanwhile for sufficiently short times, the MSD can be approximated by the expansion

$$\langle r^2(t)\rangle = 4D_Tt+v_0^2t^2-\frac{1}{3}v_0^2D_Rt^3+\frac{1}{12}v_0^2D_R^2t^4+\mathcal{O}(t^5), \tag{3.10}$$

showing diffusive behavior for the D_T term, while the activity terms, given by the self-propulsion velocity v_0, show ballistic motion.

If the MSDs are computed individually for each direction instead, a similar regime for $t \gg D_R^{-1}$ is seen, with

$$\langle x^2(t)\rangle = \langle y^2(t)\rangle \simeq \left(2D_T+\frac{v_0^2}{D_R}\right)t = 2D_{\text{eff}}t, \tag{3.11}$$

which is half of the radial MSD as expected. At short times, the expansion is

$$\langle x^2(t)\rangle \approx 2D_Tt+v_0^2t^2-v_0^2D_Rt^3+\frac{11}{12}v_0^2D_R^2t^4+\mathcal{O}(t^5), \tag{3.12a}$$

$$\langle y^2(t)\rangle \approx 2D_Tt+\frac{2}{3}v_0^2D_Rt^3-\frac{5}{6}v_0^2D_R^2t^4+\mathcal{O}(t^5), \tag{3.12b}$$

showing a strong anisotropy between the directions at low t. Since it was assumed that the particle was initially aligned with the x direction at $t=0$ ($\theta(0)=0$), it has terms of order t^2 for x while the y direction only has terms of order t^3, besides the passive noise. Note that for $\theta(0)=\pi$ the results obtained are the same, as the system only depends on $2\theta(0)$. Meanwhile setting $\theta(0)=\pm\pi/2$ is equivalent to swapping the values of a_{11} and a_{22} in matrix (3.5), indicating that the anisotropy will be in the y direction instead of x.

---

[2] This correction can be generalized for higher dimensions as $D=v_0^2/d(d-1)D_R$ (CATES; TAILLEUR, 2013)

This result demonstrates that, at early times, the particle predominantly moves in the direction of its initial alignment, with significantly less motion in the perpendicular direction. Over time, however, the particle eventually decorrelates and begins to diffuse in a manner similar to that of a passive particle. In this sense, the particle's activity is most pronounced at short timescales, as it behaves like a passive particle at longer timescales.

Another quantity that can be evaluated is the variance along each axis, $\sigma_\alpha^2 = \langle \alpha^2 \rangle - \langle \alpha \rangle^2$. This require knowing the average displacements, which are readily found with

$$\langle \mathbf{r}(t) \rangle = \begin{pmatrix} \int_0^t \mathrm{d}s \langle v_0 \hat{n}_x(s) + \sqrt{2D_T}\xi_x(s) \rangle \\ \\ \int_0^t \mathrm{d}s \langle v_0 \hat{n}_y(s) + \sqrt{2D_T}\xi_y(s) \rangle \end{pmatrix} = \begin{pmatrix} \int_0^t \mathrm{d}s \left[v_0 \langle \cos\theta(s) \rangle + \sqrt{2D_T} \langle \xi_x(s) \rangle \right] \\ \\ \int_0^t \mathrm{d}s \left[v_0 \langle \sin\theta(s) \rangle + \sqrt{2D_T} \langle \xi_y(s) \rangle \right] \end{pmatrix} \tag{3.13}$$

The integrals over noise evaluate to 0, and using the results of $\mathbb{E}[\cos X]$ and $\mathbb{E}[\sin X]$ to evaluate the integrands gives

$$\langle \cos\theta \rangle = e^{-D_R t}, \tag{3.14a}$$

$$\langle \sin\theta \rangle = 0. \tag{3.14b}$$

Substituting it back and performing the integral

$$\langle \mathbf{r}(t) \rangle = \begin{pmatrix} \frac{v_0}{D_R}\left(1 - e^{-D_R t}\right) \\ \\ 0 \end{pmatrix} \tag{3.15}$$

In this case $\sigma_y^2 = \langle y^2 \rangle$ which was already found, while

$$\langle \sigma_x^2 \rangle = v_0^2 \left[\frac{t}{D_R} + \frac{1}{12 D_R^2} \left(e^{-4D_R t} - 12 e^{-2D_R t} + 32 e^{-D_R t} - 21 \right) \right] + 2D_T t.$$

Interestingly, the expansion yields

$$\sigma_x^2 \approx \frac{1}{3} v_0^2 D_R^2 t^4 - \frac{7}{15} v_0^2 D_R^3 t^5 + \mathcal{O}(t^6), \tag{3.16}$$

once again demonstrating a significant anisotropy with far more variance on y at early times, since $\sigma_y^2 \sim t^3$ while $\sigma_x^2 \sim t^4$, not taking into account the D_T term. This type of anisotropy related to the activity has been studied before in (BASU et al., 2018).

3.2 PARTICLE UNDER HARMONIC CONFINEMENT

The behavior of confined active matter is a topic of considerable interest since many real world systems are subject to some form of confinement. By investigating the complex behaviors that arise from the coupling between inherently non-equilibrium properties and confinement, valuable insights of realistic systems can be obtained. Even under seemingly simple cases such as harmonic confinement, a wide range of phenomena has been studied, such as non-Boltzmann distributions in the steady state and re-entrant transitions back to passive-like states (POTOTSKY; STARK, 2012; HENNES; WOLFF; STARK, 2014; MALAKAR et al., 2020; WEXLER et al., 2020; CHAUDHURI; DHAR, 2021). Experimental realizations have been also carried out with acoustic (TAKATORI et al., 2016) and optical (SCHMIDT et al., 2021) confinements, which corroborate theoretical results and demonstrate interest in these types of systems.

When including self-alignment torque to the system dynamics, the behavior changes even at single particle level. This can be seen when adding a harmonic confining potential of the form $V(r) = \frac{1}{2}\kappa r^2$ (so that $\mathbf{F}^{\text{tot}} = -\nabla V = -\kappa \mathbf{r}$) to Equations (2.1) and rewriting them as

$$\dot{\mathbf{r}} = v_0 \hat{\mathbf{n}} - \mu\kappa r \hat{\mathbf{r}} + \sqrt{2D_T}\boldsymbol{\xi}_i(t), \tag{3.17a}$$

$$\dot{\theta} = \beta r \kappa \sin(\theta - \varphi) + \sqrt{2D_R}\zeta_i(t), \tag{3.17b}$$

in which φ is the polar angle of the particle measured from the x axis.

In the absence of noise, that is when $D_T = D_R = 0$, an analytical solution be obtained by projecting the equation onto polar coordinates and introducing a tilt angle $\chi \equiv \theta - \varphi$

$$\dot{r} = v_0 \cos\chi - \mu\kappa r, \tag{3.18a}$$

$$r\dot{\varphi} = v_0 \sin\chi, \tag{3.18b}$$

$$\dot{\theta} = \beta r \kappa \sin\chi. \tag{3.18c}$$

These equations admit a trivial steady state solution given by $\dot{r} = \dot{\varphi} = \dot{\theta} = 0$, defining the climbing state. In this phase, the particle simply ascends the potential until the local gradient matches its own self-propulsion force, after which it remains in a stationary position defined by a radius $r = v_0/(\mu\kappa) = R_{\text{CI}}$. This radius defines a critical isoforce line, or critical isocline, denoting a boundary for which particles in the noiseless regime cannot cross from the inside out.

Another distinct regime comes from the solution given by $\dot{r} = 0$ and $\dot{\chi} = 0$. These conditions imply $\dot{\varphi} = \dot{\theta} = \omega$, a constant, and the particle satisfies

$$R_\circ = \sqrt{\frac{v_0}{\beta\kappa}}, \tag{3.19a}$$

$$\omega = \beta\kappa R_\circ \sqrt{1 - \left(\frac{\mu\kappa}{v_0}\right)^2 R_\circ^2} = \sqrt{v_0\beta\kappa - (\mu\kappa)^2}, \tag{3.19b}$$

$$\chi = \arccos\left(\frac{\mu\kappa R_\circ}{v_0}\right) = \arccos\left(\mu\sqrt{\frac{\kappa}{v_0\beta}}\right), \tag{3.19c}$$

which defines a circular motion with constant radius $R_\circ$ and angular speed ω, dubbed the orbiting phase.

For the particle to enter the orbiting phase, it is necessary for ω to be real, which requires that $\beta \geq \beta^* = (\mu\kappa)^2/v_0$. Once this condition is true, all fixed points, which define the critical isocline, become unstable at once, and the system transitions into the orbiting state. At $\beta = \beta^*$, the orbit will have the same radius as the critical isocline, that is $R_\circ = R_{\mathrm{CI}}$. This is consistent with a physical interpretation of the system, as the orbit radius cannot be larger than the isocline since the particle is unable to enter that region (DAMASCENA; CABRAL; SILVA, 2022).

Experimental realizations of this system have also been conducted with robotic agents confined in harmonic traps, as done by Dauchot and Démery (2019). In this study, a HexBug robot of about 5cm displays both climbing and orbiting states, with transitions between those regimes occurring when the robot's battery drops below a certain level (which can be understood as a drop in v_0). The stochastic components inherent to real life experiments introduce some changes in the system, including the diffusion along the azimuthal direction on the climbing regime and spontaneous inversions of direction for the orbiting regime. This can be seen in Figure 5, which presents the experimental results for the system. Panels (b) and (c) display the azimuthal velocity for each state. In the climbing state, the velocity shows a noisy distribution around 0, indicating azimuthal diffusion. In the orbiting state, the velocity switches between negative to positive values, reflecting the spontaneous inversions in direction.

These findings have been extended to other confinement geometries by Damascena, Cabral and Silva (2022), including anisotropic harmonic and anharmonic potentials. In this case, the critical isocline stops being a circle and the fixed points no longer become unstable at the same value of β, in general. This might result in, for example, particles accumulating along the major axis in an elliptical potential. The orbital regimes also change into more complex shapes, such as ovals and lemniscates. Figure 6 illustrates several orbits for increasingly elliptical potentials.

Figure 5 – Experimental results for a hexbug trapped in harmonic confinement. (a-c) Climbing regime showing the robots pointing outwards the potential and diffusing laterally. (d-f) Orbiting regime, showing rotation around the potential minimum and inversions in direction. (a, d) Trajectories of the robots (b, e) Azimuthal velocity (c, f) Probability distribution function of the azimuthal velocity.

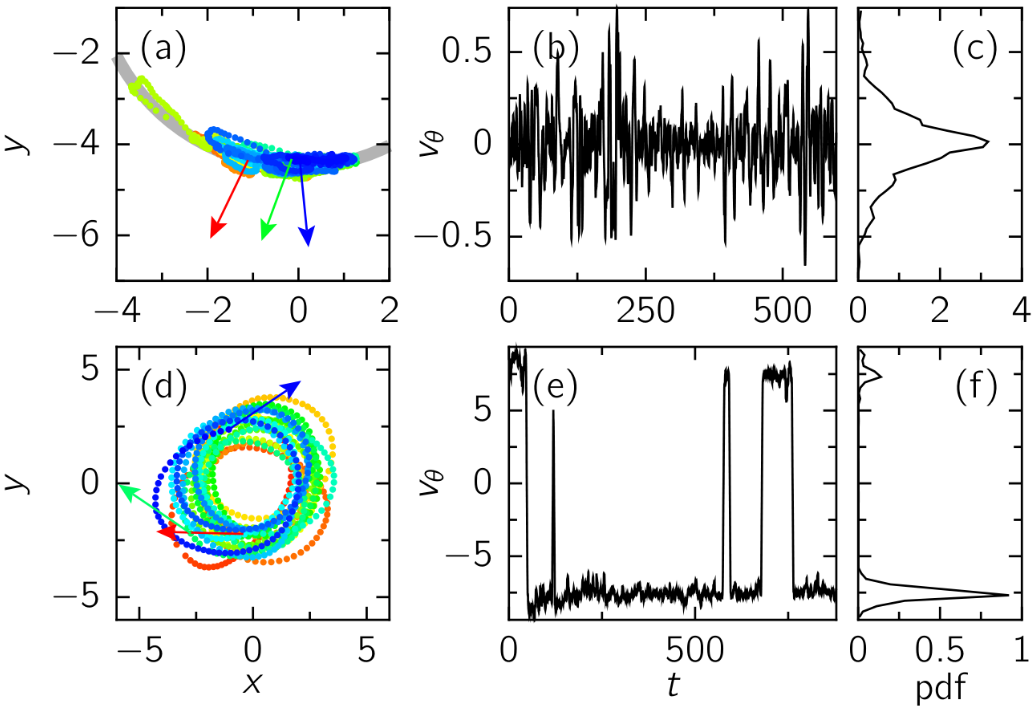

Source: (DAUCHOT; DÉMERY, 2019)

In these systems, it was reported that for an even number of crossings, $\hat{\mathbf{n}}$ completes full rotations in a period, hence the R label. In contrast for an odd amount of crossings, $\hat{\mathbf{n}}$ will oscillate in librational motion without completing a full rotation, and thus the L label. Another thing of note is that the clockwise and anti-clockwise orbits are distinct from each other, instead of overlapping like in the circular case. Additionally noise effects can induce transition between coexisting orbits (DAMASCENA; SILVA, 2023).

Figure 6 – (a-d) Representative orbits for different elliptical potentials, of the form $V(x,y) \sim (1+\epsilon)x^2 + y^2$. (e) Phase diagram in the $\beta - \epsilon$ plane, with the (a-d) panels indicated. Background colors indicate the topological state of the orbit, with light peach being used for rotation (R) and coral for libration (L). The subscript indicates the number of crossings. The full and dashed lines indicate transitions when sweeping ϵ at fixed β.

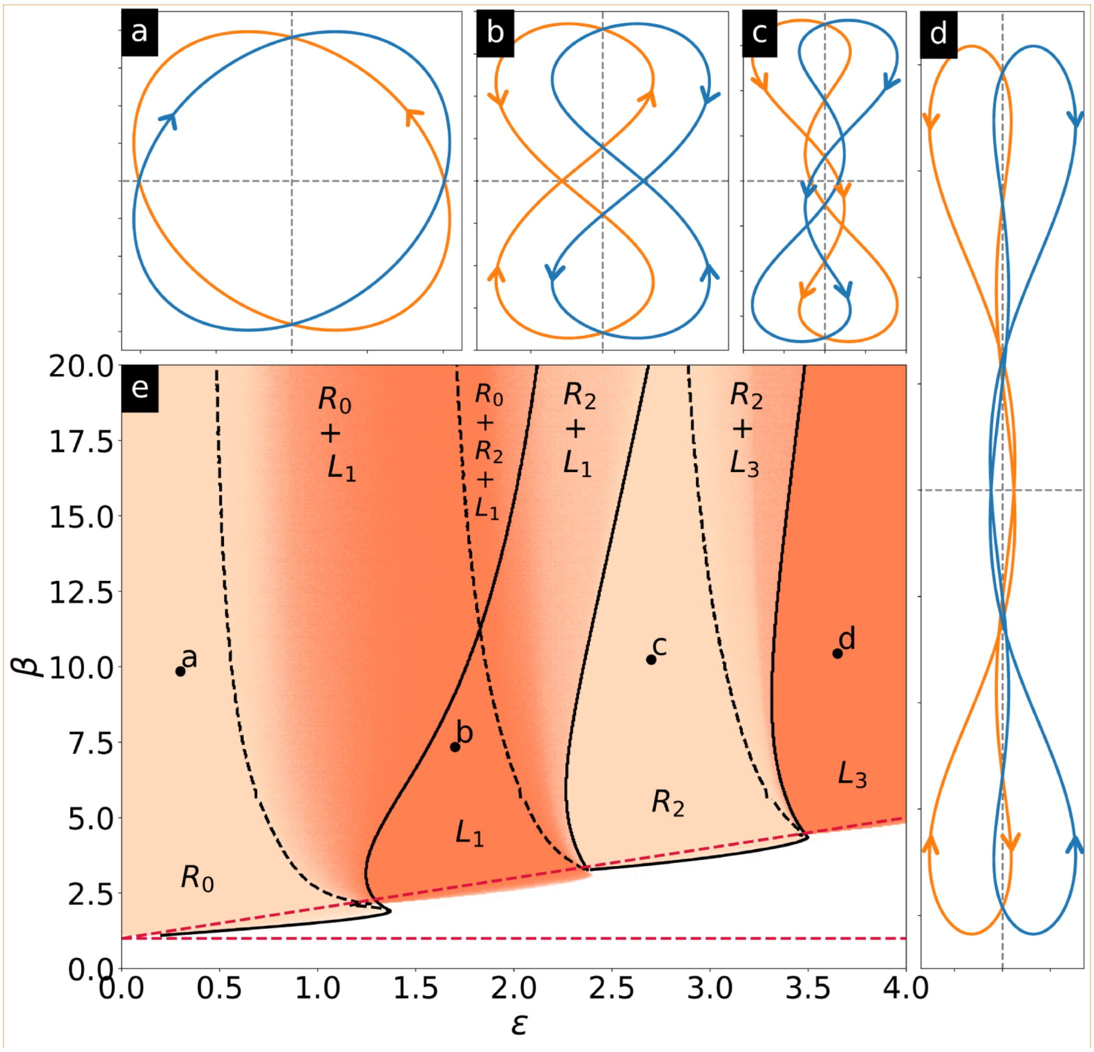

Source: (DAMASCENA; CABRAL; SILVA, 2022)

4 INTERACTING ACTIVE MATTER UNDER PERIODIC BOUNDARY CONDITIONS

This chapter will explore a system of active matter with steric interactions without a confining potential. By looking at a system with no obstacles and finite noise, a polarization condition is established and a critical value for the torque β to achieve it is defined, which depends on both the thermal noise and density of the system. Next, by introducing an isotropic periodic substrate to the system, the flock shows a locking along the substrate symmetry directions, which becomes more pronounced as the obstacle density grows larger, however the polarization conditions remain largely unchanged. By making the substrate anisotropic, a transition from two-dimensional motion to one-dimensional is seen, as the system separates into lanes that only move along one direction.

The results presented in this chapter were originally published in the article (CANAVELLO et al., 2025).

4.1 COLLECTIVE BEHAVIOR OF SELF-ALIGNING ACTIVE SYSTEMS

A fundamental question that arises when introducing a self-aligning torque into active matter systems is how the dynamics of interacting particles will be altered by this additional feature. Active matter systems, even in their simplest forms, exhibit a rich and diverse phenomenology, making this an intriguing area of study. For instance, motility-induced phase separation (MIPS) serves as an example of non-trivial behavior in minimal models (FILY; MARCHETTI, 2012; REDNER; HAGAN; BASKARAN, 2013; CATES; TAILLEUR, 2015; GEYER et al., 2019). In such systems, the interplay of active motion and repulsive interactions leads to the spontaneous formation of dense and dilute phases, even without attractive or aligning interactions, and can even show emergent velocity alignment (CAPRINI; MARCONI; PUGLISI, 2020). These observations suggest that the introduction of self-aligning torques may add yet another layer of complexity to the already intricate behavior of active matter systems.

When a self-aligning torque is present the system, that is $\beta > 0$, particles will change their orientation during collisions, with the speed of said change being directly proportional to β. It is anticipated that after the particles have undergone a sufficient number of collisions with one another, the system will become polarized, with all particles pointing in a single direction, similar to the behavior observed in Vicsek systems. An example of both the unpolarized and polarized states for a system can be seen in Figure 7 for a system with $N = 480$ particles and $D = 0.01v_0/\sigma$. It is useful to define a filling fraction as $f = NA_{\text{part}}/L^2$, in which $A_{\text{part}} = \pi(2^{\frac{1}{6}}\sigma/2)^2$ is the area occupied by a particle with the Weeks-Chandler-Anderson potential and L^2 is the total available area for the particles, which is a $L \times L$ square with periodic boundary conditions. This definition gives a filling fraction of $f \simeq 0.19$ for the system in Figure 7, which has $\sigma = 0.1$ and $L = 5.0 = 50\sigma$.

Figure 7(a) shows a system with $\beta = 0.1$ in the unpolarized state, so each particle has a different color indicating their distinct headings [1]. In Figure 7(b), $\beta = 0.6$ and the system is fully polarized, so each particle has the same color indicating the entire system is moving in the same direction, giving the center of mass of the system a finite speed. In what follows, a calculation of the critical value of β_c will be demonstrated, and the value found for this system is about $\beta_c \simeq 0.14$.

This order is broken by the random noise D, creating a competition between the time it takes to achieve polarization, τ_P (which is proportional to β^{-1}) and the persistence time of the system τ_D which measures how long it takes for the thermal noise to significantly alter the particle's trajectory. A condition for full polarization can then be established as $\tau_P < \tau_D$.

Figure 7 – Snapshots of particles for two different values of β for a system with $f = 0.19$ and $D = 0.01$ with (a) showing an unpolarized state with $\beta = 0.1 < \beta_c$ (b) showing a polarized state with $\beta = 0.6 > \beta_c$. The colorhweel indicates the internal orientation θ of the particles.

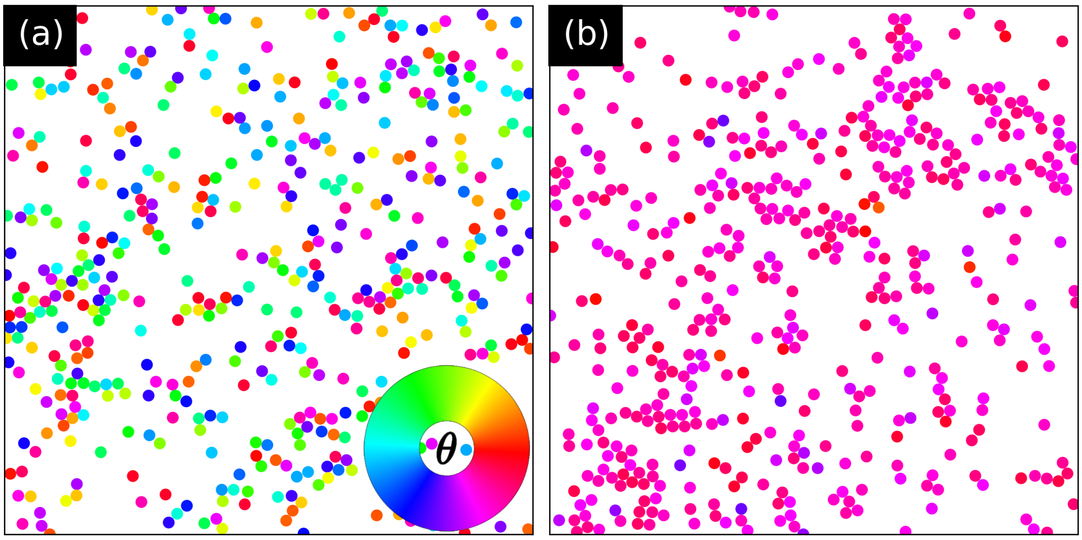

Source: (CANAVELLO et al., 2025) (adapted)

For ABPs, the timescale over which thermal noise decorrelates the particle's orientation is inversely proportional to D, that is $\tau_D \sim D^{-1}$ (BASU et al., 2018). To find an estimate for τ_P,

---

[1] For simplicity, β and D will be expressed in units of μ/σ and v_0/σ from here on.

it helps to first express it as a product of the number of collisions required for full polarization, N_{col} with the average collision time τ_{col}. The latter is defined as the mean free path divided by the particle speed i.e. $\tau_{\text{col}} = (\sigma f v_0)^{-1}$ with $n \equiv N/L^2$ being the system density. To find an estimate for N_{col} it is useful to look at the angular deflection a single collision will have, denoted by $\delta\theta$, then assuming that a particle starts out misaligned, the number of collisions required to align it will be of the order $N_{\text{col}} \sim \delta\theta^{-1}$. Looking at Eq. (2.1b) to find an estimate for $\delta\theta$ it can be noted that $\delta\theta \sim \beta F \delta t$ and from Eq. (2.1a), $F \sim v_0/\mu$. Combining these results, $\delta\theta \sim \beta(v_0/\mu)\delta t \sim \beta\sigma/\mu$. With these results in mind, the polarization condition becomes

$$\tau_P < \tau_D, \tag{4.1a}$$

$$N_{\text{col}}\tau_{\text{col}} < D^{-1}, \tag{4.1b}$$

$$(\mu/\beta\sigma)(L^2/N\sigma v_0) < D^{-1}, \tag{4.1c}$$

$$\mu L^2/(\beta N \sigma^2 v_0) < D^{-1}, \tag{4.1d}$$

to find a critical value of β, denoted by β_c the inequality turns into an equality

$$\beta_c \sim \mu D/(v_0 f), \tag{4.2}$$

with f being the filling fraction. This means that, up to a constant factor, it is possible to see how variations of the parameters will affect β_c. Similar scaling arguments have also been made for Vicsek systems (GINELLI, 2016, Section 3.1).

To validate this simple scaling estimate of β_c, direct simulations of the equations of motion in Equations (2.1) were carried out, using uniformly distributed random initial conditions for the position and orientation. In Figure 8 the average velocity of the center-of-mass, defined as $\bar{\mathbf{v}} = \frac{1}{N}\Sigma_i \mathbf{v}_i$, is plotted against scaled datasets of (a) β/D at constant f and (b) βf at constant D. A collapse of the curves is seen on both cases, indicating that the behavior of β_c depending on D/f is indeed correct. An universal numerical estimate for the scaled value of β_c was determined by locating the inflection point of each curve, defined as the point where the (numerical) derivative of the curve reaches its maximum value, and either multiplying it by f for the curves on panel (a) or dividing it by D for the curves on panel (b). By averaging the value found across all curves, the result found was $\beta_c \simeq 2.7\mu D/(v_0 f)$, which is represented as a dashed vertical line in both panels.

Figure 8 – System polarization $\langle\bar{v}\rangle$ versus: (a) β/D for various D at fixed filling fraction $f = 0.10$, and (b) βf for different filling fractions at fixed $D = 0.01$. Each point represents the average polarization after $100\sigma/v_0$ time units for 100 realizations of random noise, with error bars showing the standard deviations from the mean. Closed symbols correspond to a system with size $L = 50\sigma$, while open symbols represent a system four times larger in area $(L = 100\sigma)$. The dashed vertical line marks the numerical estimate for β_c.

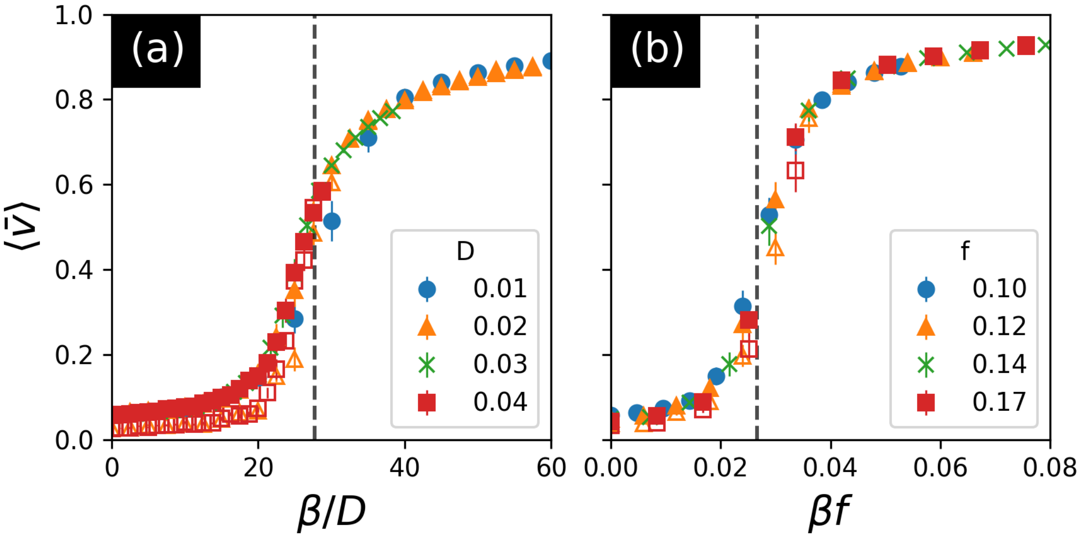

Source: (CANAVELLO et al., 2025)

4.2 COLLECTIVE MOTION IN A SQUARE ARRAY OF OBSTACLES

An important feature when modeling realistic systems is the influence of a substrate on system dynamics, as most natural and experimental environments will exhibit some degree of non-homogeneity (VOLPE et al., 2011). The introduction of periodic obstacles has been shown to, for example, screen the interaction between fish, disturbing the formation of schools above a certain obstacle density (VENTÉJOU et al., 2024). Moreover, in the presence of asymmetric substrates, ratchet effects can emerge, leading to direct transport even in the absence of external drives (REICHHARDT; REICHHARDT, 2017).

By introducing obstacles to the system, which are treated as immobile particles (thus possessing the same interaction properties), it can then be determined if, and how, the addition of obstacles to the system will affect the polarization condition established before. The number of obstacles, or posts, is denoted by N_p, while N will represent only the number of motile particles. Figure 9(a)-(c) presents three different systems with varying obstacle densities with $N = 240, D = 0.01$ and $\beta = 1.0$. This value of β guarantees that the system will polarize, according to the critical polarization condition found above. A finite value of noise is also desirable to avoid possible jammed states in the system.

The post densities (depicted as black dots) are, respectively, 4×4, 8×8 and 16×16, equally uniformly distributed in a square array for a system with $L = 50\sigma$. The system can still achieve total polarization but particles will suffer more collisions with posts which impacts their terminal velocity. In Figure 9(d) the polarization is plotted against β for various densities and the inflection point occurs at roughly the same point (note that using the calculations detailed in the previous section the value of $\beta_c \simeq 0.28$, which matches well with the data) but the final velocity for systems with obstacles is lower than the free case due to the increasingly frequent collisions with obstacles.

Figure 9 – (a) - (c) Square arrays of obstacles for different obstacle densities, in order, $N_p = 4 \times 4$, 8×8 and 16×16 for a system with $D = 0.01$, $\beta = 1.0$, $L = 50\sigma$ and 240 mobile particles. The colors indicate the particles orientations, with black indicating posts. (d) System polarization for different post array densities. The value of β in which the transition occurs remains unchanged as the density varies, however the velocity drops. Error bars indicate standard deviations obtained from 50 realizations of random noise.

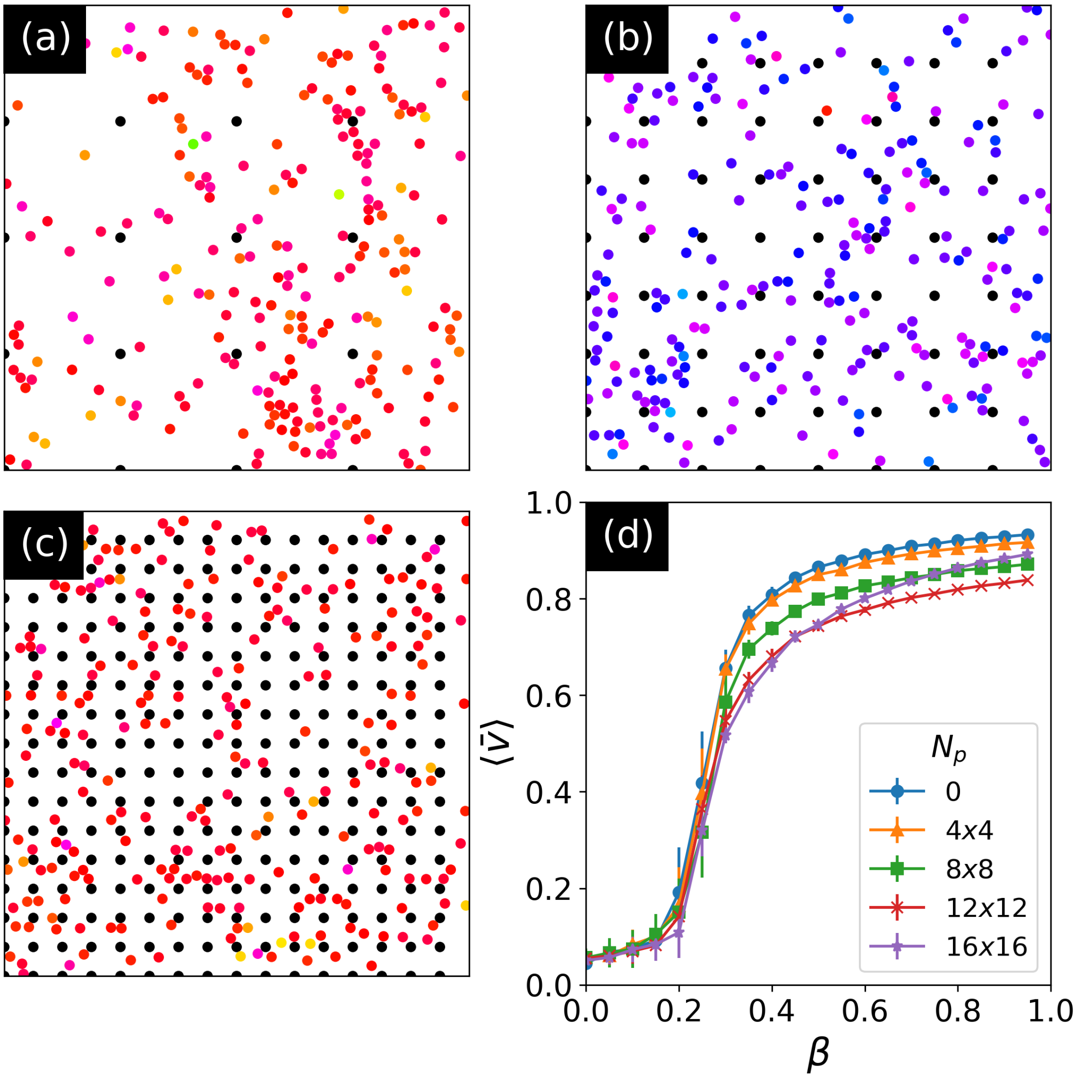

Source: (CANAVELLO et al., 2025) (adapted)

Figure 10 shows a histogram of the directions for a system with $N = 240$, $\beta = 1.0$ and $D = 0.01$ (thus satisfying the polarization condition) over 360 realizations of random noise. The left column shows the directions of individual particles, while the right one has the direction of the total polarization vector, defined as $\mathbf{M} = \frac{1}{N}\Sigma_i \hat{\mathbf{n}}_i$. By increasing the post density, a locking along the symmetry directions becomes more pronounced, and similar directional locking effects have been studied in run-and-tumble particles in a periodic substrate (REICHHARDT; REICHHARDT, 2020). In Figure 10(g, h), showing the 16×16 array, the system as a whole only moves in multiples of $90°$, while individual particles still have small peaks around multiples of $45°$, which indicate transitions into neighboring lanes. The direction locking comes from a combination of the particle collisions causing all particles to assume the same direction and the obstacle substrate filtering the particles to only move along its symmetry directions. It is noteworthy that by replacing posts with dissenters, defined as ABPs without alignment interactions, even a small fraction of those can disrupt the flocking behavior of the system (YLLANES; LEONI; MARCHETTI, 2017).

Figure 10 – Normalized histograms of (a, c, e, g) probability distribution of individual particles directions θ_i (b, d, f, h) probability distribution of the mean direction of motion of the system θ_M. (a, b) Isotropic case with no obstacles (c, d) 4×4 obstacle array, which shows a weak directional locking (e, f) 8×8 obstacle array showing a stronger direction lock (g, h) 16×16 obstacle array showing a system that can only move along the symmetry directions. Computed over 360 realizations for a system with $D = 0.01$, $\beta = 1.0$, $L = 50\sigma$ and 240 mobile particles. The dashed lines indicate multiples of $90°$.

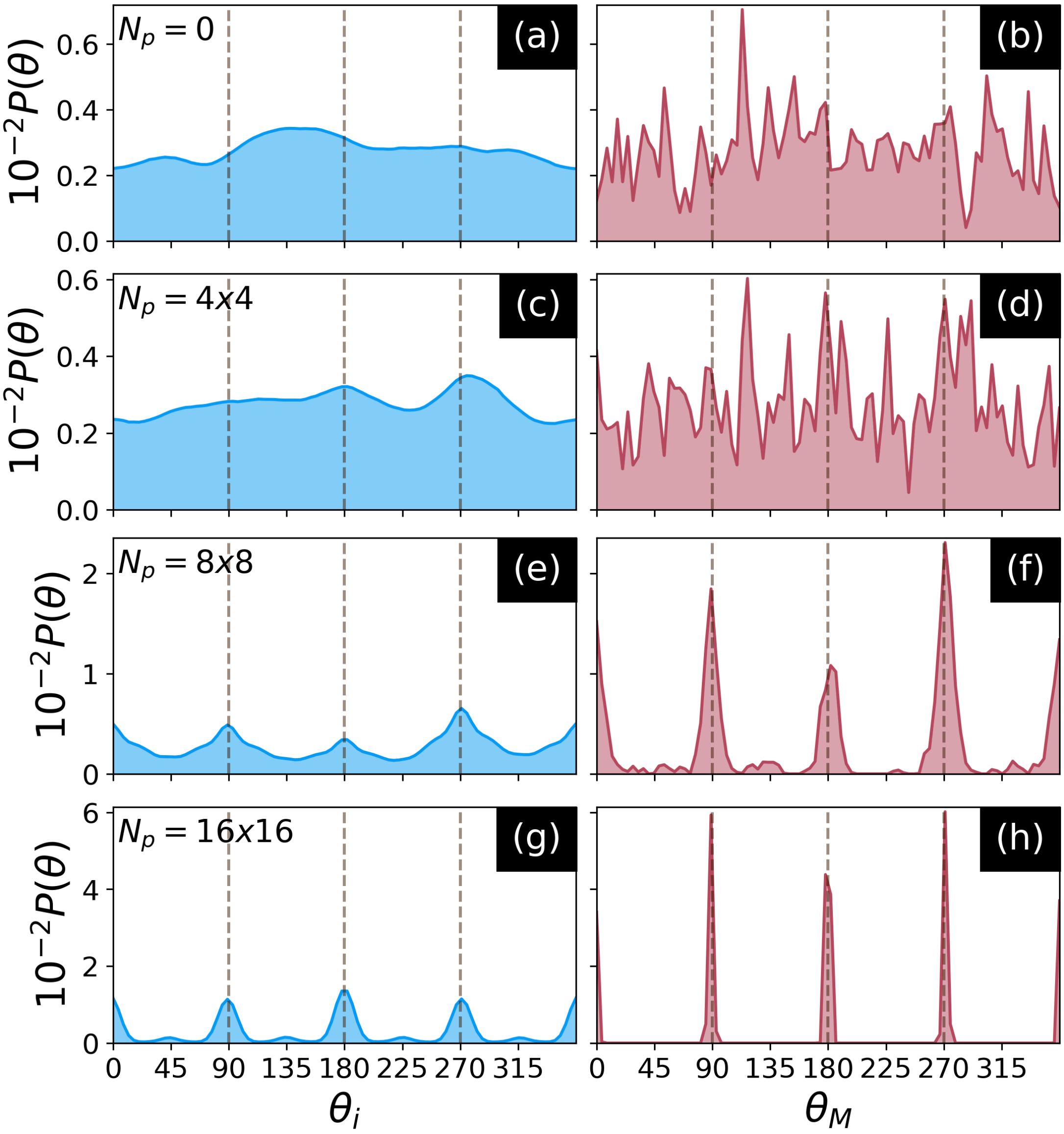

Source: (CANAVELLO et al., 2025)

4.3 ANISOTROPIC ARRAYS OF OBSTACLES

By keeping the amount of obstacles in the y direction, denoted by $N_{p,y}$, constant while varying the number of obstacles in the x direction, denoted by $N_{p,x}$, rectangular arrays of varying ratios can be constructed. In Figure 11 snapshots of each phase, along with a schematic phase diagram, are shown for a system with fixed $N_{p,y} = 8$. The quasi-isotropic case, represented by Figure 11(a), displays a system with some anisotropy at $N_{p,x} = 14$, but the global polarization θ_M can still assume any of the four symmetry directions of the array, demonstrated by the system being able to move upwards.

By increasing the anisotropy ratio further, the system transitions into a quasi-1D state, in which particles segregate into "lanes" that move along the x axis. Although each lane (of which there are 8, the same number as $N_{p,y}$) only moves into one direction, individual particles can still hop between them vertically, which is why the lanes stay coupled and may have different densities between each other. This creates a behavior in which neighboring lanes tend to move in the same direction, but distant neighboring lanes might have opposite directions. Figure 11(b) demonstrates one such system at $N_{p,x} = 22$, with two densely packed lanes followed by sparsely populated lanes and a moderately packed lane moving in the opposite direction.

When the spacing between obstacles is smaller than the particle size σ, particles can no longer jump to different lanes, effectively making it so each lane will be isolated. As the initial positions are uniformly distributed, each lane will have an equal and constant density over time. The lanes then polarize in either the $-x$ or $+x$ direction, which is seen in Figure 11(c) for a system with $N_{p,x} = 26$. This phase is also marked by an increase in relaxation time required for the system to reach a steady flow, since lanes can form transient jammed, or clogged, states. This phenomenon is seen on Figure 12, where the relaxation time τ is plotted against the number of posts in the system. A sharp rise at $N_{p,x} = 25$ is observed, due to particles no longer being able to move between lanes. To measure τ, the time series of the x velocity, $\langle v_x \rangle$, for each lane was taken and exponential fit of the form $|1 - \exp(-t/\tau)|$ was realized and then averaged over all samples. This was done since $\langle v_x \rangle$ in each lane starts at 0, due to random initial conditions, and move to ± 1, corresponding to the right or left direction. Increasing β and N reduces the relaxation time τ since the system will, respectively, align faster in collisions and realize more collisions. Increasing $N_{p,x}$ also has that effect as the boundary between lanes becomes "smoother" and harder for particles to get stuck in.

The same phases were observed in a system with four times the area, while keeping the same filling fraction, as can be seen on Figure 13. This result, in conjunction with the polarization curve for a larger system overlapping with the one for a smaller system in Figure 8, suggests that the behaviors analyzed are consistent across scales.

The values of $N_{p,x}$ for each transition does not change when varying N, and two parameters were observed to define the points at which each transition happens: the velocities (along

Figure 11 – (a, b, c) Examples of the system in each of the phases found (d) schematic phase diagram of the system for varying anisotropy, with the number of obstacles in the x directions indicated by $N_{p,x}$ and the number of particles by N. The number of obstacles in the y direction is fixed at $N_{p,y} = 8$ and $L = 50\sigma$. For the snapshots $D = 0.01$, $\beta = 5.0$ and $N = 576$ with the particles orientations being indicated by the color wheel and black representing the obstacles. (a) Quasi-isotropic system moving upwards with $N_{p,x} = 14$. While there is a preference in moving along the horizontal axis, collective movement along the vertical one is still possible. (b) A coupled lane system with $N_{p,x} = 22$, while the polarization is restricted to the x axis, different lanes can still take different directions. Since particles can still move vertically, some lanes will have different densities than others. (c) Uncoupled lanes with $N_{p,x} = 26$, particles can no longer move between lanes and some of those get “stuck” in the ridges formed by posts. Neighboring lanes no longer influence each other.

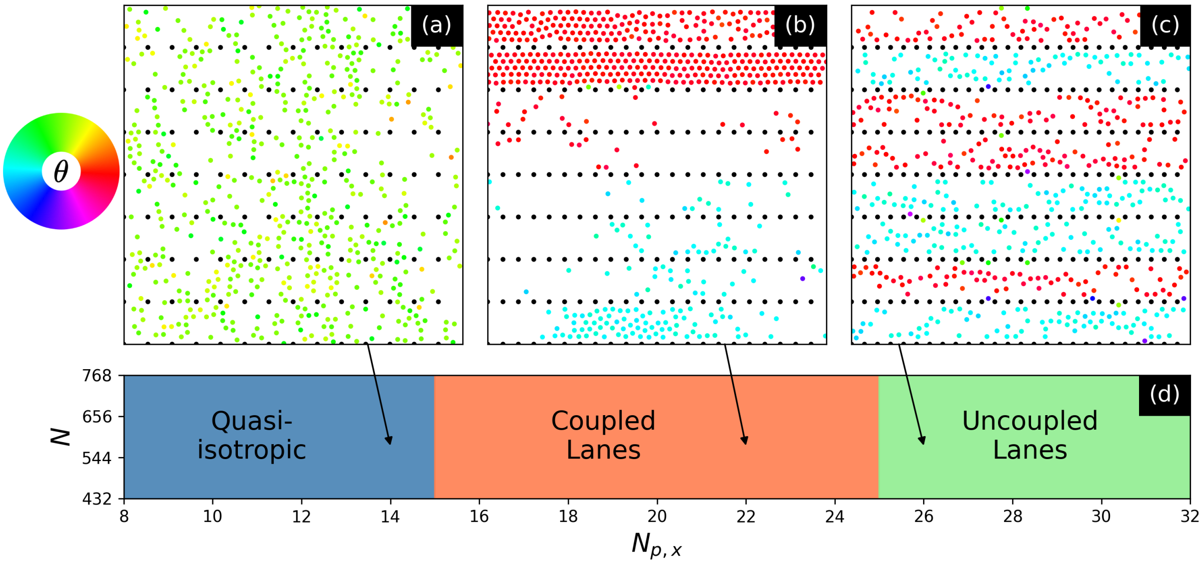

Source: (CANAVELLO et al., 2025)

both axes) and the interface probability between lanes, that is, the chance that two lanes have opposing directions. The first transition, between quasi-isotropic and coupled lanes phases was characterized as when $\langle v_y^2 \rangle$ goes to 0, indicating that the system no longer has vertical movement in the bulk, while the coupled to uncoupled lane transition was defined as the point at which the interface probability reaches 0.5, which happens when each lane is effectively its own subsystem that picks a direction at random. In Figure 14(a) the velocities are plotted against $N_{p,x}$ going from the isotropic case, at $N_{p,x} = 8$ up to $N_{p,x} = 32$. As expected, both values start at 0.5, since there is an equal probability of the system moving in any of the four symmetry directions, and as the anisotropy increases, $\langle v_y^2 \rangle$ goes to 0 since the bulk will no longer move vertically. The interface probability, in Figure 14(b) goes from 0, which indicates the system moving as a whole in a single direction to 0.5, meaning that each lane assumes a direction randomly and independently from other lanes.

Figure 12 – Transient time τ required for lanes to reach a steady velocity versus the number of posts in the x direction at $D = 0.01$ and (a) $\beta = 5.0$ and (b) $N = 528$. At $N_{p,x} = 25$ particles can no longer move between lanes and become stuck in the ridges formed by the posts, as the spacing becomes equal to the particle size. This induces the formation of clogs or jams inside lanes, which are broken apart with noise. By increasing $N_{p,x} = 25$ further, it becomes harder for particles to get stuck as the ridges become smaller, reducing τ. When β is increased, particles are quicker to align themselves and reach a steady flow, which is why τ decreases. Similarly, increasing N results in more collisions which also helps the system reach a steady state faster. Error bars indicate the standard deviations obtained from 50 realizations of random noise.

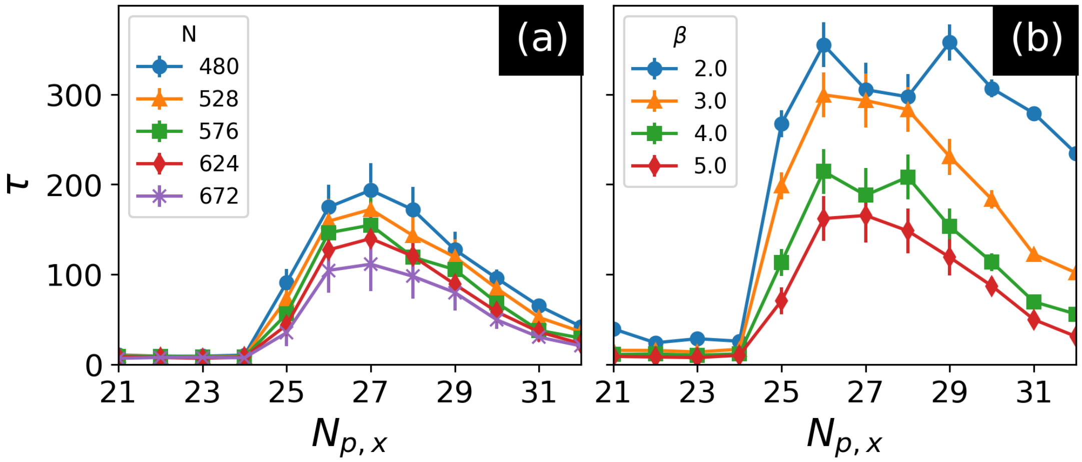

Source: (CANAVELLO et al., 2025)

Figure 13 – Equivalent phases to Figure 11 for a system with $L = 100\sigma$ and $N = 4 \times 576 = 2304$, preserving the same filling fraction. (a) Quasi-isotropic system, (b) Coupled lane state (c) Uncoupled lanes.

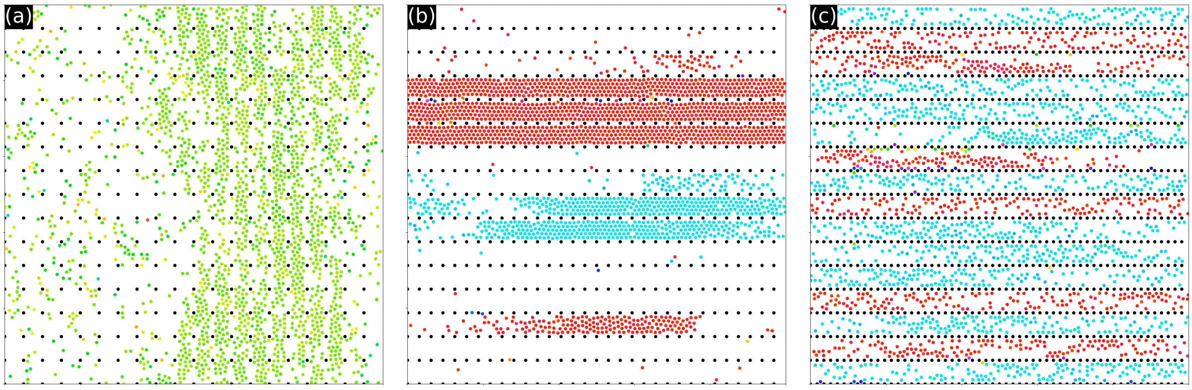

Source: (CANAVELLO et al., 2025)

Figure 14 – (a) Mean square velocities $\langle v_x^2 \rangle$ and $\langle v_y^2 \rangle$ versus $N_{p,x}$ for a system with $D = 0.01$, $\beta = 5.0$, $L = 50\sigma$ and $N = 576$. The squared velocities guarantee that particles moving along both the positive direction and negative directions are counted equally. (b) Interface probability, which is the chance that neighboring lanes have opposing directions. At $N_{p,x} = 25$ the spacing between obstacles is exactly σ, indicated by a sharp increase in the probability. The error bands are standard deviations obtained from 100 realizations of random noise.

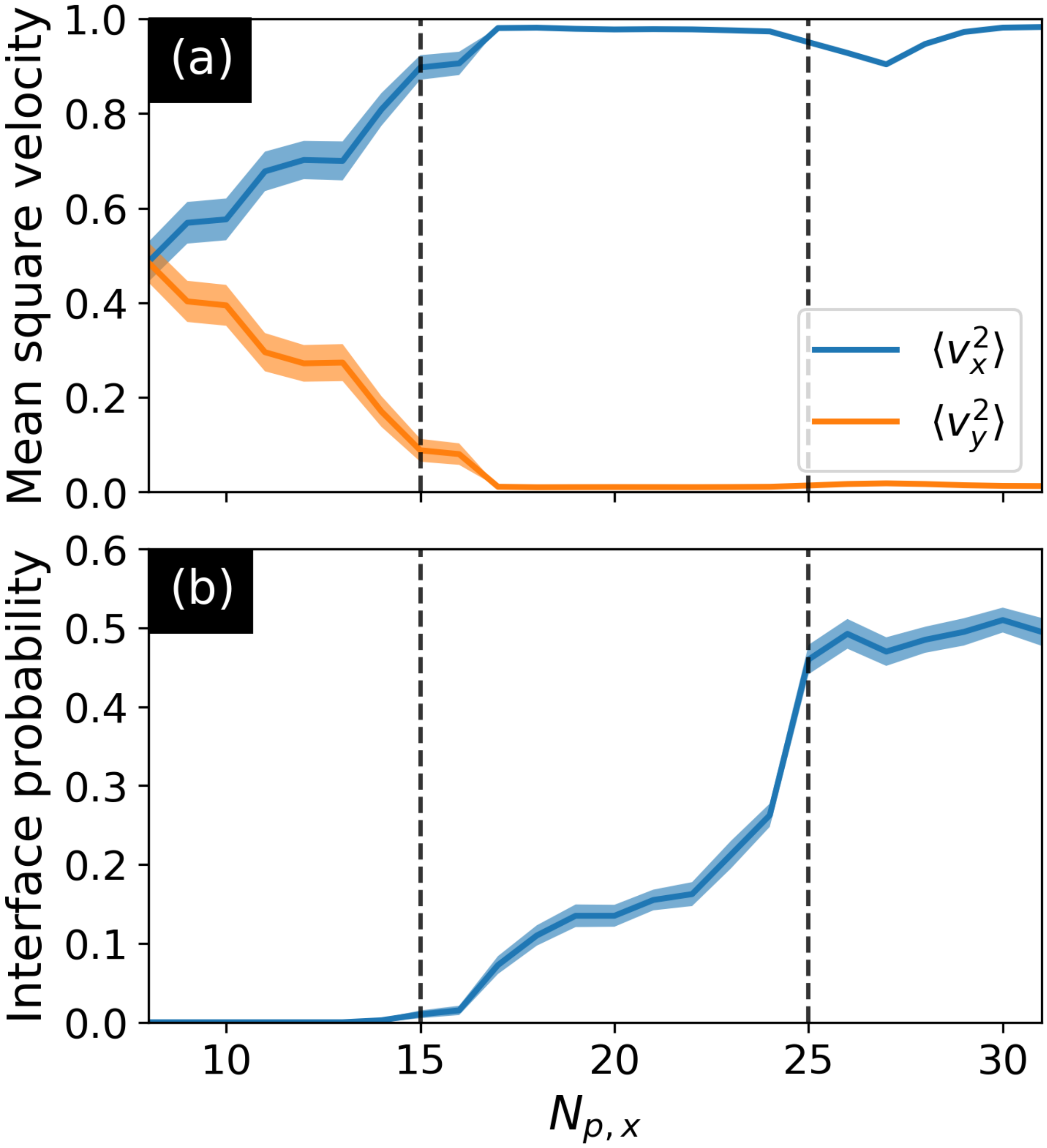

Source: (CANAVELLO et al., 2025)

4.4 TAKEAWAYS

This chapter investigated the dynamics of an interacting active matter system, focusing on the emergence of polarized states in the absence of a confining potential. By varying the alignment torque parameter β, a critical value β_c at which polarization happens is identified. This threshold is derived analytically and confirmed through numerical simulations of the Langevin equations of motion.

When a square array of obstacles is introduced, the flocking conditions remain unchanged, but the system becomes locked to the symmetry directions of the array. Adding a small anisotropy to the distribution of obstacles reveals that having more posts in one direction (the x one in this case) initially leads to a quasi-isotropic phase, where the system retains collective motion with a preference for the x-direction, while still allowing for bulk movement in the perpendicular y-direction.

As anisotropy increases, the system transitions to coupled lane phases, where collective motion is restricted to lanes that can still interact and vary in density. At high enough anisotropy, the system enters the uncoupled lanes phase, where the lanes become isolated and each polarizes independently of the others. These findings highlight how changes in obstacles configurations can lead to distinct phases in active matter systems, offering insights into how collective behavior changes when disorder is included.

5 DYNAMICS OF ACTIVE MATTER IN A CONFINING POTENTIAL

This chapter concerns a system of interacting active matter in a confining harmonic potential, and how the addition of a aligning torque modifies the dynamics compared to both the confined single particle case and the free interacting system case. Several distinct phases are observed, with notable ones being: a close-packed vortex phase in which particles collectively rotate around the potential's minimum; a vortex phase with concentric bands around an empty center; and an orbiting polar state in which each particle has the same orientation, similar to a ferromagnetic system.

The results presented this chapter were published in the article (CANAVELLO et al., 2024).

5.1 HARMONIC CONFINEMENT

As demonstrated in Section 3.2, the introduction of a torque β modifies the dynamics of a trapped particle, allowing a new trajectory in which the particle orbits the potential. Additionally, Chapter 4 studied the behavior of an interacting system, with emphasis on collective flocking dynamics. This raises the question of how both the inclusion of both elements would influence the system's dynamics.

By adding a harmonic potential of the form $V(r) = \frac{1}{2}\kappa r^2$ to the system (e.g. by putting all particles on the same parabolic dish), two limiting cases can be considered initially, those being one with $D \to \infty$ in which case the system behaves as composed of classic Brownian particles, following a Boltzmann distribution peaked around the minimum of the potential. This is expected since a high enough noise will destroy the activity in the system (TAKATORI et al., 2016; MALAKAR et al., 2020). This will be denoted as the paramagnetic (PM) or unpolarized phase. The second case is $\beta = 0$, meaning particles have no alignment torque, in which cases each particle simply tries to climb the potential independently, only to be stopped when the steepness of the potential and the repulsion from neighboring particles is equal to their propulsion. That is, each particle is individually in the climbing state and all particles point outwards. Since the alignment of each particle is parallel to their radial position, this is called the radially polarized (RP) phase.

Representative snapshots for the dynamic phases found can be seen in Figure 15 for systems without thermal noise i.e. $D = 0v_0/\sigma$. In panel (a), an example of the RP phase is shown for $\beta = 0.5\mu/\sigma$, with particles having no net movement the potential minimum remaining unoccupied, since each particle climbs according to their orientation and have no collective dynamics. By increasing β, the alignment during collisions will be stronger, so new phases can emerge. The (b) panel shows a vortex state for $\beta = 1.85\mu/\sigma$, with the particles outside the orange line (denoting the shear band boundary) rotating with the same angular speed. Inside the orange line, the particles try to climb into the vortex, but do not rotate together with it, thus giving this phase the name shear-banded vortex, or SBV[1].

When increasing β further, the shear band boundary shrinks (as it will be proved later, it scales with β^{-1}). Once it's small enough that there is no empty area available for particles to be in, all particles in the system will rotate together. However, the ones inside the shear band boundary will not have an orientation that matches with the particles outside. This indicates that while the angular velocity of particles above the β^{-1} boundary matches the orientation change, $\dot{\theta}$, this does not hold for the particles inside. This state is seen on panel (c) for $\beta = 5.0$ and is called the uniform vortex (UV) phase.

It is also possible for all particles to assume the same orientation, in which case $\theta_i = \theta$ for all i, denoted the ferromagnetic phase (FM) due to a resemblance of the system with a polarized magnet. This makes the system into a single big cluster possessing one orientation, and the system behaves in a way analogous to the one-particle system. In this case, the center of mass performs a circular trajectory with finite radius. An example of this system is seen on panel (d) of Figure 15 for $\beta = 5.0$, with all particles having the same color (indicating their equal orientations) and arrows of same direction and magnitude (indicating their equal velocities). The red circle indicates the center of mass trajectory. Although the values of the system parameters are the same for panels (c) and (d), the final state is different due to the random initial condition of the particles that can make the system go into either the vortex or ferromagnetic states after relaxing.

If the filling fraction of the system is small, a separation of particles into multiple clusters can happen. It works as a combination of both the ferromagnetic and vortex states, in which particles group together into polarized clusters, each acting as a single particle orbiting the potential, similar to a vortex state. In Figure 15(e) this phase is shown for a state with 4 clusters for a system with $N = 93$ and $\beta = 5.0$. In the absence of thermal noise, the cluster composition and size remain static in time. By changing the initial conditions of the system,

---

[1] As with the previous chapter, the units for β and D, respectively μ/σ and v_0/σ, will be omitted for clarity from here on.

the same set of configurations may lead to different cluster arrangements.

Figure 15 – Snapshots of particle configurations for the different phases found in a confined system. (a) Radially polarized (RP); (b) Shear-banded vortex (SBV); (c) Uniform vortex (UV); (d) Ferromagnetic (FM) orbiting cluster; (e) Multi-cluster state with four clusters. In all cases, $D = 0$ and $\sigma = 0.1$. For (a)-(d), $N = 350$ and $\beta = 0.5, 1.85, 5.0$ and 5.0 respectively. For (e), $N = 93$ and $\beta = 5.0$. Note that panels (c) and (d) share identical system parameters, with the only difference being the initial conditions, illustrating the coexistence of the UV and FM phases. The colors indicate the internal orientation θ of the particles, while the velocities are indicated by arrows. The center of mass trajectory is marked with a red line and blue dashed line shows the critical isocline. For the vortex states in (b) and (c), the orange dashed line represents the predicted boundary between bands (see Section 5.2).

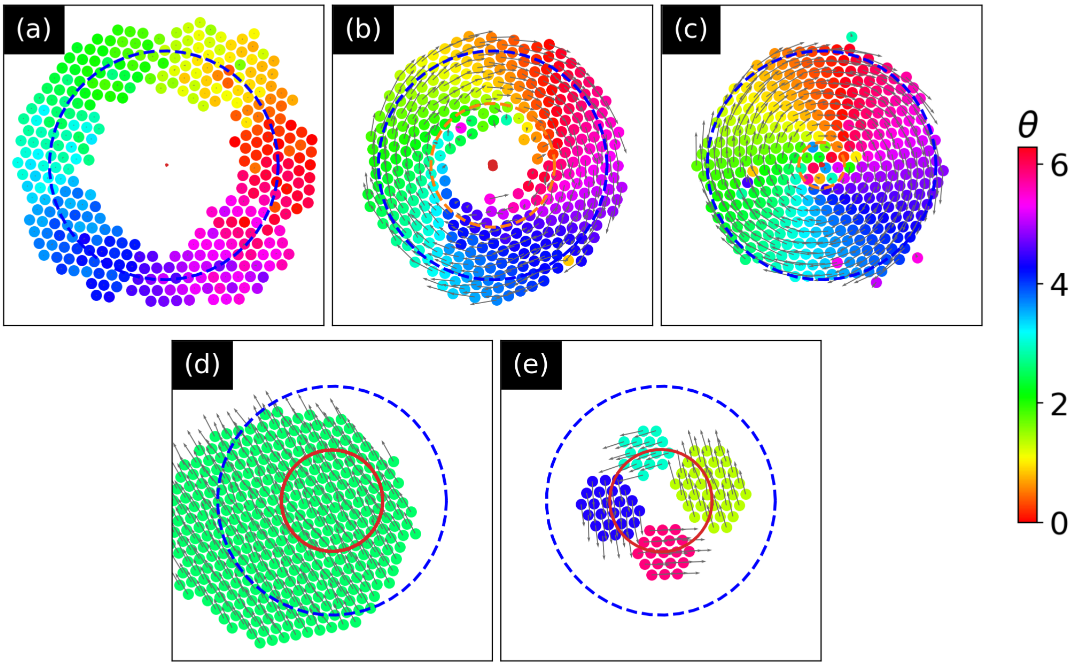

Source: (CANAVELLO et al., 2024) (adapted)

5.1.1 Observables

Since the potential is radially symmetric, it is useful to introduce some new quantities to help with calculations. Define φ_i as the radial angle of the i-th particle in the potential, such that its position will be given by $\mathbf{r}_i = (r_i \cos\varphi_i, r_i \sin\varphi_i)$. Then a tilt angle can be defined as the difference between the internal orientation and radial angle: $\chi_i = \theta_i - \varphi_i$.

Since the area which particles can exist in is boundless, the filling fraction f is now defined as the ratio of area occupied by the particles over the area the enclosed by the critical isocline,

$$f = N\frac{A_{\text{part}}}{A_{\text{CI}}} = \frac{N2^{\frac{1}{3}}\sigma^2}{4R_{\text{CI}}},$$

where $R_{\mathrm{CI}} = v_0/(\mu\kappa)$ is the critical isocline radius, which is defined in the same way as in Section 3.2. Specifically, it represents the radius at which the confining force equals the self-propulsion force of a single particle. Consequently, isolated particles in the noiseless regime cannot cross this radius from the inside out. However, interparticle interactions can push particles to a larger radius. It is important to note that, under this definition, the filling fraction can be greater 1. This indicates that particles will necessarily be found outside the critical isocline boundary.

Quantities for the bulk can also be defined, and the ones that will be used are the total, radial and azimuthal polarizations for the system

$$\mathbf{P} = \frac{1}{N}\sum_{i}^{N}\mathbf{n}_i, \tag{5.1a}$$

$$P_r = \frac{1}{N}\sum_{i}^{N}\mathbf{n}_i \cdot \hat{\mathbf{r}}_i, \tag{5.1b}$$

$$P_\phi = \frac{1}{N}\sum_{i}^{N}|\mathbf{n}_i \cdot \hat{\phi}_i|, \tag{5.1c}$$

in which $\hat{\mathbf{r}}_i = \mathbf{r}_i/|\mathbf{r}_i|$ and $\hat{\phi}_i = \hat{\mathbf{z}}_i \times \hat{\mathbf{r}}_i$ are the radial and azimuthal unit vectors. This way, $\mathbf{P}$ will measure how aligned particles are with each other, having magnitude 0 for a completely misaligned system and 1 for one where every particle points in the same direction and P_r will measure how aligned the particles are to the radial direction, while P_ϕ quantifies azimuthal alignment. It is important to note that since the directions of rotation are equivalent, the absolute value of P_ϕ must be considered to account for this symmetry. Specifically, clockwise motion will correspond to a negative $\mathbf{n}_i \cdot \hat{\phi}_i$ while counter-clockwise motion corresponds to a positive value. By taking the absolute value both directions will count equally instead of canceling each other. These quantities are used, in order, to classify a phase as FM, RP and either of the vortex states.

The hexatic order parameter, defined as

$$\psi_6^G = \left|\frac{1}{N}\sum_{i=1}^{N}\left[\frac{1}{\mathcal{N}_i}\sum_{j=1}^{\mathcal{N}_i} e^{i6\theta_{ij}}\right]\right|, \tag{5.2}$$

with $\mathcal{N}_i$ being the number of nearest neighbors for particle i and θ_{ij} being the angle that particle i forms with its neighbor j, will measure how crystalline the system is, being 1 when every particle has 6 neighbors, i.e. the system forms a triangular lattice. Neighbors are defined as particles located within a distance of 1.5σ of each other, and nearest-neighbor searches were performed using $k-d$ trees (CHEN et al., 2019). Because the analysis depends solely on the relative angles between neighboring particles, no special classification of boundary regions is required, this can be understood since a particle with only two or three neighbors can still be identified as part of a crystalline structure, provided that the neighbors are arranged at 60° angles.

5.2 ANALYTICAL FRAMEWORK AND DETERMINISTIC SOLUTIONS

Analytical calculations based on rigid body theory can be employed to predict the system's behavior in its close-packed states, specifically the ferromagnetic (FM) and uniform vortex (UV) phases. The mathematical details for this analysis are provided in Appendix A for reference.

To begin, consider the dimensionless equations of motion for a system without thermal noise (i.e., when $D = 0$). This is achieved by setting the units of length, time, and energy as $v_0/(\mu\kappa)$, $1/(\mu\kappa)$, and $v_0^2/(\mu^2\kappa)$, respectively.

$$\dot{\mathbf{r}}_i + \mathbf{r}_i - \mathbf{F}_i^{\text{int}} = \hat{\mathbf{n}}_i, \tag{5.3a}$$

$$\dot{\theta}_i = \beta(\hat{\mathbf{n}}_i \times \dot{\mathbf{r}}_i) \cdot \hat{\mathbf{z}}, \tag{5.3b}$$

in which $\mathbf{F}_i^{\text{int}}$ is the total force acting on the ith particle due to interparticle interactions[2]. By summing Eq. (5.3a) across all particles, the pairwise interactions will cancel each other and an equation for the centroid, defined as $\mathbf{R} = \sum_{i=1}^{N} \mathbf{r}_i/N$, is found

$$\dot{\mathbf{R}} + \mathbf{R} = \mathbf{P} \tag{5.4}$$

If $\hat{\mathbf{n}}_i = \mathbf{P}$ for all i, the cluster moves as a single particle. In this case, the system can be considered a single particle in confinement, a scenario with a well-known solution, which was derived in Section 3.2. For $\beta > 1$, the system exhibits orbital motion with radius R, angular velocity Ω and orientation angle θ_c.

$$R = \beta^{-1/2}, \tag{5.5a}$$

$$\Omega = \pm\sqrt{\beta - 1}, \tag{5.5b}$$

$$\theta_c(t) = \pm\sqrt{\beta - 1}t + \arccos(\beta^{-1/2}) + \theta_c(0), \tag{5.5c}$$

---

[2] Note that in the absence of noise, the alignment torque can be expressed as either $\hat{\mathbf{n}}_i \times \dot{\mathbf{r}}_i$ or $\hat{\mathbf{n}}_i \times \mathbf{F}_i^{\text{int}}$, as these vectors will only differ by a vector proportional to $\hat{\mathbf{n}}_i$.

note that $\dot{\theta}_c = \Omega$, which is expected.

If all particles are rotating around the origin, then $\mathbf{R} = \mathbf{P} = 0$. A helpful quantity can be obtained by performing the cross product between $\mathbf{r}$ and Equation (5.3a). Since all particles are performing a circular motion, then $\dot{\mathbf{r}}_i$ will be perpendicular to $\mathbf{r}_i$ and have magnitude $\mathbf{r}_i\dot{\varphi}_i$. Once again summing over all particles, the following is found

$$\sum_i \mathbf{r}_i^2 \dot{\varphi}_i = \sum_i \mathbf{r}_i \sin\chi_i, \tag{5.6}$$

the tilt angle naturally appears when doing the cross product between the radial position and the orientation.

In the model considered so far, the condition $\dot{\theta}_i = \dot{\varphi}_i$, equivalent to $\dot{\chi}_i = 0$, was implied, i.e. a rigid body condition. As will be proven later, this is only satisfied for $r_i > \beta^{-1}$. This requirement can be relaxed while still assuming that particles have the same angular velocity ($\dot{\varphi}_i = \omega$ for all particles) and are in a constant radius ($\dot{r}_i = 0$ for all particles), making this, in fact, a quasi-rigid body model. In this case, Equation (5.3b) can be written as

$$\dot{\chi}_i = (\beta r_i \cos\chi_i - 1)\omega, \tag{5.7}$$

note that $\cos\chi_i$ appears instead of $\sin\chi_i$ since $\dot{\mathbf{r}}_i \perp \mathbf{r}_i$ as mentioned above. This equation has a known solution, with two distinct regimes depending on whether $r_i > 1/\beta$ or not (see Equation (A.22) in Appendix A).

For $r_i > 1/\beta$, the solution is

$$\chi_i = 2\arctan\left[\left(\frac{C_+ + C_- e^{-t/\tau_\omega}}{C_+ - C_- e^{-t/\tau_\omega}}\right)\sqrt{\frac{\beta r_i - 1}{\beta r_i + 1}}\right], \tag{5.8}$$

where $C_\pm = \tan\left(\chi_i(0)/2\right) \pm \sqrt{\left(\beta r_i - 1\right)/\left(\beta r_i + 1\right)}$, $\chi_i(0)$ is the initial value of χ_i at $t = 0$ and $\tau_\omega = 1/\omega\sqrt{\beta^2 r_i^2 - 1}$. This regime is monotonic on time, and for $t \gg \tau_\omega$, the equation takes a value of $\chi_i = 2\arctan\sqrt{(\beta r_i - 1)/(\beta r_i + 1)}$. It can be verified that $\cos\chi_i = 1/\beta r_i$, which is the same result found when taking $\dot{\chi}_i = 0$ in Equation (5.7)[3].

Meanwhile for $r_i < 1/\beta$, the solution is

$$\chi_i = -2\arctan\left[\sqrt{\frac{1 - \beta r_i}{1 + \beta r_i}}\tan\left(\nu t/2 - C_0\right)\right], \tag{5.9}$$

where $\nu = \sqrt{1 - \beta^2 r_i^2}\omega$ is the angular frequency of χ_i and

$$C_0 = \arctan\left[\sqrt{\left(1 - \beta r_i\right)/\left(1 + \beta r_i\right)}\tan\left(\chi_i(0)/2\right)\right].$$

---

[3] Due to the trigonometric identity $\cos(2\arctan(x)) = (1 - x^2)/(1 + x^2)$

Contrasting with the previous regime, this solution is oscillatory.

To find the projections of χ_i on the radial and azimuthal directions, and thus the components of $\mathbf{n}_i$, it is enough to find $\cos\chi_i$ (corresponding to the radial projection) and $\sin\chi_i$ (corresponding to the azimuthal projection). For the $r_i > 1/\beta$ regime, this is taken as the asymptotic values at large t, while for $r_i < 1/\beta$ a time average over one period, $T = 2\pi/\nu$, is taken. This gives

$$\langle \sin\chi_i \rangle = \begin{cases} 0 & \text{if } r_i < 1/\beta, \\ \sqrt{1 - \frac{1}{\beta^2 r_i^2}} & \text{if } r_i > 1/\beta, \end{cases} \tag{5.10}$$

$$\langle \cos\chi_i \rangle = \begin{cases} \frac{1-\sqrt{1-\beta^2 r_i^2}}{\beta r_i} & \text{if } r_i < 1/\beta, \\ \frac{1}{\beta r_i} & \text{if } r_i > 1/\beta. \end{cases} \tag{5.11}$$

With this in mind, the average angular speed of the entire system can be found by looking at Equation (5.6) and the values of $\sin\chi_i$. By taking $\dot{\varphi}_i = \omega$ once more

$$\langle \omega \rangle = \frac{\sum_i' \sqrt{r_i^2 - \beta^{-2}}}{\sum_i r_i^2}, \tag{5.12}$$

where $\sum_i'$ indicates the sum is only performed for particles with $r_i > 1/\beta$. Performing a similar operation to Equation (5.7) results in

$$\langle \dot{\theta}_i \rangle = \begin{cases} \langle \omega \rangle \left(1 - \sqrt{1 - \beta^2 r_i^2}\right) & \text{if } r_i < 1/\beta, \\ \langle \omega \rangle & \text{if } r_i > 1/\beta. \end{cases} \tag{5.13}$$

A perceptive reader will notice that since $\dot{\chi}_i \neq 0$ for $r_i < 1/\beta$, then Equation (5.3a) says that $\dot{\mathbf{r}}_i \neq 0$, implying a time dependence on $\dot{r}_i$ or $\dot{\varphi}_i$. In this model, an approximation of constant angular velocities and small radial distance variations, represented by δr_i are assumed. In the simulations, this manifests as a jelly-like jiggling of the system, and the model is expected to hold as long as $\delta r_i \ll r_i$.

5.3 NUMERICAL RESULTS

By numerically integrating the equations of motion in Equations (2.1) and measuring the polarizations, the ranges in which the phases, as shown in Fig 15, exist can be determined. A uniform random distribution was used to select the initial position and orientation of the particles. This is important since some phases coexist, and the variability in initial conditions can lead the same system to evolve into different phases. This way, the radially polarized (RP) phase is characterized by a large P_r, since all orientations are aligned with the radial position. The vortex states have two different behaviors: at $\beta \gtrsim 1$, P_r is large but P_ϕ is non-zero, and this azimuthal alignment is enough for the system to rotate while still pointing mostly outwards; while at $\beta \gg 1$, P_ϕ dominates and the particles rotate with internal orientation perpendicular to their radial position. For the uniform vortex (UV) phase, the hexatic parameter ψ_6^G is also large since the particles are close packed, in contrast of the shear-banded vortex (SBV) hollow center. When the system is in the ferromagnetic (FM) state, the $|\mathbf{P}|$ dominates since all particles point in the same direction. Since the system is close packed, the ψ_6^G parameter is also high. This is the phase that dominates for high β and is the most resilient to noise, provided a high enough β. When $\mathbf{P}, P_r$ and P_ϕ are all close to zero, the system lacks any kind of order and is in the paramagnetic (PM), or unpolarized, state. This phase dominates at high D and low β.

Figure 16 showcases the four observables in the $D - \beta$ space, with the colors being an average of each observable over 50 realizations of random noise and 100 units of time. The solid lines indicate the stability boundaries for each phase, obtained by initializing the system in a phase, then gradually changing β and D until the polar order observable for that phase falls below a threshold equal to 0.5, which is then considered to be a different phase.

The criteria for transition were validated by analyzing the time evolution of the system near the predicted boundaries. The transition from the RP to vortex states presents a unique case, as the system is particularly sensitive to changes in this regime. To classify the system as being in the vortex state, a threshold of $P_\phi > 0.1$ was adopted, since any azimuthal polarization that appears signals the onset of rotation. This criterion is marked by the dashed blue line. Additionally, the SBV phase exhibits a higher P_r than the UV phase, as the particles at the center of the system do not rotate with the bulk. Based on this distinction, a value of $P_r = 0.5$ was chosen as a rough estimate to represent the transition between these two phases.

Figure 16 – Heatmaps of the four observables measured in the $D-\beta$ plane at fixed $N = 93$ and $\sigma = 0.2\,(f \simeq 1.17)$. Double brackets indicate averages over time and random noise realizations. (a) Radial polarization $\langle\langle P_r \rangle\rangle$; (b) Azimuthal polarization $\langle\langle P_\phi \rangle\rangle$; (c) Modulus of the total polarization $\langle\langle |\mathbf{P}| \rangle\rangle$; and (d) hexatic order parameter $\langle\langle \psi_6^G \rangle\rangle$. The red, blue and white lines indicate, in order, the boundaries in which the ferromagnetic (FM), uniform vortex (UV) and radially polarized (RP) phases become unstable. The dashed blue line separates the shear-banded vortex (SBV) and the RP phases.

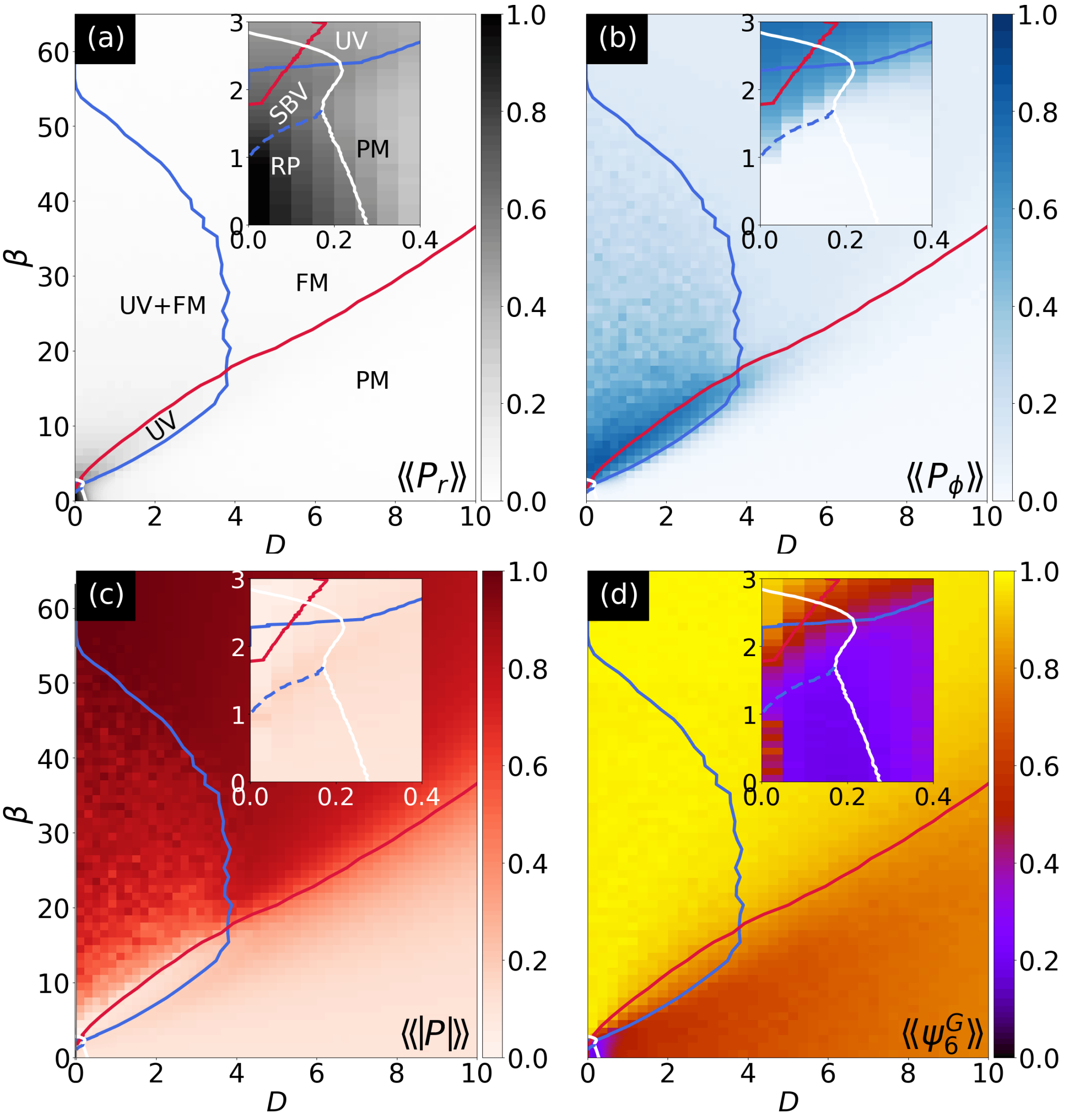

Source: (CANAVELLO et al., 2024)

5.4 PHASES

5.4.1 Radially polarized phase

The radially polarized (RP) phase is a simple static phase, in which, similar to the climbing phase for one confined particle and (DAMASCENA; CABRAL; SILVA, 2022), particles simply accumulate on the edges of the potential and stay there. At $D \ll 1$ and $\beta \lesssim 1$, the particles will be closely packed and the system shows crystalline order, which is indicated by a high $\langle\langle\psi_6^G\rangle\rangle$. When the noise D is increased, order decays and the system exhibits a more fluid behavior, but still keeps radial order. By further increasing D, and keeping β low, all order is lost and the system enters the paramagnetic phase. However, by increasing β at a fixed and low D, the system will transition into either the vortex or ferromagnetic phases, as will be described below.

5.4.2 Coexistence properties of the ferromagnetic and uniform vortex phases

Both the ferromagnetic (FM) and uniform vortex (UV) states are characterized by the particles being closely packed and having quasi-crystalline order, which (at low noise) indicate that both of these phases can be well described by the model presented in Section 5.2.

In the FM phase, all particles possess the same orientation θ and the system behaves like a single particle revolving around the potential center with constant radius R and angular speed Ω. In Figure 17(a), the analytical calculations in Equation (5.5) are compared against the numerical simulation results for a system with $N = 93$ and $\sigma = 0.2$ for several noise values. Both results coincide even at higher noise levels, indicating that the FM is resilient to thermal fluctuations. This can be inferred from Figure 16, in which the FM phase boundary (in red) is seen to grow with β, indicating a high noise tolerance as long as β is large enough.

For the UV phase, all particles have the same angular speed $\dot{\varphi}_i = \omega$ and the system rotates around its own axis, which is in the potential minimum. Once again comparing the numerical simulations with the analytical results obtained from Equation (5.12) in Figure 17(b), the results align very well in the noiseless regime $D = 0$, but worsen significantly when the noise level is increased. According to the blue line in Figure 16, at $D = 0.5$ the system should be well in the stability range for the UV phase, however the mean angular velocity of the system falls far below the expect value from the rigid-body model, suggesting that the UV phase is far more sensitive to noise than the FM phase.

In Figure 16 it is easy to see that there is a large coexistence range between the UV and FM phases, denoted by the area enclosed by the red and blue lines. Having the same parameters, the system will fall into one of these phases depending solely on its initial configuration, with the FM being more likely for higher β (and conversely UV being more probable for lower β). This suggests that by varying β or D, the system can transition between these phases, and

Figure 17 – Comparison between the analytical predictions and numerical simulation results when varying the self-alignment torque β at different noise levels D for a system with $N = 93$ and $\sigma = 0.2$. The dashed lines indicate analytical results. (a) Angular velocity of the ferromagnetic phase cluster Ω and (inset) orbit radius R. (b) Angular velocity of the uniform vortex phase ω. It should be remembered that in (a) phase the cluster revolves around the potential center with a finite radius while in (b) the cluster rotates around its own axis.

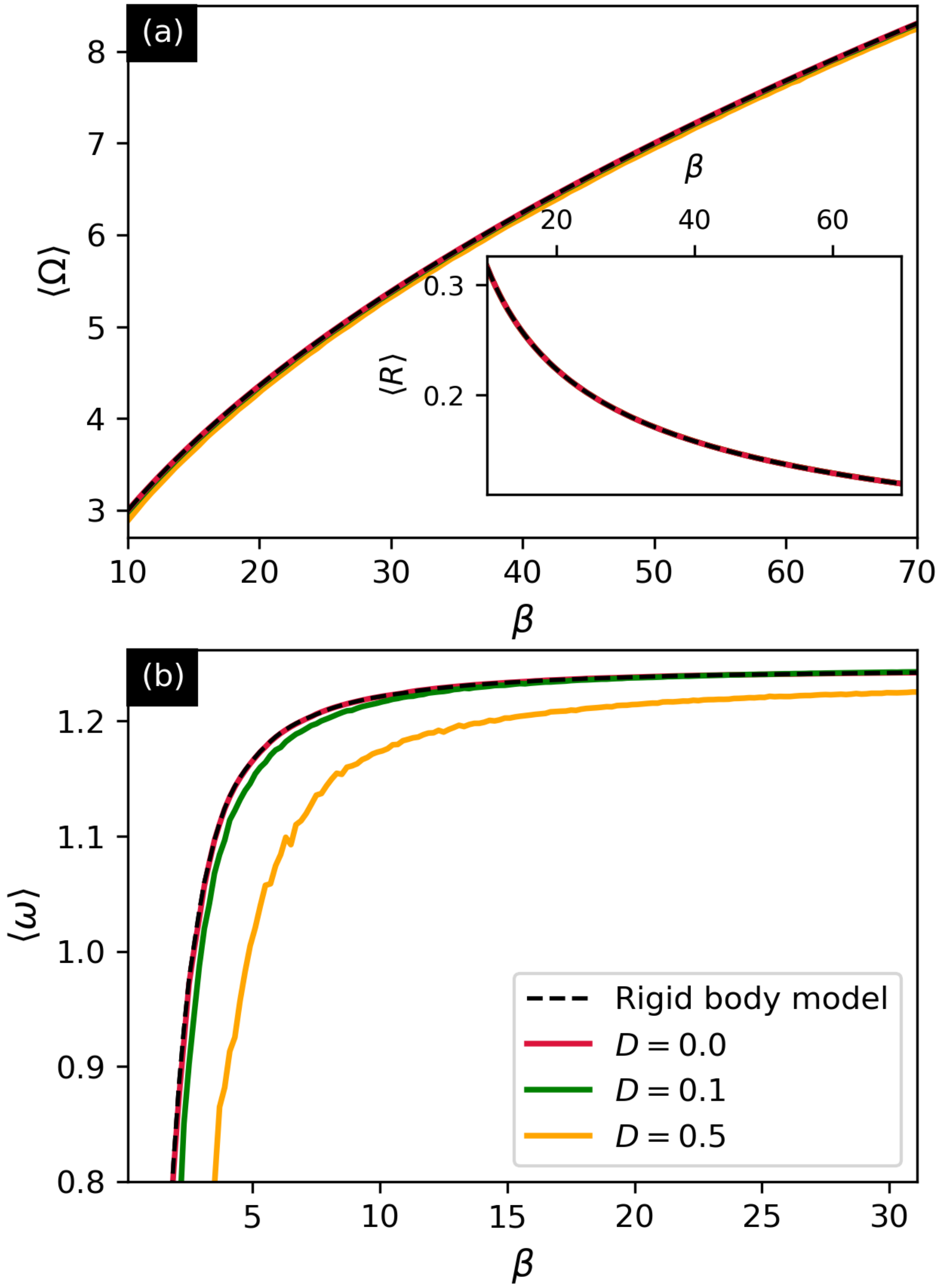

Source: (CANAVELLO et al., 2024)

hysteresis is observed when doing so.

Figure 18 – Averages over time and random noise realizations for (top) $\langle\langle \mathbf{P} \rangle\rangle$ and (bottom) $\langle\langle P_r \rangle\rangle$ and $\langle\langle P_\phi \rangle\rangle$ at (a) Fixed $\beta = 25$ and sweeping D from 0 to 10 (solid line) and back (dashed). (b) Fixed $D = 2.5$ and sweeping β from 0 to 60 (solid) and back (dashed). Shadows indicate standard deviations from the mean, and simulations were realized for a system with $N = 93$ and $\sigma = 0.2$. Insets indicate representative states of the system in each place following the same color scheme as Figure 15.

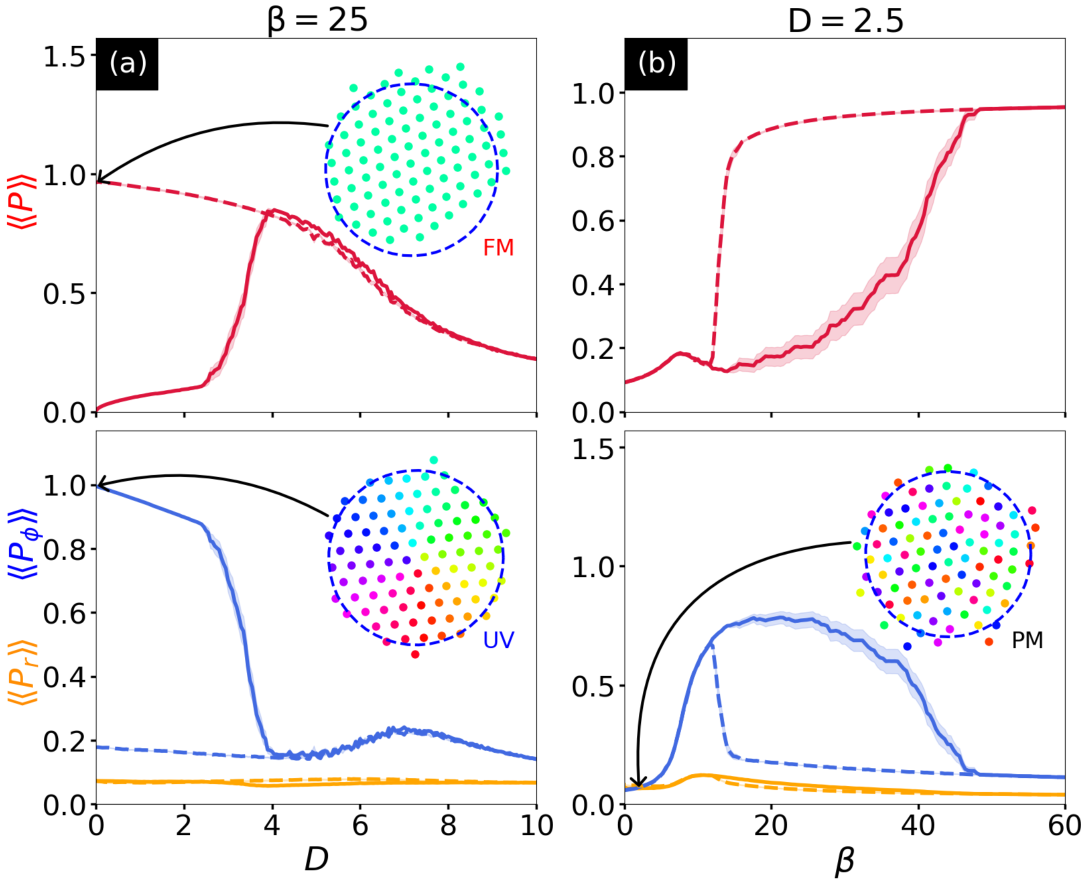

Source: (CANAVELLO et al., 2024)

This hysteretic behavior can be confirmed in Figure 18. For the (a) panels, on the left side, the system is initialized in a UV state at $\beta = 25$, which is relatively high. This state is characterized by high P_ϕ, and by increasing the noise D, the system transitions to the FM phase, indicated by the drop in P_ϕ and simultaneous rise in $\mathbf{P}$ and by increasing the noise even further, the FM phase smoothly decays into a disordered paramagnetic (PM) phase, in which all 3 measured observables are low. By decreasing the noise from the PM phase, the system closely follows the forward path during the PM to FM transition, but at $D \sim 4$ it starts following a different path, staying on the FM phase, and the system never returns to the vortex phase.

When doing a similar simulation at constant noise D and varying β instead, on the (b) panels, a similar hysteresis is seen. The system starts in the PM phase, which is the only state possible at $\beta = 0$ and $D = 2.5$ and when β is increased it transitions into the UV phase at $\beta \simeq 20$ and into the FM phase at $\beta \simeq 40$. When going back, the system only transitions from FM to UV at $\beta \simeq 15$, demonstrating a strong hysteretic effect in the system until it goes to the PM phase at low β.

To look at noise-inducted transitions between the coexisting distinct phases, specific fixed β and D points were chosen in the parameter space and a time series of the $\mathbf{P}$ and P_ϕ observables were calculated over a long time window ($t = 10^4 t_0$). The results for these kind of transitions are presented in Figure 19. In panel (a), for a system in the coexistence zone ($\beta = 25,\ D = 2.85$), a transition from the UV to the FM phase is observed. This transition is associated with a sharp drop in P_ϕ and a simultaneous rise in $\mathbf{P}$ around $t \simeq 2700$. Panel (b) provides a zoomed-in view of the transition. Notably, if the system is initialized in the FM phase, a transition to the UV is not observed, indicating that the system is more stable in the FM phase for given parameters. Meanwhile panel (c) shows a system within the region where only the UV phase is stable, with $\beta = 9.2$ and $D = 2.5$. Here, the system exhibits multiple switches between clockwise (negative P_ϕ) and counter-clockwise (positive P_ϕ) motion. The system stays in both states for roughly similar amounts of time, which reflects the symmetry between both directions.

It should be noted that these noise-induced transitions are facilitated by the low number of particles N. When increasing N at constant filling fraction f (achieved by decreasing the particle size σ), larger noise levels are needed for the UV to FM transition to take place, until it disappears completely and the system goes straight into the PM phase.

5.4.3 In-depth analysis of the uniform vortex phase

The previous section focused on the coexistence properties between the FM and UV phases. By now turning the focus solely on the UV phase, more characteristics, such as radial dependencies, can be studied. This phase is characterized by a constant and equal angular velocity $\dot{\varphi}_i = \omega$ for all particles, but the orientation θ_i varies considerably with the radial position r_i of the particle. To better look at this phase, it is useful to consider smaller particle sizes, $\sigma = 0.1$, which improves local statistics while keeping the filling fraction constant.

This behavior is depicted in Figure 20(a, b), which shows the time-averaged radial distributions of P_r, P_ϕ, $\dot{\theta}$, and $\dot{\varphi}$ for a system with $N = 500$, $\beta = 1.85$, and $D = 0$. It is particularly

Figure 19 – Time series for $\mathbf{P}$ and P_ϕ for a system starting on the UV phase with (a, b) $\beta = 25$ and $D = 2.85$ and (c) $\beta = 9.2$ and $D = 2.5$. (a, b) shows a system going from UV to the FM phase [(b) shows a zoomed in window of the transition] (c) system in the UV phase performing multiple switches between clockwise to counter-clockwise motion

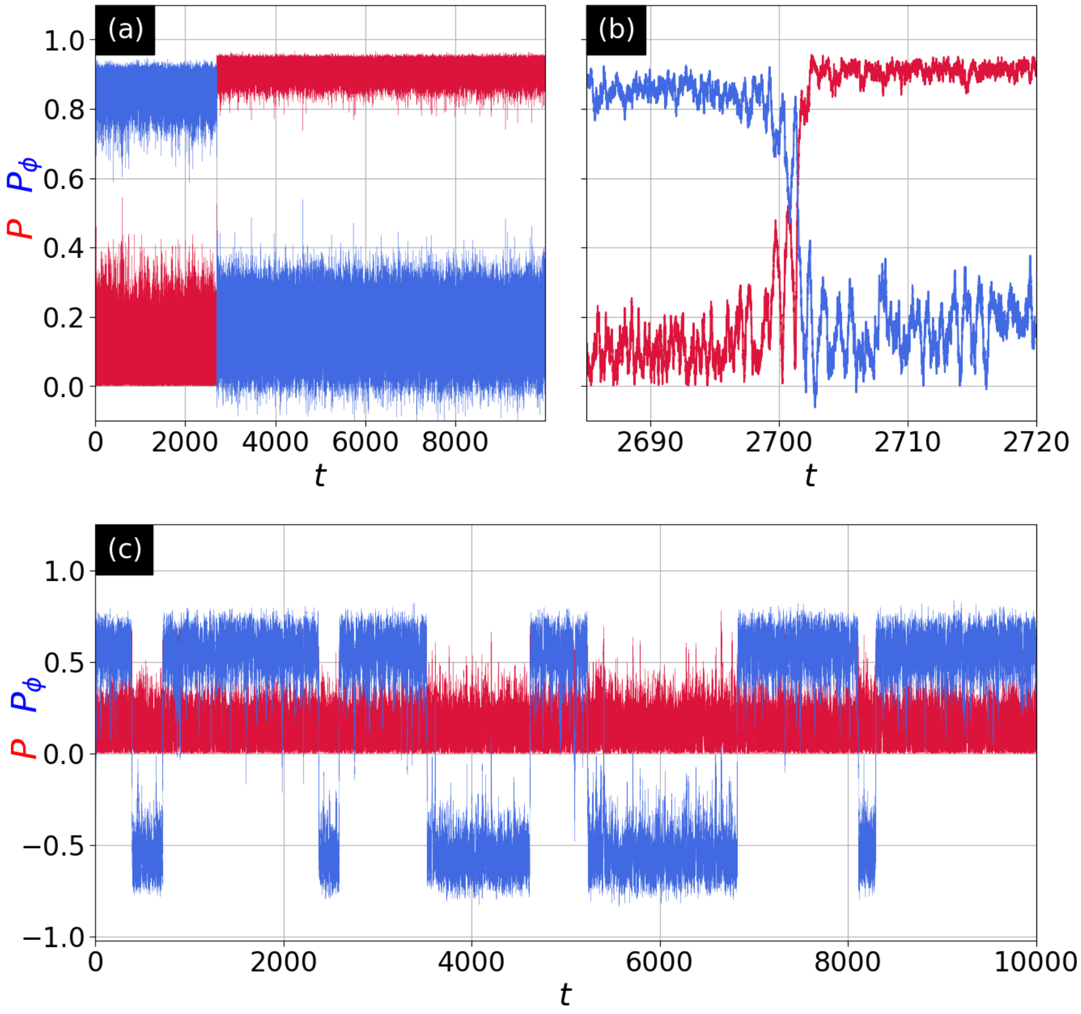

Source: (CANAVELLO et al., 2024)

notable that the angular velocity $\dot{\varphi}$ remains constant across all radial positions. This finding provides strong support for the initial assumption of uniform rotational motion, which was a necessary result for the calculations in Section 5.2.

In contrast, the observables P_r, P_ϕ and $\dot{\theta}$ display marked differences between the inner region ($r < 1/\beta$) and the outer region ($r > 1/\beta$). Despite these variations, the distributions remain in excellent agreement with the theoretical predictions. In the outer region, the system behaves in accordance with the rigid body condition, where $\dot{\varphi} = \dot{\theta}$ and the projected components conform to the analytical predictions: $P_r = \cos\chi = 1/(\beta r)$ and $P_\phi = \sin\chi = \sqrt{1 - 1/(\beta r)^2}$. Within the inner region, the rigid body approximation breaks down as $\dot{\theta}$ is no longer constant. Nevertheless, because $\dot{\varphi}$ does remain constant with respect to r, the theoretical expressions

Figure 20 – Time averages for $P_r, P_\phi, \dot{\theta}$ and $\dot{\varphi}$ for simulations (shaded areas) and analytical results (dashed lines). Simulations use $\sigma = 0.1$, $\beta = 1.85$ and $D = 0$, while having $N = 500$ for (a, b) and $N = 350$ for (c, d). The red and blue dashed lines are plots of the Equations (5.10) and (5.11), whereas the purple and green lines indicate Equations (5.12) and (5.13). In (a, b) the simulation matches the predictions remarkably well, while for lower densities in (c, d) it fails in the $r < 1/\beta$ region, which is unoccupied since the system is in the shear-banded vortex phase. The numerical results fall to 0 due to the finite size of the sample.

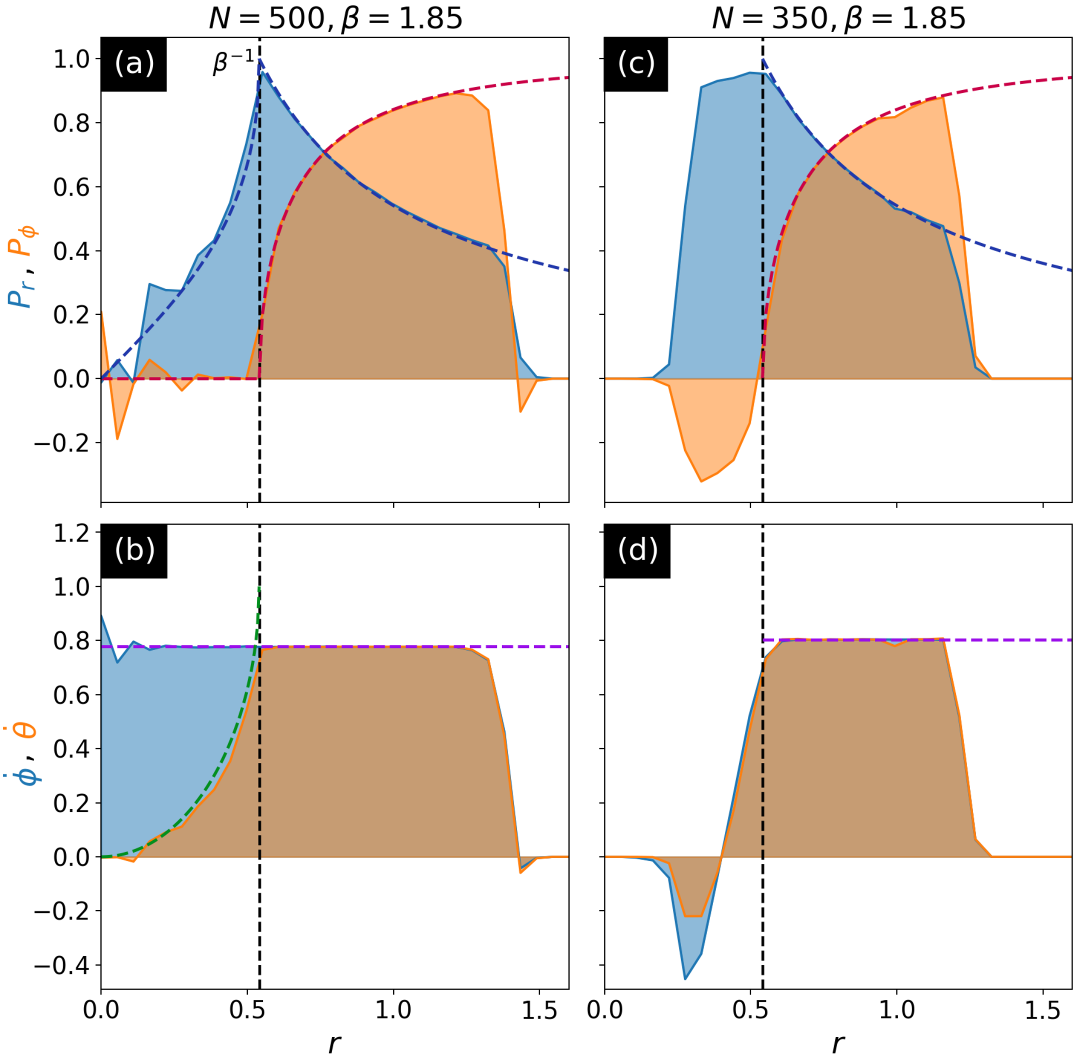

Source: (CANAVELLO et al., 2024)

for P_r and P_ϕ continue to provide a valid description of the system over all r.

By looking at the behavior of individual particles in each region, a deeper insight of the system can be obtained. Figure 21 shows the radial position r and tilt angle χ of 4 particles over time, with two of them being in the outer region and two in the inner region for a system with $N = 500$, $\beta = 1.85$ and $D = 0$. The radial distances display small oscillations of order $\delta r \sim \sigma/2$ (even though there is no thermal noise) and these oscillations are strongly correlated between all four particles, indicating an excitation of a collective mode. This phenomenon

Figure 21 – Temporal evolution of (a) radial distance r (b, c) tilt angle $\chi = \theta - \varphi$ for four different particles in a system with $N = 500$, $\sigma = 0.1$, $\beta = 1.85$ and $D = 0$. Dashed lines indicate analytical predictions from Equations (5.8) and (5.9). For particles in the outside region, in panel (b), χ fluctuates around a constant value at large t. Meanwhile χ performs full revolutions for the particles in the inside region.

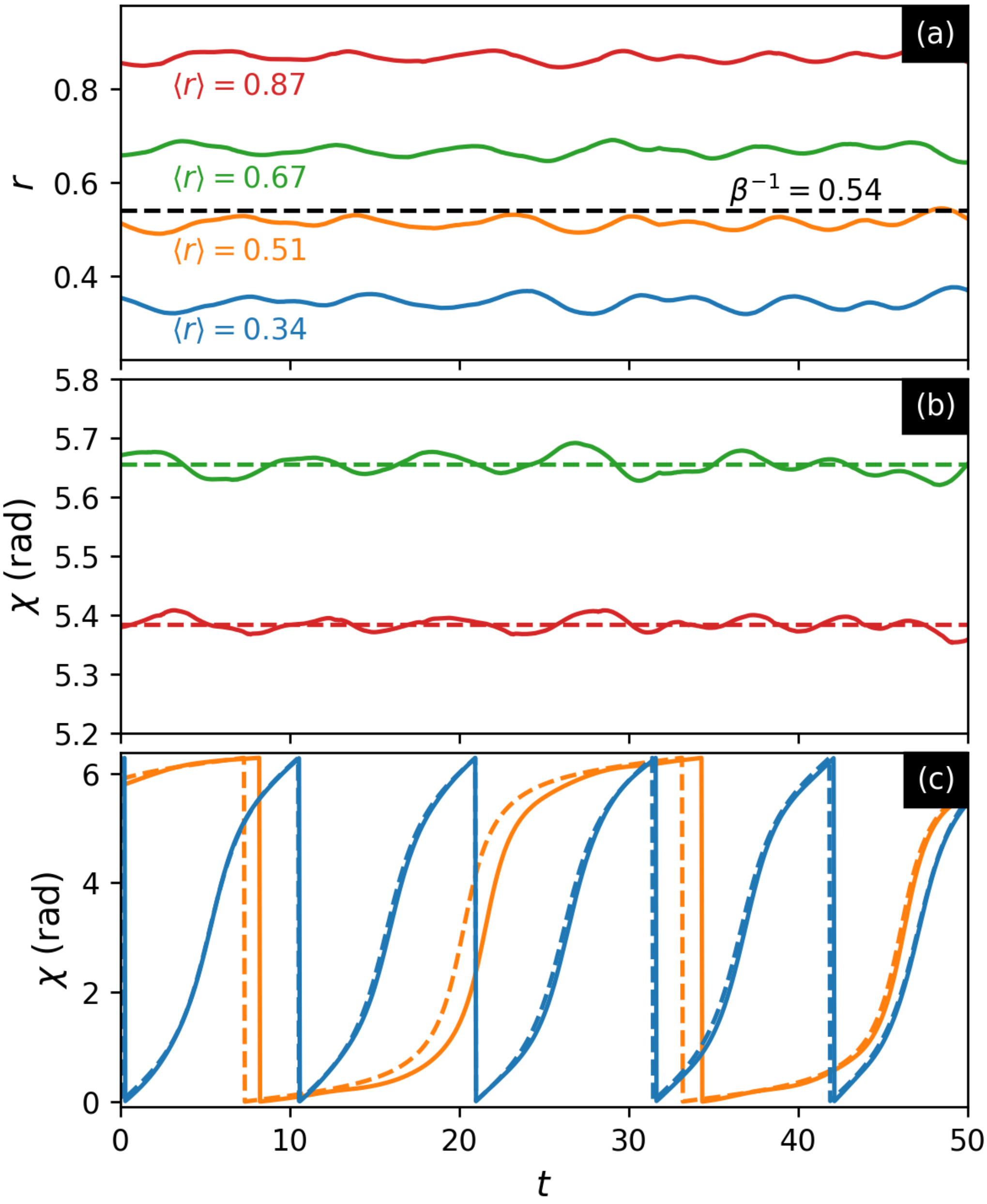

Source: (CANAVELLO et al., 2024)

manifests as a slight “wobble” of the inner region in regard to the outer region. This result undermines the assumptions of a rigid body system, but as the oscillations are small the results from Section 5.2 still hold remarkably well.

Figure 21 presents a system in the uniform vortex state, with the left panel using colors to display the orientation θ and the right panel showing the tilt angle χ. Above the shear band

Figure 22 – Snapshot of a system in the uniform vortex (UV) state with parameters $N = 500, \sigma = 0.1$, $\beta = 1.85$ and $D = 0.0$. On the left, colors indicate the internal orientation angle θ of each particle, while on the right panel the colors encode the tilt angle χ instead. Above the shear band boundary, the color is uniform for all particles with the same radius and constant over time, while in the inner region, the colors are varied and cycle periodically over time, corroborating the results shown in Figure 21.

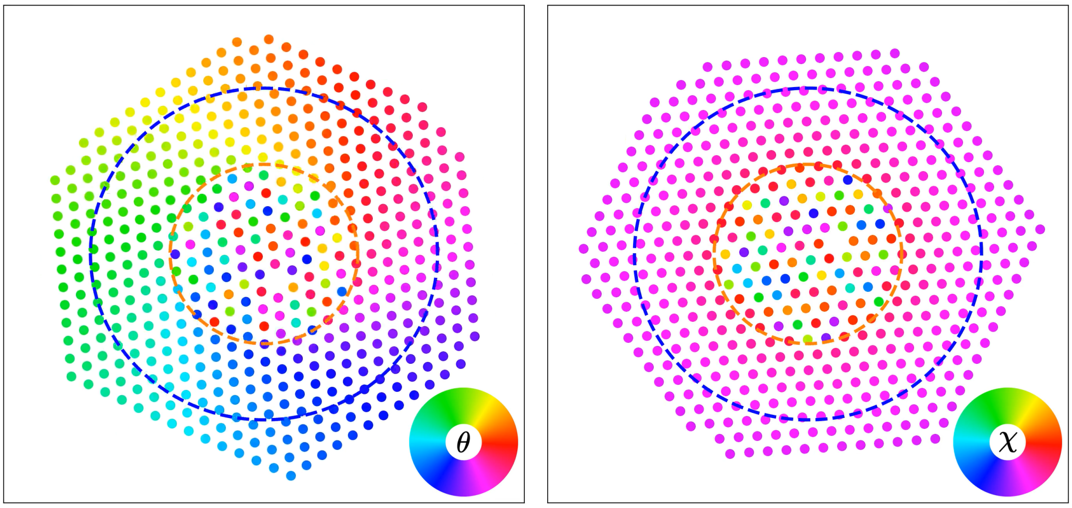

Source: (CANAVELLO et al., 2024) (supplementary material, adapted)

boundary (denoted by the dashed orange line), all particles appear to share the same color, indicating that the tilt angle χ is equal for all of them, and also constant over time. In a rigorous manner, only the particles with equal radius will have equal χ (and color), however the difference is small enough that it can't be easily discerned.

In contrast, within the inner region of the system, the colors are distributed seemingly at random, and they evolve periodically over time. This dynamic behavior is governed by the relation expressed in Equation (5.9). Although particles with the same radius exhibit identical tilt angle frequency $\dot{\chi}$, the initial conditions encoded within each particle lead to variations in χ even for particles of the same radius, explaining the difference in colors.

Figure 23(c, d) illustrates the system configuration for a small value of β, corresponding to a large inner region of the system, particularly when compared to the configuration seen in Figure 15(c). The seemingly random orientations for particles within the orange dashed boundary are a consequence of $\dot{\chi} \neq 0$ and can be described by Equation (5.9) and can also be seen in Figure 21(c).

Looking at the system from the laboratory frame of reference, the position of each *color* in the outer region of the system remain static over time, while all particles rotate uniformly at a constant angular velocity. Conversely, in a rotating frame of reference with the same angular

Figure 23 – Snapshots of particles positions and orientations at $\beta = 1.85$ and $D = 0$. All systems are rotating clockwise in this case. The blue line and orange line indicate, respectively, the critical isocline at $r = 1$ and the shear band limit $r = 1/\beta$. Orientations are indicated by colors in the same way as Figure 15.

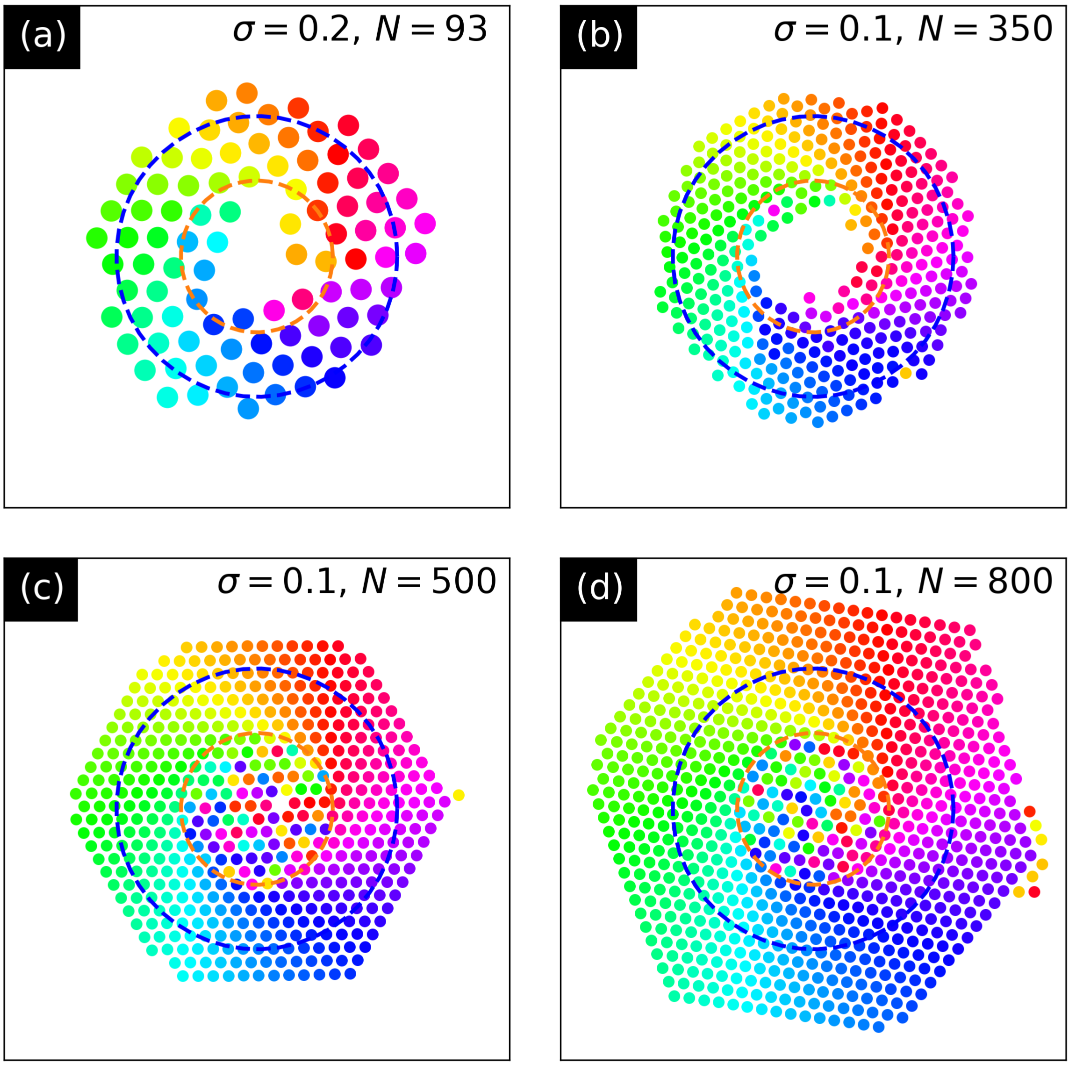

Source: (CANAVELLO et al., 2024)

speed ω of the system, and using colors to represent χ instead of θ, all particles appear static in time (since all of them have the same ω). The particles in the outer region then assume a single static color, while the particles within the inner region undergo continuous color changes, reflecting the results shown in Figure 21 and 22. This rotating frame view also facilitates the observation of intrinsic elastic deformations in the system, which are what allows the system to violate the condition $\dot{\chi} = 0$ for the inner region, while still maintaining a quasi-rigid-body structure and stabilize the UV phase.

5.4.4 Shear-banded vortex

Under low β (meaning a large inner region) and low filling fraction, the system might not be in a fully compact state. This happens because the particles with $r < 1/\beta$ will try to climb the potential towards $r = 1/\beta$, and since there aren't enough particles to "push" them down, this creates an area in the center without any particles. Examples of the shear-banded vortex (SBV) phase can be seen in Figures 15 and 23. The images also show the two mechanisms in which the SBV may transition into the uniform vortex (UV) phase, with the panels (b) and (c) of Figure 15 showing a transition induced by an increase in β, thus reducing the inner region, and panels (b) and (c) of Figure 23 showing a transition induced by an increase in the filling fraction, which compacts the cluster and the empty region can no longer sustain itself.

The transition between SBV and UV can also be visualized in Figure 24, which plots the internal (R_{int}) and external (R_{int}) radii, defined as the time-averaged radial position of the inner- and outermost particles, as a function of β for a system with $N = 93$, $\sigma = 0.2$ and $D = 0$. For $\beta \lesssim 1$ there is no vortex phase, as the system is in the climbing state with a distinct ring shape, which is characterized by large R_{int} and $\omega = 0$. Increasing β allows the system to start rotating, however there is a markedly distinct behavior in each region, as the particles inside the inner region have a significantly lower angular velocity. As β increases, R_{int} decreases and the inner angular velocity becomes closer to the outer one. At $\beta \gtrsim 3$ the inner radius reaches its lowest value, of order σ, and the angular velocity for the system becomes uniform. The simultaneous cluster compaction and uniformity of the angular velocities marks the transition from the SBV to UV phase.

As the regions have different angular velocities, the analytical results obtained for the UV phase in Section 5.2 are no longer valid, which is shown in Figure 20(c, d). While the predictions for $r > 1/\beta$ still hold since the particles are closely packed and have the same angular velocity there. In contrast, the inner region shows a completely different behavior, with $\dot{\varphi}$ and $\dot{\theta}$ even taking on the opposite sign of the outer region. Another noteworthy characteristic of this phase is the considerable value of P_r observed in the inner region, indicating that the particles are trying to migrate towards the outer region of the system.

To better understand what happens in this phase, it helps to think of particles in the inner region as being in the climbing state, and are kept in there due to the steepness of the potential combined with forces exerted from particles in the outer region. When climbing the potential, these frustrated particles will trend either clockwise or counter-clockwise and, if it matches the

Figure 24 – Example of a transition between shear-banded vortex and uniform vortex phases by increasing β for a system with $N = 93$, $\sigma = 0.2$ and $D = 0$. (a) External (R_{ext}) and internal (R_{int}) radii of the cluster as a function of β. The dashed black line indicates the $1/\beta$ boundary which marks a difference in behavior of the system. (b) Angular speed ω for particles in the outside region (black line) and inner region (blue line) as a function of β. The regions are separated by the $1/\beta$ boundary. At $\beta \simeq 3$ (vertical dashed line), the system fully transitions into the UV phase, with the internal radius becoming the order of σ and the angular speed being constant across both regions.

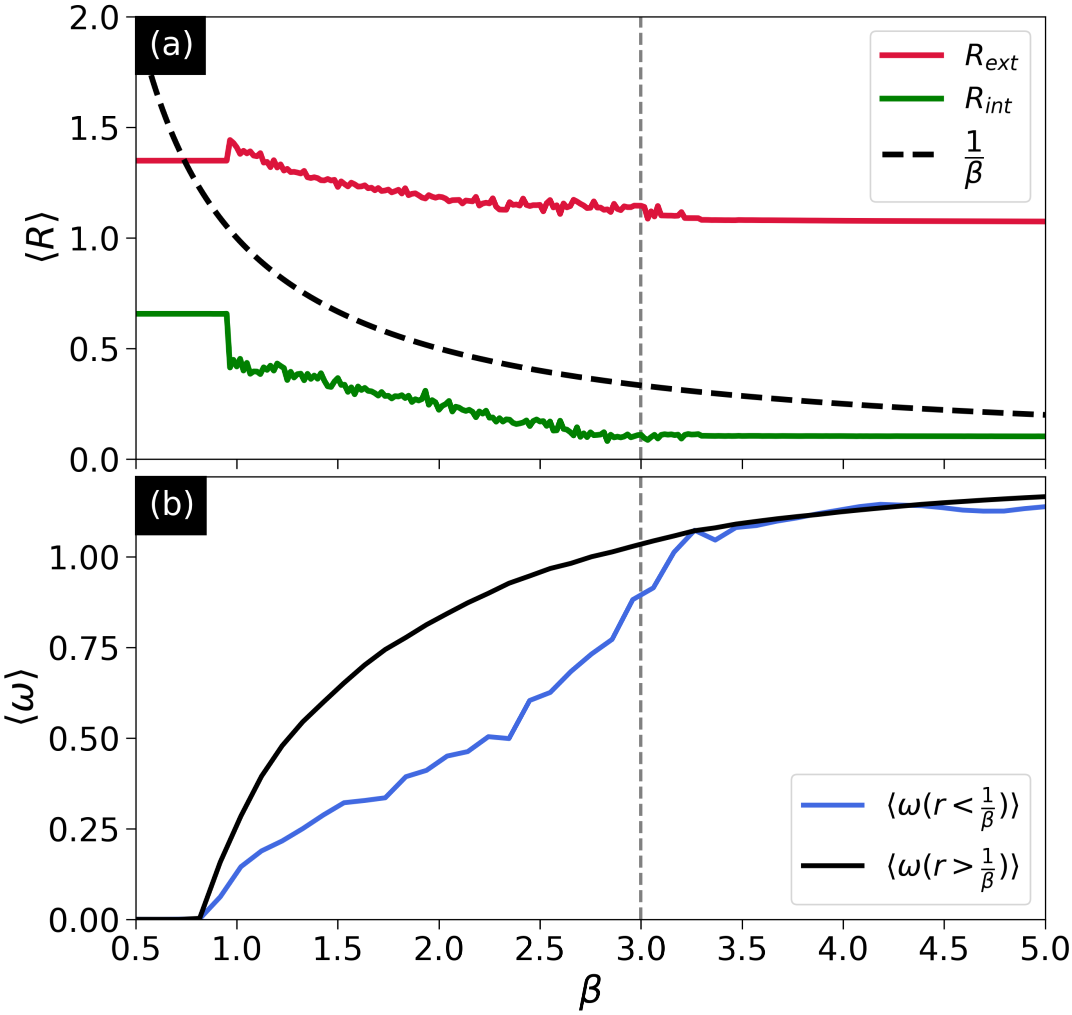

Source: (CANAVELLO et al., 2024)

orientation of the outer band, those particles will have a higher chance of being assimilated due to sliding events that can rearrange the system. When a frustrated particle gets lucky and is absorbed into the outer region, one of the particles from the outer falls back into the inner region, becoming frustrated, which repeats the process. This continued cycle makes it so all particles rotating in the same direction as the outer band are eventually assimilated into the outer region, while the particles left inside are the ones running contrary to it, essentially acting like a filter. Which explains why the particles that in the inner region tend to rotate on the opposite direction of the outer region.

5.4.5 Multi-cluster phase

At low filling fractions, it is possible for the system to not assume a compact form and instead split into different clusters, seen in Figure 15(e). In this case, characteristics of both vortex and ferromagnetic states are seen. Particles are polarized inside each cluster, which acts as a single particle, like in the ferromagnetic state and obeying Equations (5.5). Each cluster, however, rotates around the potential with the same angular velocity, thus obeying the vortex phase requirements.

Figure 25 – Heatmaps for the average number of clusters $\langle N_c \rangle$ in the $\sigma - N$ space (thus changing f) at different values of β with $D = 0$. The white dashed line indicates the $f = 1$ condition, at which point the system would be completely filled from the origin to the isocline. As this is an average over time and noise, values might be non-integers, but each individual configuration has an integer amount of clusters.

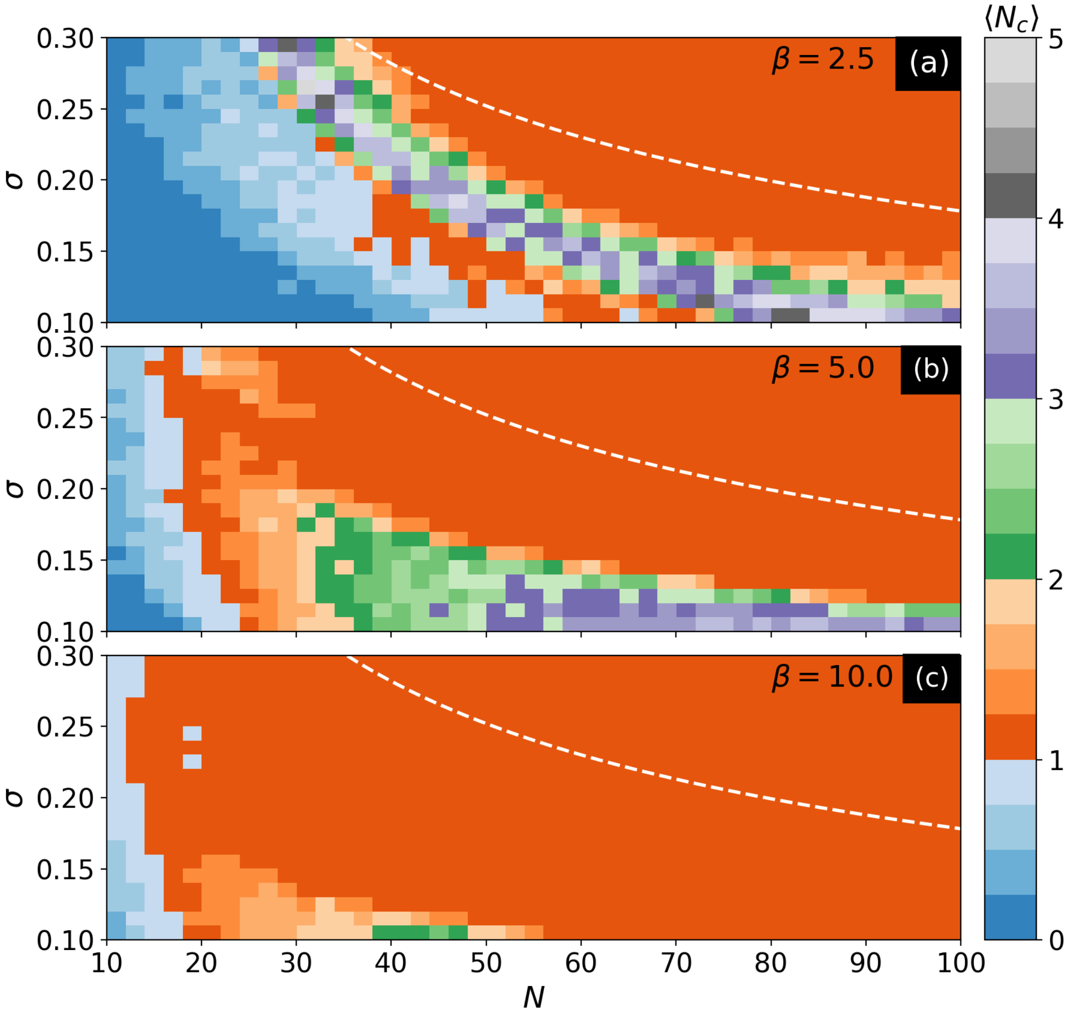

Source: (CANAVELLO et al., 2024)

In Figure 25, the average number of clusters, denoted by $\langle N_c \rangle$, for configurations on the $\sigma - N$ space are measured. The algorithm DBSCAN (SCHUBERT et al., 2017) was used to calculate the number of clusters in the systems, with a particle being considered part of a cluster if it has at least 3 particles within a 1.5σ radius (core point), or if it is directly reachable by a core point. Particles that do not belong to any cluster are treated as outliers rather than as individual one-particle clusters. This choice ensures that systems without any aggregation are characterized as having zero clusters, rather than being interpreted as containing N separate clusters.

As the same configuration can evolve into different amount of clusters, the resulting $\langle N_\mathsf{c} \rangle$ may be non-integer, and a complex relationship between σ and N is observed. In very dilute systems (low N and σ), particles are too far apart to feel each other and may not form clusters, leading to configurations with zero clusters and $\langle N_\mathsf{c} \rangle < 1$. A limiting condition of $f = 1$ was established, as it is the point in which particles completely occupy the system up to the critical isocline, making it very hard for particles to have sufficient space between them to form multiple clusters. Since the radial position of each cluster is given by $R = \beta^{-1/2}$, when β increases the trajectory of the clusters become tighter, which leads to all particles eventually merging together into a single cluster, which is exactly what is seen on Panel (c) for $\beta = 10$. The system will then evolve into one of the other collective phases described before.

5.5 TAKEAWAYS

An analytical and numerical investigation was done to investigate an interacting system that couples self-aligning torque with an external harmonic potential. Multiple new phases were observed, some reminiscent of those in single particle system, but new phases are also present, some with surprising results. The angular mobility β plays a key role in the vast wealth of the system's phases. At low β, the system does not display orientational dynamics and settles into a phase that is similar to the climbing phase for one-particle systems. However, increasing β above a critical value will break the rotational symmetry of the system and it'll start rotating. This rotation can manifest in different ways depending on the values of not only β, but also the filling fraction f and the thermal noise D. The ones studied in this chapter were: a ferromagnetic state, where the orientations of all particles are the same and the system acts like a singular particle; a uniform vortex state, in which all particles have the same angular velocity; a shear-banded vortex, that separates the system into two an external region with constant angular velocity and a climbing phase in the inner region; and a multi cluster phase, where the system separates into several small clusters that rotate around the potential, combining elements of both the ferromagnetic and vortex states.

A rigid body analytical model was developed for the close packed phases, those being the ferromagnetic and uniform vortex ones. However, a peculiarity emerges in the latter case: although all particles share the same angular velocity, their polarization vectors rotate at a different frequency for particles with $r < 1/\beta$. This behavior appears to contradict the conditions expected of rigid body motion. In fact, the system exhibits slight deformations over time, which facilitate a decoupling between its translational and polarization dynamics. Despite these deformations, the analytical formulas found were in great agreement with the numerical simulation results. Another intriguing phenomenon is the appearance of a shear-banded phase, which features two regions rotating in opposite directions and at different angular velocities. This behavior arises from a filtering mechanism: particles aligning with the rotation of the outer band are absorbed into it, while those remaining in the inner region rotate in the opposite direction. As a result, the system self-organizes into a state where the inner and outer bands exhibit counter-rotating motion. These results demonstrate how a combination of self-alignment torque, confining potential and interparticle interactions can give rise to a rich and complex phase space.

6 DISCUSSION AND FUTURE PERSPECTIVES

In this work, the collective behavior of active matter systems with self-aligning torques was systematically investigated under two distinct configurations: periodic boundary conditions and harmonic confinement, and these scenarios were compared with the dynamics of a single particle to elucidate the role of collective effects. Under periodic boundaries, seen in Chapter 4, a flocking transition was identified at a critical self-alignment strength, which remained robust even with the introduction of periodic obstacles. However, the inclusion of anisotropic obstacles led to a notable transition from two-dimensional to one-dimensional collective motion, demonstrating how a substrate can modify emergent behavior. In the harmonically confined case, studied in Chapter 5, a rich phase space was uncovered, revealing novel states such as a ferromagnetic phase, where particles share a common orientation, and a vortex phase, characterized by uniform angular motion among particles.

A key insight from these results is the central role played by the self-alignment torque, which acts as a fundamental control parameter in determining the system's macroscopic behavior. Despite its relevance to numerous natural and artificial systems such as bacterial colonies and robotic swarms, this type of system remains underexplored. The findings presented here highlight its importance, suggesting that self-alignment can be leveraged as a design principle for tuning collective dynamics. These results could aid the development of smart active materials and methods to control polarization direction in populations (WOODHOUSE; RONELLENFITSCH; DUNKEL, 2018; ZHENG et al., 2023; LAZZARI; DAUCHOT; BRITO, 2024; DJELLOULI et al., 2024).

A promising direction for future research lies in extending these studies to strongly disordered or heterogeneous environments. This includes complex substrates such as porous or patchy media, where spatial disorder can significantly affect the long-range order, mobility, and clustering behavior of active particles (CHEPIZHKO; ALTMANN; PERUANI, 2013; CHEPIZHKO; PERUANI, 2013; MORIN et al., 2017; CHEN et al., 2022; MODICA; XI; TAKATORI, 2022; MODICA; OMAR; TAKATORI, 2023; SINAASAPPEL et al., 2025; SHINDE; VOITURIEZ; CALLAN-JONES, 2025). Investigating how a self-aligning component would interacts with such complex geometries could yield insights into real-world systems where disorder is intrinsic, such as cellular tissues, biofilms, or geological porous structures. The interplay between local alignment rules and substrate-induced randomness presents a rich field for both theoretical modeling and experimental validation.

Another avenue of research involves boundary interactions, particularly in systems where the torque is influenced by the walls or interfaces (OSTAPENKO et al., 2018). Recent experimental studies suggest that the trajectories (CODUTTI et al., 2022) and accumulation near surfaces (PÉREZ-ESTAY et al., 2024) are some of the mechanisms that are mediated by boundary interactions. Understanding how self-alignment modifies these effects could provide new strategies for controlling active flows, enhancing transport in confined geometries, or optimizing particle sorting and filtering.

While these results concern an homogeneous population, the question of how heterogeneous mixtures with distinct sizes and torque strengths is still open and relevant, which can also be investigated further. Overall, the results of this thesis open several avenues for advancing both the theoretical understanding and practical applications of active matter in structured environments.

REFERENCES

ABELSON, H.; SUSSMAN, G. J. *Structure and Interpretation of Computer Programs*. 2nd. ed. Cambridge: MIT Press, 1996. ISBN 978-0262510875.

ABRAMOWITZ, M.; STEGUN, I. A. *Handbook of Mathematical Functions: With Formulas, Graphs, and Mathematical Tables*. Tenth printing. New York: Dover Publications, 1964. ISBN 0-486-61272-4.

ARNOLD, V. I. *Mathematical Methods of Classical Mechanics*. Second. New York: Springer-Verlag, 1989. 508 p. (Graduate Texts in Mathematics, v. 60). ISBN 978-0387968902.

ARROYO, M.; HELTAI, L.; MILLÁN, D.; DESIMONE, A. Reverse engineering the euglenoid movement. *Proceedings of the National Academy of Sciences*, National Academy of Sciences, v. 109, n. 44, p. 17874–17879, 2012.

BACONNIER, P.; DAUCHOT, O.; DÉMERY, V.; DÜRING, G.; HENKES, S.; HUEPE, C.; SHEE, A. Self-aligning polar active matter. *Reviews of Modern Physics*, APS, v. 97, n. 1, p. 015007, 2025.

BACONNIER, P.; SHOHAT, D.; LÓPEZ, C. H.; COULAIS, C.; DÉMERY, V.; DÜRING, G.; DAUCHOT, O. Selective and collective actuation in active solids. *Nature Physics*, Nature Publishing Group UK London, v. 18, n. 10, p. 1234–1239, 2022.

BALLERINI, M.; CABIBBO, N.; CANDELIER, R.; CAVAGNA, A.; CISBANI, E.; GIARDINA, I.; LECOMTE, V.; ORLANDI, A.; PARISI, G.; PROCACCINI, A. et al. Interaction ruling animal collective behavior depends on topological rather than metric distance: Evidence from a field study. *Proceedings of the national academy of sciences*, National Acad Sciences, v. 105, n. 4, p. 1232–1237, 2008.

BASU, U.; MAJUMDAR, S. N.; ROSSO, A.; SCHEHR, G. Active brownian motion in two dimensions. *Phys. Rev. E*, American Physical Society, v. 98, p. 062121, Dec 2018. Available at: <https://link.aps.org/doi/10.1103/PhysRevE.98.062121>.

BECHINGER, C.; LEONARDO, R. D.; LÖWEN, H.; REICHHARDT, C.; VOLPE, G.; VOLPE, G. Active particles in complex and crowded environments. *Rev. Mod. Phys.*, American Physical Society, v. 88, p. 045006, Nov 2016. Available at: <https://link.aps.org/doi/10.1103/RevModPhys.88.045006>.

BERG, H. C. *E. coli in Motion*. New York: Springer New York, 2004. ISBN 978-0-387-21638-6.

BIALKÉ, J.; SPECK, T.; LÖWEN, H. Active colloidal suspensions: Clustering and phase behavior. *Journal of Non-Crystalline Solids*, Elsevier, v. 407, p. 367–375, 2015.

BONILLA, L. L. Active ornstein-uhlenbeck particles. *Physical Review E*, APS, v. 100, n. 2, p. 022601, 2019.

BOWICK, M. J.; FAKHRI, N.; MARCHETTI, M. C.; RAMASWAMY, S. Symmetry, thermodynamics, and topology in active matter. *Physical Review X*, APS, v. 12, n. 1, p. 010501, 2022.

BRAŃKA, A.; HEYES, D. Algorithms for brownian dynamics computer simulations: Multivariable case. *Physical Review E*, APS, v. 60, n. 2, p. 2381, 1999.

BREONI, D.; SCHMIEDEBERG, M.; LÖWEN, H. Active brownian and inertial particles in disordered environments: Short-time expansion of the mean-square displacement. *Physical Review E*, APS, v. 102, n. 6, p. 062604, 2020.

BUTTINONI, I.; VOLPE, G.; KÜMMEL, F.; VOLPE, G.; BECHINGER, C. Active brownian motion tunable by light. *Journal of Physics: Condensed Matter*, IOP Publishing, v. 24, n. 28, p. 284129, 2012.

CANAVELLO, D.; DAMASCENA, R. H.; CABRAL, L. R. E.; SILVA, C. C. de S. Polar order, shear banding, and clustering in confined active matter. *Soft Matter*, The Royal Society of Chemistry, v. 20, p. 2310–2320, 2024. Available at: <http://dx.doi.org/10.1039/D3SM01721D>.

CANAVELLO, D.; REICHHARDT, C.; REICHHARDT, C. J. O.; SILVA, C. C. de S. Polarization and dynamic phases of aligning active matter in periodic obstacle arrays. *Soft Matter*, The Royal Society of Chemistry, v. 21, p. 1760–1767, 2025. Available at: <http://dx.doi.org/10.1039/D4SM01404A>.

CAPRINI, L.; MARCONI, U. M. B.; PUGLISI, A. Spontaneous velocity alignment in motility-induced phase separation. *Physical review letters*, APS, v. 124, n. 7, p. 078001, 2020.

CATES, M. E.; TAILLEUR, J. When are active brownian particles and run-and-tumble particles equivalent? consequences for motility-induced phase separation. *EPL (Europhysics Letters)*, IOP Publishing, v. 101, n. 2, p. 20010, Jan 2013. ISSN 1286-4854. Available at: <http://dx.doi.org/10.1209/0295-5075/101/20010>.

CATES, M. E.; TAILLEUR, J. Motility-induced phase separation. *Annual Review of Condensed Matter Physics*, Annual Reviews, v. 6, n. 1, p. 219–244, Mar 2015. ISSN 1947-5462. Available at: <http://dx.doi.org/10.1146/annurev-conmatphys-031214-014710>.

CAVAGNA, A.; CIMARELLI, A.; GIARDINA, I.; PARISI, G.; SANTAGATI, R.; STEFANINI, F.; VIALE, M. Scale-free correlations in starling flocks. *Proceedings of the National Academy of Sciences*, National Academy of Sciences, v. 107, n. 26, p. 11865–11870, 2010.

CHATÉ, H. Dry aligning dilute active matter. *Annual Review of Condensed Matter Physics*, Annual Reviews, v. 11, n. 1, p. 189–212, 2020.

CHAUDHURI, D.; DHAR, A. Active brownian particle in harmonic trap: exact computation of moments, and re-entrant transition. *Journal of Statistical Mechanics: Theory and Experiment*, IOP Publishing, v. 2021, n. 1, p. 013207, Jan 2021. ISSN 1742-5468. Available at: <http://dx.doi.org/10.1088/1742-5468/abd031>.

CHEN, L.; LEE, C. F.; MAITRA, A.; TONER, J. Packed swarms on dirt: Two-dimensional incompressible flocks with quenched and annealed disorder. *Physical Review Letters*, APS, v. 129, n. 18, p. 188004, 2022.

CHEN, Y.; ZHOU, L.; TANG, Y.; SINGH, J. P.; BOUGUILA, N.; WANG, C.; WANG, H.; DU, J. Fast neighbor search by using revised kd tree. *Information Sciences*, Elsevier, v. 472, p. 145–162, 2019.

CHEPIZHKO, O.; ALTMANN, E. G.; PERUANI, F. Optimal noise maximizes collective motion in heterogeneous media. *Physical review letters*, APS, v. 110, n. 23, p. 238101, 2013.

CHEPIZHKO, O.; PERUANI, F. Diffusion, subdiffusion, and trapping of active particles in heterogeneous media. *Physical review letters*, APS, v. 111, n. 16, p. 160604, 2013.

CICHOS, F.; GUSTAVSSON, K.; MEHLIG, B.; VOLPE, G. Machine learning for active matter. *Nature Machine Intelligence*, Nature Publishing Group UK London, v. 2, n. 2, p. 94–103, 2020.

CODUTTI, A.; CHARSOOGHI, M. A.; CERDÁ-DOÑATE, E.; TAÏEB, H. M.; ROBINSON, T.; FAIVRE, D.; KLUMPP, S. Interplay of surface interaction and magnetic torque in single-cell motion of magnetotactic bacteria in microfluidic confinement. *Elife*, eLife Sciences Publications Limited, v. 11, p. e71527, 2022.

DAMASCENA, R. H.; CABRAL, L. R. E.; SILVA, C. C. d. S. Coexisting orbits and chaotic dynamics of a confined self-propelled particle. *Phys. Rev. E*, American Physical Society, v. 105, p. 064608, Jun 2022. Available at: <https://link.aps.org/doi/10.1103/PhysRevE.105.064608>.

DAMASCENA, R. H.; SILVA, C. C. de S. Noise-induced escape of a self-propelled particle from metastable orbits. *Phys. Rev. E*, American Physical Society, v. 108, p. 044605, Oct 2023. Available at: <https://link.aps.org/doi/10.1103/PhysRevE.108.044605>.

DAUCHOT, O.; DÉMERY, V. Dynamics of a self-propelled particle in a harmonic trap. *Phys. Rev. Lett.*, American Physical Society, v. 122, p. 068002, Feb 2019. Available at: <https://link.aps.org/doi/10.1103/PhysRevLett.122.068002>.

DESEIGNE, J.; DAUCHOT, O.; CHATÉ, H. Collective motion of vibrated polar disks. *Physical review letters*, APS, v. 105, n. 9, p. 098001, 2010.

DESEIGNE, J.; LÉONARD, S.; DAUCHOT, O.; CHATÉ, H. Vibrated polar disks: spontaneous motion, binary collisions, and collective dynamics. *Soft Matter*, Royal Society of Chemistry, v. 8, n. 20, p. 5629–5639, 2012.

DJELLOULI, A.; RAEMDONCK, B. V.; WANG, Y.; YANG, Y.; CAILLAUD, A.; WEITZ, D.; RUBINSTEIN, S.; GORISSEN, B.; BERTOLDI, K. Shell buckling for programmable metafluids. *Nature*, Nature Publishing Group UK London, v. 628, n. 8008, p. 545–550, 2024.

DOOSTMOHAMMADI, A.; IGNÉS-MULLOL, J.; YEOMANS, J. M.; SAGUÉS, F. Active nematics. *Nature communications*, Nature Publishing Group UK London, v. 9, n. 1, p. 3246, 2018.

EBBENS, S.; TU, M.-H.; HOWSE, J. R.; GOLESTANIAN, R. Size dependence of the propulsion velocity for catalytic janus-sphere swimmers. *Physical Review E—Statistical, Nonlinear, and Soft Matter Physics*, APS, v. 85, n. 2, p. 020401, 2012.

ELGETI, J.; WINKLER, R. G.; GOMPPER, G. Physics of microswimmers—single particle motion and collective behavior: a review. *Reports on Progress in Physics*, IOP Publishing, v. 78, n. 5, p. 056601, apr 2015. Available at: <https://dx.doi.org/10.1088/0034-4885/78/5/056601>.

FEHLINGER, S.; LIEBCHEN, B. Collective behavior of active molecules: Dynamic clusters, holes, and active fractalytes. *Physical Review Research*, APS, v. 5, n. 3, p. L032038, 2023.

FERRANTE, E.; TURGUT, A. E.; DORIGO, M.; HUEPE, C. Collective motion dynamics of active solids and active crystals. *New Journal of Physics*, IOP Publishing, v. 15, n. 9, p. 095011, 2013.

FILY, Y.; MARCHETTI, M. C. Athermal phase separation of self-propelled particles with no alignment. *Physical Review Letters*, American Physical Society (APS), v. 108, n. 23, p. 235702, Jun 2012. ISSN 1079-7114. Available at: <http://dx.doi.org/10.1103/PhysRevLett.108.235702>.

GEYER, D.; MARTIN, D.; TAILLEUR, J.; BARTOLO, D. Freezing a flock: Motility-induced phase separation in polar active liquids. *Physical Review X*, American Physical Society, v. 9, p. 031043, Sep 2019. Available at: <https://link.aps.org/doi/10.1103/PhysRevX.9.031043>.

GILPIN, W.; BULL, M. S.; PRAKASH, M. The multiscale physics of cilia and flagella. *Nature Reviews Physics*, Nature Publishing Group UK London, v. 2, n. 2, p. 74–88, 2020.

GINELLI, F. The physics of the vicsek model. *The European Physical Journal Special Topics*, Springer, v. 225, p. 2099–2117, 2016.

GIOMI, L.; HAWLEY-WELD, N.; MAHADEVAN, L. Swarming, swirling and stasis in sequestered bristle-bots. *Proceedings of the Royal Society A: Mathematical, Physical and Engineering Sciences*, The Royal Society Publishing, v. 469, n. 2151, p. 20120637, 2013.

GONZÁLEZ-ALBALADEJO, R.; CARPIO, A.; BONILLA, L. Scale-free chaos in the confined vicsek flocking model. *Physical Review E*, APS, v. 107, n. 1, p. 014209, 2023.

GOULD, H.; TOBOCHNIK, J.; CHRISTIAN, W. *An Introduction to Computer Simulation Methods: Applications to Physical Systems*. Third. San Francisco: Addison-Wesley, 2007. 796 p. ISBN 978-0-8053-7758-3.

GRADSHTEYN, I.; RYZHIK, I. *Table of Integrals, Series, and Products*. Eight. Amsterdam: Academic Press, 2014. 1184 p. ISBN 978-0-12-384933-5.

GREINER, A.; STRITTMATTER, W.; HONERKAMP, J. Numerical integration of stochastic differential equations. *Journal of Statistical Physics*, Springer, v. 51, p. 95–108, 1988.

HENNES, M.; WOLFF, K.; STARK, H. Self-induced polar order of active brownian particles in a harmonic trap. *Physical Review Letters*, American Physical Society (APS), v. 112, n. 23, p. 238104, Jun 2014. ISSN 1079-7114. Available at: <http://dx.doi.org/10.1103/PhysRevLett.112.238104>.

HIGHAM, D. J. An algorithmic introduction to numerical simulation of stochastic differential equations. *SIAM review*, SIAM, v. 43, n. 3, p. 525–546, 2001.

HOFSTADTER, D. R. *Gödel, Escher, Bach: An Eternal Golden Braid*. New York: Basic Books, 1979. 777 p. ISBN 978-0-465-02656-2.

HOWSE, J. R.; JONES, R. A. L.; RYAN, A. J.; GOUGH, T.; VAFABAKHSH, R.; GOLESTANIAN, R. Self-motile colloidal particles: From directed propulsion to random walk. *Physical Review Letters*, American Physical Society (APS), v. 99, n. 4, p. 048102, Jul 2007. ISSN 1079-7114. Available at: <http://dx.doi.org/10.1103/PhysRevLett.99.048102>.

KÖDDERMANN, T.; LUDWIG, R.; PASCHEK, D. On the validity of stokes–einstein and stokes–einstein–debye relations in ionic liquids and ionic-liquid mixtures. *ChemPhysChem*, Wiley Online Library, v. 9, n. 13, p. 1851–1858, 2008.

KOENDERINK, G. H.; ZHANG, H.; AARTS, D. G.; LETTINGA, M. P.; PHILIPSE, A. P.; NÄGELE, G. On the validity of stokes–einstein–debye relations for rotational diffusion in colloidal suspensions. *Faraday discussions*, Royal Society of Chemistry, v. 123, p. 335–354, 2003.

LAM, K.-D. N. T.; SCHINDLER, M.; DAUCHOT, O. Self-propelled hard disks: implicit alignment and transition to collective motion. *New Journal of Physics*, IOP Publishing, v. 17, n. 11, p. 113056, 2015.

LAZZARI, D.; DAUCHOT, O.; BRITO, C. Tuning collective actuation of active solids by optimizing activity localization. *Soft Matter*, Royal Society of Chemistry, v. 20, n. 43, p. 8570–8580, 2024.

LÖWEN, H. Inertial effects of self-propelled particles: From active brownian to active langevin motion. *The Journal of chemical physics*, AIP Publishing, v. 152, n. 4, 2020.

MAKRIS, N. C.; RATILAL, P.; JAGANNATHAN, S.; GONG, Z.; ANDREWS, M.; BERTSATOS, I.; GODØ, O. R.; NERO, R. W.; JECH, J. M. Critical population density triggers rapid formation of vast oceanic fish shoals. *Science*, American Association for the Advancement of Science, v. 323, n. 5922, p. 1734–1737, 2009.

MALAKAR, K.; DAS, A.; KUNDU, A.; KUMAR, K. V.; DHAR, A. Steady state of an active brownian particle in a two-dimensional harmonic trap. *Physical Review E*, APS, v. 101, n. 2, p. 022610, 2020.

MARCHETTI, M. C.; FILY, Y.; HENKES, S.; PATCH, A.; YLLANES, D. Minimal model of active colloids highlights the role of mechanical interactions in controlling the emergent behavior of active matter. *Current Opinion in Colloid & Interface Science*, Elsevier, v. 21, p. 34–43, 2016.

MARCHETTI, M. C.; JOANNY, J. F.; RAMASWAMY, S.; LIVERPOOL, T. B.; PROST, J.; RAO, M.; SIMHA, R. A. Hydrodynamics of soft active matter. *Rev. Mod. Phys.*, American Physical Society, v. 85, p. 1143–1189, Jul 2013. Available at: <https://link.aps.org/doi/10.1103/RevModPhys.85.1143>.

MARTIN, D.; O'BYRNE, J.; CATES, M. E.; FODOR, É.; NARDINI, C.; TAILLEUR, J.; WIJLAND, F. V. Statistical mechanics of active ornstein-uhlenbeck particles. *Physical Review E*, APS, v. 103, n. 3, p. 032607, 2021.

MARTÍN-GÓMEZ, A.; LEVIS, D.; DÍAZ-GUILERA, A.; PAGONABARRAGA, I. Collective motion of active brownian particles with polar alignment. *Soft matter*, Royal Society of Chemistry, v. 14, n. 14, p. 2610–2618, 2018. Available at: <https://doi.org/10.1039/C8SM00020D>.

MATTSON, W.; RICE, B. M. Near-neighbor calculations using a modified cell-linked list method. *Computer Physics Communications*, Elsevier, v. 119, n. 2-3, p. 135–148, 1999.

MILSTEIN, G. *Numerical Integration of Stochastic Differential Equations*. Dordrecht: Springer Netherlands, 1995. 169 p. (Mathematics and Its Applications, v. 313). ISBN 978-0792332138.

MIRANDA-FILHO, L.; SOBRAL, T.; SOUZA, A. de; ELSKENS, Y.; ROMAGUERA, A. R. d. C. Lyapunov exponent in the vicsek model. *Physical Review E*, APS, v. 105, n. 1, p. 014213, 2022.

MODICA, K. J.; OMAR, A. K.; TAKATORI, S. C. Boundary design regulates the diffusion of active matter in heterogeneous environments. *Soft Matter*, Royal Society of Chemistry, v. 19, n. 10, p. 1890–1899, 2023.

MODICA, K. J.; XI, Y.; TAKATORI, S. C. Porous media microstructure determines the diffusion of active matter: experiments and simulations. *Frontiers in Physics*, Frontiers Media SA, v. 10, p. 869175, 2022.

MORIN, A.; DESREUMAUX, N.; CAUSSIN, J.-B.; BARTOLO, D. Distortion and destruction of colloidal flocks in disordered environments. *Nature Physics*, Nature Publishing Group UK London, v. 13, n. 1, p. 63–67, 2017.

MOUSSAÏD, M.; HELBING, D.; THERAULAZ, G. How simple rules determine pedestrian behavior and crowd disasters. *Proceedings of the National Academy of Sciences*, National Academy of Sciences, v. 108, n. 17, p. 6884–6888, 2011.

OSTAPENKO, T.; SCHWARZENDAHL, F. J.; BÖDDEKER, T. J.; KREIS, C. T.; CAMMANN, J.; MAZZA, M. G.; BÄUMCHEN, O. Curvature-guided motility of microalgae in geometric confinement. *Phys. Rev. Lett.*, American Physical Society, v. 120, p. 068002, Feb 2018. Available at: <https://link.aps.org/doi/10.1103/PhysRevLett.120.068002>.

PÉREZ-ESTAY, B.; CORDERO, M. L.; SEPÚLVEDA, N.; SOTO, R. Accumulation and depletion of e. coli in surfaces mediated by curvature. *Physical Review E*, APS, v. 109, n. 5, p. 054601, 2024.

POTOTSKY, A.; STARK, H. Active brownian particles in two-dimensional traps. *Europhysics Letters*, IOP Publishing, v. 98, n. 5, p. 50004, 2012.

PRESS, W. H.; TEUKOLSKY, S. A.; VETTERLING, W. T.; FLANNERY, B. P. *Numerical Recipes: The Art of Scientific Computing*. Third. Cambridge: Cambridge University Press, 2007. 1256 p. ISBN 978-0-521-88068-8.

PURCELL, E. M. Life at low reynolds number. *American Journal of Physics*, American Association of Physics Teachers (AAPT), v. 45, n. 1, p. 3–11, Jan. 1977. ISSN 1943-2909. Available at: <http://dx.doi.org/10.1119/1.10903>.

RAMASWAMY, S. The mechanics and statistics of active matter. *Annual Review of Condensed Matter Physics*, v. 1, n. 1, p. 323–345, 2010. Available at: <https://doi.org/10.1146/annurev-conmatphys-070909-104101>.

RAMASWAMY, S. Active matter. *Journal of Statistical Mechanics: Theory and Experiment*, IOP Publishing, v. 2017, n. 5, p. 054002, 2017.

REDNER, G. S.; HAGAN, M. F.; BASKARAN, A. Structure and dynamics of a phase-separating active colloidal fluid. *Biophysical Journal*, Elsevier BV, v. 104, n. 2, p. 640a, Jan 2013. ISSN 0006-3495. Available at: <http://dx.doi.org/10.1016/j.bpj.2012.11.3534>.

REICHHARDT, C.; REICHHARDT, C. J. O. Directional locking effects for active matter particles coupled to a periodic substrate. *Phys. Rev. E*, v. 102, p. 042616, 2020.

REICHHARDT, C. O.; REICHHARDT, C. Ratchet effects in active matter systems. *Annual Review of Condensed Matter Physics*, Annual Reviews, v. 8, n. 1, p. 51–75, 2017.

REYNOLDS, C. W. Flocks, herds and schools: A distributed behavioral model. *ACM SIGGRAPH Computer Graphics*, Association for Computing Machinery (ACM), v. 21, n. 4, p. 25–34, Aug. 1987. ISSN 0097-8930. Available at: <http://dx.doi.org/10.1145/37402.37406>.

ROMANCZUK, P.; BÄR, M.; EBELING, W.; LINDNER, B.; SCHIMANSKY-GEIER, L. Active brownian particles. *The European Physical Journal Special Topics*, Springer Science and Business Media LLC, v. 202, n. 1, p. 1–162, Mar 2012. ISSN 1951-6401. Available at: <http://dx.doi.org/10.1140/epjst/e2012-01529-y>.

SAINTILLAN, D.; SHELLEY, M. J. Active suspensions and their nonlinear models. *Comptes Rendus Physique*, Elsevier, v. 14, n. 6, p. 497–517, 2013.

SCHMIDT, F.; ŠÍPOVÁ-JUNGOVÁ, H.; KÄLL, M.; WÜRGER, A.; VOLPE, G. Non-equilibrium properties of an active nanoparticle in a harmonic potential. *Nature Communications*, Nature Publishing Group, v. 12, n. 1, p. 1–9, 2021.

SCHUBERT, E.; SANDER, J.; ESTER, M.; KRIEGEL, H. P.; XU, X. Dbscan revisited, revisited: Why and how you should (still) use dbscan. *ACM Trans. Database Syst.*, Association for Computing Machinery, New York, NY, USA, v. 42, n. 3, Jul 2017. ISSN 0362-5915. Available at: <https://doi.org/10.1145/3068335>.

SHAEBANI, M. R.; WYSOCKI, A.; WINKLER, R. G.; GOMPPER, G.; RIEGER, H. Computational models for active matter. *Nature Reviews Physics*, Nature Publishing Group UK London, v. 2, n. 4, p. 181–199, 2020.

SHIMOYAMA, N.; SUGAWARA, K.; MIZUGUCHI, T.; HAYAKAWA, Y.; SANO, M. Collective motion in a system of motile elements. *Phys. Rev. Lett.*, American Physical Society, v. 76, p. 3870–3873, May 1996. Available at: <https://link.aps.org/doi/10.1103/PhysRevLett.76.3870>.

SHINDE, R.; VOITURIEZ, R.; CALLAN-JONES, A. Integer defects, flow localization, and bistability on curved active surfaces. *Physical Review Letters*, APS, v. 134, n. 17, p. 178401, 2025.

SILVER, N. *The Signal and the Noise: Why So Many Predictions Fail - But Some Don't.* New York: Penguin Press, 2012. 534 p. ISBN 978-1-59420-411-1.

SINAASAPPEL, R.; FAZELZADEH, M.; HOOIJSCHUUR, T.; DI, Q.; JABBARI-FAROUJI, S.; DEBLAIS, A. Locomotion of active polymerlike worms in porous media. *Phys. Rev. Lett.*, American Physical Society, v. 134, p. 128303, Mar 2025.

SPELLINGS, M.; ENGEL, M.; KLOTSA, D.; SABRINA, S.; DREWS, A. M.; NGUYEN, N. H.; BISHOP, K. J.; GLOTZER, S. C. Shape control and compartmentalization in active colloidal cells. *Proceedings of the National Academy of Sciences*, National Academy of Sciences, v. 112, n. 34, p. E4642–E4650, 2015.

STALLMAN, R.; ROTHWELL, T. *GNU C Language Introduction and Reference Manual.* Boston, 2022.

SUMPTER, D. J. The principles of collective animal behaviour. *Philosophical transactions of the royal society B: Biological Sciences*, The Royal Society London, v. 361, n. 1465, p. 5–22, 2006.

SZABÓ, B.; SZÖLLÖSI, G. J.; GÖNCI, B.; JURÁNYI, Z.; SELMECZI, D.; VICSEK, T. Phase transition in the collective migration of tissue cells: Experiment and model. *Phys. Rev. E*, American Physical Society, v. 74, p. 061908, Dec 2006. Available at: <https://link.aps.org/doi/10.1103/PhysRevE.74.061908>.

TAILLEUR, J.; CATES, M. E. Statistical mechanics of interacting run-and-tumble bacteria. *Physical review letters*, APS, v. 100, n. 21, p. 218103, 2008.

TAKATORI, S. C.; DIER, R. D.; VERMANT, J.; BRADY, J. F. Acoustic trapping of active matter. *Nature communications*, Nature Publishing Group, v. 7, n. 1, p. 1–7, 2016.

TONER, J.; TU, Y. Long-range order in a two-dimensional dynamical xy model: how birds fly together. *Physical review letters*, APS, v. 75, n. 23, p. 4326, 1995.

TONER, J.; TU, Y. Flocks, herds, and schools: A quantitative theory of flocking. *Physical review E*, APS, v. 58, n. 4, p. 4828, 1998.

TONG, D. *Classical Mechanics:*. First. Cambridge: Cambridge University Press, 2025. 400 p. (Lectures on Theoretical Physics, v. 1). ISBN 9781009594547.

VENKATESH, V.; SOUSA, N. de G.; DOOSTMOHAMMADI, A. The interplay of polar and nematic order in active matter: Implications for non-equilibrium physics and biology. *Journal of Physics A: Mathematical and Theoretical*, v. 58, n. 26, p. 263001, 2025.

VENTÉJOU, B.; MAGNIEZ-PAPILLON, I.; BERTIN, E.; PEYLA, P.; DUPONT, A. Behavioral transition of a fish school in a crowded environment. *Physical Review E*, APS, v. 109, n. 6, p. 064403, 2024.

VICSEK, T.; CZIRÓK, A.; BEN-JACOB, E.; COHEN, I.; SHOCHET, O. Novel type of phase transition in a system of self-driven particles. *Physical Review Letters*, American Physical Society (APS), v. 75, n. 6, p. 1226–1229, Aug 1995. ISSN 1079-7114. Available at: <http://dx.doi.org/10.1103/PhysRevLett.75.1226>.

VICSEK, T.; ZAFEIRIS, A. Collective motion. *Physics reports*, Elsevier, v. 517, n. 3-4, p. 71–140, 2012.

VOLPE, G.; BUTTINONI, I.; VOGT, D.; KÜMMERER, H.-J.; BECHINGER, C. Microswimmers in patterned environments. *Soft Matter*, Royal Society of Chemistry, v. 7, n. 19, p. 8810–8815, 2011.

WARD, A. J.; SUMPTER, D. J.; COUZIN, I. D.; HART, P. J.; KRAUSE, J. Quorum decision-making facilitates information transfer in fish shoals. *Proceedings of the National Academy of Sciences*, National Acad Sciences, v. 105, n. 19, p. 6948–6953, 2008.

WEBER, C. A.; HANKE, T.; DESEIGNE, J.; LÉONARD, S.; DAUCHOT, O.; FREY, E.; CHATÉ, H. Long-range ordering of vibrated polar disks. *Physical review letters*, APS, v. 110, n. 20, p. 208001, 2013.

WEEKS, J. D.; CHANDLER, D.; ANDERSEN, H. C. Role of repulsive forces in determining the equilibrium structure of simple liquids. *The Journal of chemical physics*, American Institute of Physics, v. 54, n. 12, p. 5237–5247, 1971.

WENSINK, H. H.; KANTSLER, V.; GOLDSTEIN, R. E.; DUNKEL, J. Controlling active self-assembly through broken particle-shape symmetry. *Physical Review E*, APS, v. 89, n. 1, p. 010302, 2014.

WEXLER, D.; GOV, N.; RASMUSSEN, K. O.; BEL, G. Dynamics and escape of active particles in a harmonic trap. *Phys. Rev. Research*, American Physical Society, v. 2, p. 013003, Jan 2020. Available at: <https://link.aps.org/doi/10.1103/PhysRevResearch.2.013003>.

WOODHOUSE, F. G.; RONELLENFITSCH, H.; DUNKEL, J. Autonomous actuation of zero modes in mechanical networks far from equilibrium. *Physical Review Letters*, APS, v. 121, n. 17, p. 178001, 2018.

YLLANES, D.; LEONI, M.; MARCHETTI, M. How many dissenters does it take to disorder a flock? *New Journal of Physics*, IOP Publishing, v. 19, n. 10, p. 103026, 2017.

ZAMPETAKI, A. V.; LIEBCHEN, B.; IVLEV, A. V.; LÖWEN, H. Collective self-optimization of communicating active particles. *Proceedings of the National Academy of Sciences*, National Academy of Sciences, v. 118, n. 49, p. e2111142118, 2021.

ZHENG, E.; BRANDENBOURGER, M.; ROBINET, L.; SCHALL, P.; LERNER, E.; COULAIS, C. Self-oscillation and synchronization transitions in elastoactive structures. *Physical Review Letters*, APS, v. 130, n. 17, p. 178202, 2023.

APPENDIX A – CALCULATIONS FOR STEADY-STATE SOLUTIONS IN CONFINED CLOSE-PACKED CLUSTERS

This appendix has the details for the calculations done in Section 5.2[1].

Starting with the equations of motion for the system

$$\dot{\boldsymbol{r}}_k + \boldsymbol{r}_k - \sum_{\substack{l=1\\l\neq k}}^{N} \boldsymbol{f}_{kl} = \boldsymbol{n}_k, \tag{A.1}$$

$$\dot{\theta}_k = \beta \left[\boldsymbol{n}_k \times \left(\sum_{\substack{l=1\\l\neq k}}^{N} \boldsymbol{f}_{kl} - \boldsymbol{r}_k\right)\right] \cdot \hat{z} = \beta(\boldsymbol{n}_k \times \dot{\boldsymbol{r}}_k) \cdot \hat{z}, \tag{A.2}$$

for parabolic confinement and arbitrary pairwise interparticle forces given by

$$\boldsymbol{f}_{kl} = f(r_{kl})\frac{\boldsymbol{r}_{kl}}{r_{kl}}, \tag{A.3}$$

where $k,\, l = 1,\, 2,\, \ldots N$ are the particles indexes, $\boldsymbol{r}_k = (r_k \cos\varphi_k,\, r_k \sin\varphi_k)$, $\boldsymbol{n}_k = (\cos\theta_k,\, \sin\theta_k)$ are, respectively, the position and orientation of the k-th particle and $\boldsymbol{r}_{kl} = \boldsymbol{r}_k - \boldsymbol{r}_l$, and $r_{kl} = |\boldsymbol{r}_k - \boldsymbol{r}_l|$ are the interparticle distance vector and magnitude.

It is well known that for general rigid body motion, the system motion consists of a translation plus a rotation of the entire system (ARNOLD, 1989; TONG, 2025). Therefore, the position of the k-th particle of the system can be described by

$$\boldsymbol{r}_k = \boldsymbol{R} + \mathsf{S}\left(\varphi\right) \boldsymbol{s}_k, \tag{A.4}$$

where $\boldsymbol{R} = \sum_{k=1}^{N} \boldsymbol{r}_k / N$ is the position of the system centroid, and

$$\mathsf{S}\left(\phi\right) = \begin{pmatrix} \cos\phi & -\sin\phi \\ \sin\phi & \cos\phi \end{pmatrix}, \tag{A.5}$$

is the rotation matrix, ϕ is a rotation angle in a frame whose origin is at the centroid position, and $\boldsymbol{s}_k$ is the particle position in the moving frame. Substituting this equation in Equation (A.1) gives

$$\dot{\boldsymbol{R}} + \boldsymbol{R} + \mathsf{S}(\phi) \left[\dot{\boldsymbol{s}}_k + \omega\hat{z} \times \boldsymbol{s}_k - \sum_{\substack{l=1\\l\neq k}}^{N} \frac{f(s_{kl})}{s_{kl}} \boldsymbol{s}_{kl}\right] = \boldsymbol{n}_k, \tag{A.6}$$

---

[1] Thanks to Prof. Leonardo Cabral for helping with these results.

where $\omega = \frac{d\phi}{dt}$, $\boldsymbol{s}_{kl} = \boldsymbol{s}_k - \boldsymbol{s}_l$, and $s_{kl} = |\boldsymbol{s}_k - \boldsymbol{s}_l|$. By summing the contributions of all particles to Equation (A.6), the internal forces cancel out and gives

$$\dot{\boldsymbol{R}} + \boldsymbol{R} = \frac{1}{N}\sum_{k=1}^{N} \boldsymbol{n}_k = \langle \boldsymbol{n} \rangle \,. \tag{A.7}$$

As a consequence the centroid motion is governed by the average of the orientation forces of the system. Substituting back this equation in Eqs. (A.6) and (A.2) results in

$$\dot{\boldsymbol{s}}_k + \omega \hat{z} \times \boldsymbol{s}_k - \sum_{\substack{l=1\\ l\neq k}}^{N} \frac{f(s_{kl})}{s_{kl}} \boldsymbol{s}_{kl} = \mathsf{S}(-\phi)\left(\boldsymbol{n}_k - \langle \boldsymbol{n} \rangle\right), \tag{A.8}$$

$$\dot{\theta}_k = \beta \left[\left(\boldsymbol{n}_k \times \dot{\boldsymbol{R}} \right) \cdot \hat{z} + \left(\boldsymbol{\eta}_k \times \dot{\boldsymbol{s}}_k \right) \cdot \hat{z} + \omega \left(\boldsymbol{\eta}_k \cdot \boldsymbol{s}_k \right) \right]. \tag{A.9}$$

For $\dot{\boldsymbol{s}}_k = 0$ in the moving frame, the first equation is time independent if either (i) $\boldsymbol{n}_k = \langle \boldsymbol{n} \rangle$ for all particles or (ii) $\boldsymbol{\eta}_k = \mathsf{S}(-\phi)\boldsymbol{n}_k$ is time independent (all orientations rotate at the same angular velocity ω together with the whole configuration). In the first case, all the particles have the same orientation angle, that is $\theta_i = \theta_{\mathsf{c}}$ for $i = 1, 2, \ldots N$, while in the latter the time derivative of the particles orientations are the same, i.e., $\dot{\theta}_k = \dot{\theta}_l = \omega$ for any pair of particles in the system rotating as a rigid body with angular velocity ω. Hence, any of these conditions are sufficient to warrant a rigid body motion (with no deformations) of the system.

The two particular cases above result in Equation (A.9) to be rewritten as

- For $\boldsymbol{n}_k = \langle \boldsymbol{n} \rangle = \boldsymbol{n}_{\mathsf{c}}$ (which is equivalent to $\theta_i = \theta_{\mathsf{c}}$)

$$\left(\boldsymbol{n}_{\mathsf{c}} \times \dot{\boldsymbol{R}} \right) \cdot \hat{z} + \omega \boldsymbol{\eta}_{\mathsf{c}} \cdot \boldsymbol{s}_k = \beta^{-1} \dot{\theta}_{\mathsf{c}}; \tag{A.10}$$

- For $\dot{\theta}_k = \dot{\theta}_l = \omega$

$$\left(\boldsymbol{n}_k \times \dot{\boldsymbol{R}} \right) \cdot \hat{z} + \omega \left(\boldsymbol{\eta}_k \cdot \boldsymbol{s}_k - \beta^{-1} \right) = 0. \tag{A.11}$$

Therefore, for those conditions above if both the centroid motion and the rigid body rotation are present, they are intertwined in a way given by either Eq (A.10) or Equation (A.11).

In the following sections two particular cases of interest related to the above conditions associated with rigid body motion are explored.

A.1 POLARIZED PHASE

In the case where $\boldsymbol{n}_k = \langle \boldsymbol{n} \rangle = \boldsymbol{n}_{\mathsf{c}}$ for all particles (i.e., $\theta_k = \theta_{\mathsf{c}}$ for all k), the system is referred to as being in the polarized state. To explore this in more detail, consider the particular scenario where $\omega = 0$. In this situation, the cluster does not rotate around the centroid position, $\boldsymbol{R}$. As a result, the system behaves as a single particle and Equation(A.10) becomes

$$-\dot{R}\sin\chi_{\mathsf{c}} + R\dot{\varphi}_{\mathsf{c}}\cos\chi_{\mathsf{c}} = \beta^{-1}\dot{\theta}_{\mathsf{c}}, \tag{A.12}$$

where $\chi_{\mathsf{c}} = \theta_{\mathsf{c}} - \varphi_{\mathsf{c}}$ is the tilt angle and φ_{c} is the angle $\boldsymbol{R}$ makes with the horizontal axis. Meanwhile, Equation (A.7) projected along and orthogonal to $\boldsymbol{R}$ gives,

$$\dot{R} + R = \cos\chi_{\mathsf{c}}, \tag{A.13}$$

$$R\,\dot{\varphi}_{\mathsf{c}} = \sin\chi_{\mathsf{c}}. \tag{A.14}$$

Substituting these equations in Equation (A.12)

$$R^2\dot{\varphi}_{\mathsf{c}} = \beta^{-1}\dot{\theta}_{\mathsf{c}}. \tag{A.15}$$

This equation also shows that the areolar speed covered by the centroid is equal to the time derivative of the its orientation, θ_{c}, divided by β.

The above equations are the same as the ones for one active particle in a harmonic circular confinement, which have the solutions derived in Section 3.2. Therefore, for $\beta > 1$ a time independent periodic solution is given by $\dot{R} = 0$ and $\dot{\varphi}_{\mathsf{c}} = \dot{\theta}_{\mathsf{c}}$, that is the centroid performs a periodic circular motion with angular velocity, $\Omega = \frac{d\varphi_{\mathsf{c}}}{dt}$. Such a case gives

$$R = \beta^{-1/2}, \tag{A.16}$$

$$\Omega = \pm\sqrt{\beta - 1}, \tag{A.17}$$

$$\chi_{\mathsf{c}} = \theta_{\mathsf{c}} - \varphi_{\mathsf{c}} = \arccos\left(\beta^{-1/2}\right) \quad \Rightarrow \quad \theta_{\mathsf{c}} = \arccos\left(\beta^{-1/2}\right) \pm \sqrt{\beta - 1}t + \theta_{\mathsf{c}}(0). \tag{A.18}$$

A.2 VORTEX PHASE

Consider the case in which $\dot{\theta}_k = \omega$ for all k and assume that the particles rotate around the origin (that is $\boldsymbol{R} = 0$ and $\boldsymbol{r}_k = \boldsymbol{s}_k$). In this case, Equation (A.7) provides $\langle \boldsymbol{n} \rangle = 0$. The angular velocity for this situation of rigid body motion can be found by taking the vector product between $\boldsymbol{r}_k$ and Equation (A.1) and summing over the contributions of all particles, the internal torques cancel out and gives

$$\sum_k s_k^2\dot{\varphi}_k = \omega\sum_k s_k^2 = \sum_k s_k\sin\chi_k, \tag{A.19}$$

where $\chi_k = \theta_k - \varphi_k$. From Equation (A.11), $\boldsymbol{\eta}_k \cdot \boldsymbol{s}_k = s_k \cos\chi_k = 1/\beta$. Therefore,

$$\omega = \frac{\displaystyle\sum_k \sqrt{s_k^2 - \frac{1}{\beta^2}}}{\displaystyle\sum_k s_k^2}. \tag{A.20}$$

This result shows that a strict rigid body motion is possible in the vortex phase only for particles at $r > 1/\beta$.

To get around this, relax the condition $\dot{\theta}_k = \omega$, which means the system is not in strict rigid body motion, while still assuming that the particles rotate around the origin with approximate fixed radial positions (i.e., $\boldsymbol{r}_k = \boldsymbol{s}_k$ with $\dot{s}_k \approx 0$) and constant angular velocity $\dot{\varphi}_k \approx \omega$. Thus, Equation (A.9) becomes,

$$\dot{\chi}_k = (\beta s_k \cos\chi_k - 1)\,\omega, \tag{A.21}$$

whose solution is given by (ABRAMOWITZ; STEGUN, 1964, Eqs. 4.3.133 and 4.3.135),

$$-\omega\, t = \int_{\chi_k(0)}^{\chi_k(t)} \frac{d\chi}{1 - \beta s_k \cos\chi} = \frac{[G(t) - G(0)]}{\sqrt{|\beta^2 s_k^2 - 1|}} \tag{A.22}$$

where $\chi_k(0)$ is the value of χ_k at some initial time $t = 0$ and,

$$G(t) = \begin{cases} 2\arctan\left[\frac{(1+\beta s_k)\tan(\chi/2)}{\sqrt{|\beta^2 s_k^2 - 1|}}\right] & \text{for } \beta s_k < 1, \\ \ln\left[\frac{\sqrt{|\beta^2 s_k^2-1|} - (1+\beta s_k)\tan(\chi/2)}{\sqrt{|\beta^2 s_k^2-1|} + (1+\beta s_k)\tan(\chi/2)}\right] & \text{for } \beta s_k > 1. \end{cases} \tag{A.23}$$

The above solution gives rise to two distinct time dependencies of χ_k. For $s_k > 1/\beta$ there is a monotonic dependence of χ_k on time,

$$\chi_k = 2\arctan\left[\left(\frac{C_+ + C_- e^{-t/\tau_\omega}}{C_+ - C_- e^{-t/\tau_\omega}}\right)\sqrt{\frac{\beta s_k - 1}{\beta s_k + 1}}\right], \tag{A.24}$$

where $C_\pm = \tan\left(\chi_k(0)/2\right) \pm \sqrt{\left(\beta s_k - 1\right)/\left(\beta s_k + 1\right)}$ and $\tau_\omega = 1/\omega\sqrt{\beta^2 s_k^2 - 1}$. In this case, for $t \gg \tau_\omega$ there is an asymptotic value $\chi_k = 2\arctan\sqrt{\left(\beta s_k - 1\right)/\left(\beta s_k + 1\right)}$, which gives $\cos\chi_k = 1/\beta s_k$. This is exactly the result expected by assuming $\omega = \dot{\theta}_k$.

On the other hand, χ_k has oscillatory response for $r_k < 1/\beta$, given by

$$\chi_k = -2\arctan\left[\sqrt{\frac{1 - \beta s_k}{1 + \beta s_k}}\tan\left(\sqrt{1 - \beta^2 s_k^2}\frac{\omega t}{2} - C_0\right)\right], \tag{A.25}$$

where $C_0 = \arctan\left[\sqrt{\left(1 - \beta s_k\right)/\left(1 + \beta s_k\right)}\tan\left(\chi_k(0)/2\right)\right]$.

These above expressions for χ_k makes it possible to obtain the time averages of $\boldsymbol{n}_k \cdot \boldsymbol{r}_k = s_k \cos\chi$ and $(\boldsymbol{r}_k \times \boldsymbol{n}_k) \cdot \hat{z} = s_k \sin\chi$. For that it is necessary to compute the asymptotic limit of $\cos\chi_k$ and $\sin\chi_k$ for $r_k = s_k > 1/\beta$ and their time averages for $r_k = s_k < 1/\beta$. As previously mentioned, for $s_k > 1/\beta$ and $t \gg 1/\omega\sqrt{\beta^2 s_k^2 - 1}$, then $\cos\chi_k = 1/\beta s_k$, which gives

$$\boldsymbol{n}_k \cdot \boldsymbol{r}_k = s_k \cos\chi_k = \frac{1}{\beta} \qquad \text{and} \qquad (\boldsymbol{r}_k \times \boldsymbol{n}_k) \cdot \hat{z} = s_k \sin\chi_k = \sqrt{s_k^2 - \frac{1}{\beta^2}}. \tag{A.26}$$

For $s_k < 1/\beta$, after some straightforward calculations, Equation (A.25) gives

$$\sin\chi_k = -\frac{\sqrt{1-\beta^2 s_k^2}\,\sin\left(\sqrt{1-\beta^2 s_k^2}\,\omega t - 2C_0\right)}{1+\beta s_k \cos\left(\sqrt{1-\beta^2 s_k^2}\,\omega t - 2C_0\right)}, \tag{A.27}$$

$$\cos\chi_k = \frac{\beta s_k + \cos\left(\sqrt{1-\beta^2 s_k^2}\,\omega t - 2C_0\right)}{1+\beta s_k \cos\left(\sqrt{1-\beta^2 s_k^2}\,\omega t - 2C_0\right)}. \tag{A.28}$$

The time average of $\sin\chi_k$ over one period of time $T = 2\pi/\omega\sqrt{1-\beta^2 s_k^2}$ is zero since it is an odd function. On the other hand, the time average of $\cos\chi_k$ is nonzero and can be computed with a standard table of integrals (GRADSHTEYN; RYZHIK, 2014). Therefore,

$$\langle \sin\chi_k \rangle_T = 0 \qquad \text{and} \qquad \langle \cos\chi_k \rangle_T = \frac{1-\sqrt{1-\beta^2 s_k^2}}{\beta s_k}. \tag{A.29}$$

Consequently, for $s_k < 1/\beta$,

$$\langle \boldsymbol{n}_k \cdot \boldsymbol{r}_k \rangle_T = \frac{1-\sqrt{1-\beta^2 s_k^2}}{\beta} \qquad \text{and} \qquad \langle (\boldsymbol{r}_k \times \boldsymbol{n}_k) \cdot \hat{z} \rangle_T = 0. \tag{A.30}$$

Now, to calculate the average angular velocity with the above results in mind. Again, by taking the vector product between $\boldsymbol{r}_k$ and Equation (A.1), summing over the contributions of all the particles, and canceling out the internal torques

$$\sum_k s_k^2 \dot{\varphi}_k = \sum_k s_k \sin\chi_k. \tag{A.31}$$

By using $\dot{\varphi}_k \approx \omega$ and taking the time average of this equation, $\langle\omega\rangle$ can be obtained. Since $\langle (\boldsymbol{r}_k \times \boldsymbol{n}_k) \cdot \hat{z} \rangle_T = s_k \langle \sin\chi_k \rangle_T = 0$ for $r_k = s_k < 1/\beta$, Equation (A.31) results in

$$\langle \omega \rangle_T = \frac{\sum_k{}' \, s_k \langle \sin\chi_k \rangle_T}{\sum_k s_k^2} = \frac{\sum_k{}' \sqrt{s_k^2 - \frac{1}{\beta^2}}}{\sum_k s_k^2}, \tag{A.32}$$

where $\sum_k{}'$ means sum over only the particles outside of $r = 1/\beta$, while $\sum_k$ is the sum over all the particles. This expression is similar (but not equal) to Equation (A.20).

Finally, returning to Equation (A.21) and taking its time average will provide the time average of the particles orientation angle

$$\left\langle \dot{\theta}_k \right\rangle_T = \beta s_k \left\langle \cos\chi_k \right\rangle_T \left\langle \omega \right\rangle_T = \begin{cases} \left\langle \omega \right\rangle_T , & \text{for } s_k > \beta^{-1} \\ \left[1 - \sqrt{1 - \beta^2 s_k^2}\right] \left\langle \omega \right\rangle_T , & \text{for } s_k < \beta^{-1} \end{cases} \tag{A.33}$$

These obtained time dependencies of χ_k show that, although for $s_k > 1/\beta$ the conditions for a strict rigid body motion can be realized, that is not the case for particles inside $s < 1/\beta$. This conclusion can be seen by noticing that a time dependent χ_k implies in a time dependence of $\boldsymbol{n}_k$, which also implies that both $\dot{r}_k$ and $\dot{\varphi}_k$ in Equation (A.1) do depend on time. Therefore, the above results for the vortex phase are to be taken as an approximate model for the dynamics of particles moving together with the same angular velocities and with small variations of their radial distances to the origin.

APPENDIX B – CELL LINKED LISTS FOR MOLECULAR DYNAMICS

When dealing with simulations of large particle numbers, naively calculating the distance between every pair to find interparticle forces quickly becomes impractical since the number of pairs grows as $O(N^2)$. There are many ways to mitigate this, such as Verlet lists and cell linked lists, of which the latter will be described here. This describes a method that greatly speeds up simulations when dealing with short-range potentials, such as the WCA potential. While the method is described here for 2D system, it can easily be extended for 3D simulations as well.

B.1 SPACE PARTITIONING

The first step is to divide the simulation space into cells with size of at least the interaction cutoff radius r_c. This has to be done to guarantee that every particle inside the cutoff radius will be either in the same cell or in (first) neighboring cells. There are several ways to do this, with one of them being

```
// The floor function guarantees an integer number of cells
numcell_x = floor(boxlength_x / r_cutoff);
numcell_y = floor(boxlength_y / r_cutoff);
// The cell size is always equal or greater than r_cutoff
cellsize_x = boxlength_x / numcell_x, cellsize_y = boxlength_y / numcell_y;
```

this will partition the simulation box into an integer number with size of at least r_{cutoff}. Note that the amount of cells in each direction will differ if the simulation box isn't a square.

B.2 CREATING THE LINKED LIST

Now it is necessary to assign each particle to a cell in space. To do this, first create two lists

- head With size `numcell_x` × `numcell_y`;
- `linkedlist` With size N.

In this algorithm, head will store the highest particle index in each cell, while `linkedlist` will point the next highest index inside the cell. For example, if the cell number 3 has the particles `1, 5, 6` inside, then `head[3] = 6` and `linkedlist[6] = 5, linkedlist[5] = 1, linkedlist[1] = -1` (-1 will indicate there is no other particle in a cell). This means every particle in a cell can be quickly accessed, and assigning the particles to cells is a very fast procedure computationally. One of the ways to do is:

```
// Start by initializing the head array with -1 values
head[numcell_x * numcell_y] = {-1};
for(i = 0; i < N; i++){
    // Flatten the 2D array, each cell will now have an unique value assigned
         to it
    currentCell = numcell_x * floor(particle_y / cellsize_y) + floor(
        particle_x / cellsize_x);
    // Make linkedlist[i] point to the currently highest particle index in
        its cell
    linkedlist[i] = head[currentCell];
    // The i-th particle will now be the head of its cell, since it is the
        highest particle index inside it
    head[currentCell] = i;
}
```

B.3 INTERACTING WITH NEIGHBORING CELLS

With the cell list now constructed, the next step involves ensuring that each particle interacts with the particles located within its own cell as well as those in the eight surrounding neighboring cells. Special attention must be given to correctly handling interactions across periodic boundary conditions to maintain the physical consistency of the simulation.

```
// This is the outermost loop, going through all particles
for(i = 0; i < N; i++){
    //Get the indices for the i-th particle's cell
    partcell_x = floor(particle_x/cellsize_x), partcell_y = floor(particle_y/
        cellsize_y);
    //Now to look at all 9 cells around the i-th particle
    for(neighcell_x = partcell_x - 1; neighcell_x <= partcell_x + 1;
        neighcell_x++){
        for(neighcell_y = partcell_y - 1; neighcell_y <= partcell_y + 1;
            neighcell_y++){
            //Note that some languages define the modulo operator differently
                 for negative numbers.
            //This assumes that -1 % k = k-1 for k > 1, instead of -1
            neighcell_scalar = numcell_x * (neighcell_y % numcell_y) + (
                neighcell_x % numcell_x);
        }
    }
```

```
}
```

With the cell index for all cells around a particle, the only thing left is to use the linked lists to find all particles inside them.

```
// Use the head of the neighboring cell to find the highest particle index
    inside it
j = head[neighcell_scalar];
// If j is -1 that means a cell is empty
while(j != -1){
    // Due to Newton's third law, only cases for i < j need to be considered,
         since the force of i on j is the opposite of the force of j on i
    if(i < j){
        //Caution must be taken for the distance to be measured correctly
            along the edges of the system with periodic boundaries
        distance(i, j);
        if(distance < r_cutoff){
            /* The forces of i to j and j to i go in here */
        }
    }
    // Moves to the next element in the linked list, this happens until j is
        -1, which indicates the final element and ends the while loop
    j = linkedList[j];
}
```

note that the square root of the distance for the final step only needs to be taken if $r_{ij}^2 < r_{\text{cutoff}}^2$, which can increase efficiency as the square root is a computationally slow operation.

Another effective optimization involves the use of a lookup table (LUT) to store precomputed force values. This method discretizes the interval $[0, r_{\text{cutoff}}]$ into segments of length ι, computes the force at each discretized point, and stores the resulting values in an array. During the simulation, the force between a pair of particles separated by a distance r_{ij} can then be efficiently retrieved by accessing the LUT at the index $\lfloor r_{ij}/\iota \rfloor$. This significantly reduces computational overhead, especially when evaluating a complex interparticle potential, such as ones involving transcendental functions (ABELSON; SUSSMAN, 1996; GOULD; TOBOCHNIK; CHRISTIAN, 2007; PRESS et al., 2007).